NASA
Technical
Paper
2988

1990

Aerodynamic Pressure and Heating-Rate Distributions in Tile Gaps Around Chine Regions With Pressure Gradients at a Mach Number of 6.6

L. Roane Hunt
Langley Research Center
Hampton, Virginia

Kristopher K. Notestine
PRC Kentron, Inc.
Aerospace Technologies Division
Hampton, Virginia

National Aeronautics and
Space Administration
Office of Management
Scientific and Technical
Information Division

Summary

Surface and gap pressures and heating-rate distributions were obtained for simulated thermal protection system (TPS) tile arrays on the curved-surface test apparatus of the Langley 8-Foot High-Temperature Tunnel. Tile configurations representing two different chine radii were tested at nominal angles of attack of 7°, 10°, and 13° and unit Reynolds numbers from 0.371×10^6 to 1.400×10^6 per foot. The tests were made at a nominal Mach number of 6.6 and a nominal total temperature of 3400°R. Aerodynamic heating rates were determined from thin-wall metallic tiles located in the chine region to assess the effects of gap heating with and without filler material, and the pressures were obtained from orifices in the surrounding solid tiles of the array.

The results indicated that the chine gap pressures varied inversely with gap width because larger gap widths allowed greater venting from the gap to the lower model side pressures. Lower gap pressures cause greater flow ingress from the surface and increased gap heating. Generally, gap heating was greater in the longitudinal gaps than in the circumferential gaps. Circumferential gap heating at the mid-depth was generally less than about 10 percent of the external surface value. Gap heating was most severe at local T-gap junctions and tile-to-tile forward-facing steps that caused the greatest heating from flow impingement. The use of flow stoppers at discrete locations reduced heating in most gaps but increased heating in others. A limited use of "flow stoppers" or gap filler in longitudinal gaps could reduce gap heating in open circumferential gaps in regions of high surface pressure gradients.

Introduction

The thermal protection system (TPS) on the Space Shuttle orbiter consists of many ceramic tiles as described in references 1 and 2. The tiles are arranged with small gaps between the tiles to accommodate thermal expansion and deflection of the primary structure. Tile arrays are oriented to minimize the ingress of hot boundary-layer gases into the tile gaps. Early investigators (refs. 3–12) recognized the potential of gap heating problems and performed numerous wind-tunnel tests to obtain various gap heating correlations.

A series of gap heating studies (refs. 5–7) on flat simulated tile arrays with zero pressure gradients were performed in the Langley 8-Foot High-Temperature Tunnel (8′ HTT) for various gap widths, gap lengths, and flow angles with respect to the gaps. These data, along with other available data, were analyzed and correlated in efforts typical of those used in reference 8. Later efforts were made in references 13 and 14 to interpret and analyze tile damage resulting from the first Shuttle flights. Overall, the TPS tile temperatures during flight were lower than expected, but local hot spots from surface steps produced by uneven tile heights and large gap widths caused significant damage to the tile system. Therefore, additional gap filler was used in later flights at locations where tile-gap fabrication tolerances could not be maintained.

Gap heating has also been studied in regions of high pressure gradients, such as Shuttle chine regions where the surface transitions from the relatively flat windward surface to the side and leeward surfaces of the vehicle. In reference 15 the gap heating was assumed to be proportional to the local pressure gradient, and specifications were established to determine the pressure gradient threshold for which gap fillers would be required. Earlier efforts (refs. 10–12) to study gap heating with surface pressure gradients were hampered because of the difficulty of producing realistic aerodynamic pressure gradients on full-scale tile systems. Although no Shuttle missions have been jeopardized by TPS failures, the ceramic tile system continues to be a major concern, and extensive tile repairs are performed between flights. The requirement for gap fillers costs the Shuttle both in vehicle weight and in refurbishment labor between flights. To be conservative, much gap filler is used since little is known about the flow in open tile gaps in the chine regions.

The purpose of the present study was to define the pressure and heating-rate distributions in open tile gaps in typical chine regions for a range of surface pressure gradients and to determine the effects of discrete gap fillers designed to reduce the overall gap heat loads. Realistic aerodynamic pressure gradients were obtained using the curved-surface test apparatus (CSTA) in the Langley 8′ HTT. The flow field and the surface pressure and heating-rate distributions for the CSTA are presented in reference 16. A simulated tile array was designed for the rear section of the CSTA that allowed two tile configurations of different chine radii to be studied. Special metallic thin-wall tiles instrumented with thermocouples were installed in the chine regions to determine gap heating-rate distributions. This study was made at a nominal Mach number of 6.6, a unit Reynolds number range from 0.371×10^6 to 1.400×10^6 per foot, and a nominal total temperature of about 3400°R. The model was tested at nominal angles of attack of 7°, 10°, and 13°. Also, gap filler was installed as "flow stoppers" at discrete locations to determine if such a method might reduce chine gap heating and result in less use of the current Shuttle continuous filler material.

Symbols

c_p	specific heat at constant pressure, Btu/lbm°R
D	total tile-gap depth, in.
F_1, F_2, F_3	width of model flats (fig. 4), in.
h	tile-to-tile step height, in.
L	total tile-gap length, in.
ℓ	distance along tile gap, in.
M	Mach number
N_{Re}	unit Reynolds number, per foot
N_{St}	Stanton number
p	pressure, psia
q	dynamic pressure, psi
$\dot{q}$	heat-transfer rate, Btu/ft^2-sec
R	chine radius (fig. 4), in.
R_n	model nose radius, in.
S_R	total chine arc length (fig. 4), in.
s	circumferential distance around chine (fig. 4), in.
T	temperature, °R
t	time, sec
V	velocity, ft/sec
w	tile-gap width, in.
x	axial distance from nose (fig. 4), in.
y	vertical distance from tunnel centerline (fig. 20), in.
z	tile-gap depth from outer surface, in.
α	model angle of attack (fig. 4), deg
Δ	incremental change
ρ	density, lbm/ft^3
τ	wall thickness, in.

Subscripts:

c	combustor
ref	reference
t	total
w	wall
2	behind normal shock wave
∞	test chamber free stream

Abbreviations:

P	pressure on smooth side of model
PG	tile-gap pressure
PS	surface pressure on tile side of model
Q	Gardon heat gauge on smooth side of model
QG	tile-gap heating rate
QS	surface heating rate on tile side of model
QW	thick-wall thermocouple on smooth side of model
QX	coaxial thermocouple on smooth side of model
TG	tile-gap temperature
TS	tile surface temperature

Apparatus and Test

Model

The model consisted of an array of simulated surface insulation tiles attached to one-half the aft portion of the curved-surface test apparatus (CSTA). The model is shown in figure 1 installed in the Langley 8-Foot High-Temperature Tunnel (8′ HTT). The other half of the CSTA had a smooth surface and was fabricated from 0.38-in-thick nickel plate. The CSTA is 107.63 in. long and is 36.28 in. by 24.20 in. at the base as shown in figure 2. The top and bottom surfaces are inclined 5.0°, and the sides are inclined 8.2° with the model axis. The basic model cross section consists of four circular arcs separated by four straight-line segments. The CSTA has a 3-in. spherical nose radius and boundary-layer flow trips at $x = 3.00$ in. as illustrated in figure 3.

The model was tested in the two configurations that are illustrated in figure 4. Configuration 2 is obtained from configuration 1 by rotating the model 180° about the model axis. For configuration 1 the small chine radius is on top, and for configuration 2 the large chine radius is on top. The model nose is pitched down for positive angles of attack. The arc radii (R), arc lengths, (S_R), and straight-line segment lengths (F_1, F_2, and F_3) are linear functions of model axial length x. The equations for these terms are given for each configuration in figure 4.

Photographs of test configurations 1 and 2 are presented in figures 5(a) and 5(b), respectively. The tile array was fabricated from large aluminum sections that were bolted to the strongback prior to machining the outer mold-line surface. Then, each large section was removed and cut into individual tiles. The tiles were then bolted to the strongback with 0.060-in. gaps between tiles. This method of fabrication ensured a precise outer mold-line surface and a precise tile-gap alignment. In configuration 1, a single row of tiles is oriented along the small-radius chine to cover the entire arc length between the continuous gap along the windward tangent line ($s = 0$ in fig. 4) and the gap along the side tangent line ($s = S_R$ in fig. 4). This is representative of the Shuttle tile orientation on the wing strake. (See ref. 15.) In configuration 2, the circumferential gaps between tiles are continuous and the longitudinal gaps are staggered. This arrangement is characteristic of the chine at the forward section of the Shuttle fuselage. (See ref. 17.) Both configurations are located in the sketch in figure 5.

For each configuration, specific solid chine tiles at about $x/R_n = 25$ were replaced with instrumented thin-wall tiles as indicated in figure 5. The walls of these tiles were fabricated from 0.030-in-thick AISI type 316 stainless steel welded in the corners and were instrumented with about 40 chromel-alumel thermocouples spotwelded to the inside of the top and side surfaces. The instrumented tile for the small-radius chine of configuration 1 is shown in figure 6, and the tile array with the tile both removed and installed is shown in figure 7. Because of the inexact nature of the fabrication process, the thin-wall tile was smaller than the solid aluminum tile that it replaced. Therefore, the tile was installed with an upstream circumferential gap of about 0.075 in. in width and a corresponding downstream gap of about 0.103 in. in width. The tile was shimmed from the subsurface to match the four outer corners of the tile with the height of the adjacent tiles. The general curvature of the instrumented tile matched the tile array, but no attempt was made to measure the precision of the instrumented tile curvature.

Similarly, the two thin-wall instrumented tiles shown in figure 8 were designed to replace adjacent tiles on the large-radius chine of configuration 2. In this case, the thin-wall tiles matched the size of the original solid tiles of the array. In figure 9, the tile array is shown with the tiles removed and with the instrumented tiles installed. Again, the thin-wall tile corners were shimmed to match the surrounding tiles, and the thin-wall tiles were adjusted in the array to obtain uniform gap widths that vary from 0.058 to 0.068 in.

Instrumentation

Although the primary instrumentation of the model was in the tile array, the smooth side of the model was also instrumented for pressure and heating-rate measurements to establish the undisturbed surface flow conditions. A full parametric study of the surface pressure and heating-rate distributions of the CSTA is presented in reference 16. Some of the instrumentation used in reference 16 was reinstalled on the smooth side to provide a direct comparison of the smooth-surface values with those of the tile-array side of the model. The longitudinal line of instrumentation on the windward pitch plane and the circumferential line of instrumentation opposite the instrumented tiles shown in figure 10(a) were used for each configuration. Each instrument number is representative of both a pressure orifice and an adjacent Gardon heat-flux gauge. Additional instrumentation on the smooth side, illustrated in figure 10(b), consisted of chromel-alumel thermocouples spotwelded to the backside of the 0.38-in-thick nickel skin and chromel-constantan coaxial thermocouples installed in small stainless steel plugs to measure outer-surface temperatures in a circumferential line near the rear of the model.

Details of the pressure orifice and Gardon heat-flux gauge installation are shown in figure 11 with the pressure orifice located 1.0 in. upstream of each heat-flux gauge. The surface pressure orifices were installed using stainless steel tubes mounted through the model wall and flush with the outer surface. The tubes, which were 2 to 4 ft long with a 0.060-in. inside diameter, were attached to individual electromechanical pressure transducers located inside the model. The Gardon heat-flux gauges were the heat-sink type with a 0.005-in-thick chromel disk mounted flush with the model surface and bonded to a nickel body. The gauge body was threaded and installed in the model walls as shown in figure 11. The gaps around the disk were filled with a ceramic compound to provide a flush surface installation.

The chromel-constantan coaxial thermocouple shown in figure 12 consisted of a thermocouple probe extending through the threaded stainless steel plug to the outer surface of the model. The thermal transport properties of the thermocouple and plug were matched to ensure one-dimensional conduction into the plug. Therefore, transient heat flux was obtained from the surface temperature history. Gaps around these plugs were also filled with the ceramic compound.

The location of thermocouples and pressure orifices for the instrumented tiles for configurations 1 and 2 are illustrated in figures 13 and 14 and in figures 15 and 16, respectively. The 41 thermocouples attached to the inner surface of the small-radius-chine tile of configuration 1 are shown in an unfolded graphic representation in figure 13. The corresponding pressure instrumentation in the surrounding solid tiles is illustrated in figure 14 by the graphic perspective representation of the tile array with the thin-wall tile removed. Special Gardon heat-flux gauges QG1 and QG2 are shown in figure 14 in the gaps for direct comparison with heating data obtained from thin-wall tile temperatures. Similar illustrations are presented for the thermocouple locations on the two adjacent thin-wall tiles of the large-radius chine of configuration 2 in figure 15 and for the pressure orifices and heat-flux gauges surrounding the tiles in figure 16. Generally, instrumentation was sparsely distributed on all exposed tile surfaces. Gap (or tile sidewall) instrumentation was primarily located at the mid-depth of the gaps to trace gap-flow paths, but some instruments were located along a line normal to the tile outer edge to define indepth pressure and heating variations.

All model instrument locations are defined in figures 10–16 and tables I and II. Instruments are located by coordinates of longitudinal distance (x) and circumferential distance from windward tangent line (s) defined in figure 4. Tile instrument locations are also described by length in longitudinal gaps (ℓ) and gap depth (z).

Facility

The Langley 8-Foot High-Temperature Tunnel (8′ HTT), shown schematically in figure 17, is a large blowdown tunnel that simulates aerodynamic heating and pressure loading for a nominal Mach number of 7 at altitudes between 80 000 and 120 000 ft. The high energy needed for temperature simulation is obtained by burning a mixture of methane and air under pressure in the combustor and expanding the products of combustion through a conical-contoured nozzle into the open-jet test chamber. The flow enters a supersonic diffuser where it is pumped by an air ejector through a mixing tube and exhausted to the atmosphere through a subsonic diffuser. The tunnel operates at total temperatures from 2400°R to 3600°R, free-stream dynamic pressures from 250 to 1800 psf, and free-stream unit Reynolds numbers from 0.3×10^6 to 2.2×10^6 per foot, and it has a maximum run time of 120 sec.

The model is stored in the pod below the test stream to protect it from adverse tunnel start-up loads. Once the desired flow conditions are established, the model is pitched to the desired angle of attack and inserted into the test stream on a hydraulically actuated elevator. Insertion time is typically 1.5 sec. More detailed information about the tunnel can be found in reference 18.

Test Conditions and Procedure

A schematic of the test section of the 8′ HTT with the CSTA model installed is shown in figure 18. The model was sting mounted to the curved strut used to pitch the model assembly. The 107.63-in-long CSTA model extended to within 0.5 ft of the tunnel nozzle exit. Calibration tests (ref. 16) indicated that pitch angles of 15° can cause the model nose to extend beyond the test core into lower-temperature stream flow and can produce tunnel flow blockage that causes abnormally high pressure in the model base region. Therefore, the angle of attack for the present test was limited to less than 15°. The model was tested at angles of attack of 7°, 10°, and 13° to establish a reasonable range of pressure difference between the windward and leeward surfaces of the model. An additional variation of pressure differential was obtained by varying the tunnel combustor pressure.

The test summary of both model configurations is presented in table III. For configuration 1, the CSTA was oriented with the small-radius chine up, and the model angle of attack was varied (pitched down) in tests 1, 2, and 3 for combustor pressures of about 1500 psia. In tests 4, 5, and 6, α was constant at 10° and the combustor pressure was 703, 1000, and 2480 psia, respectively. Configuration 1 was then tested with various gap-filler arrangements. Similar tests were made on configuration 2 with the large-radius chine up, and the model pitched down for tests 10, 11, and 12. The combustor pressure was not varied above 1500 psia because of tunnel operation problems that occurred during these tests. Therefore, only two tests were made at different pressures (tests 13 and 14). Tests 15 and 16 were made with some tile-to-tile forward-facing steps, and the last test was made with a gap filler at discrete locations in the longitudinal gaps. The forward-facing steps and the gap-filler arrangements are described later.

The flow parameters for each test are presented in table III. The total temperature and combustor pressure are listed along with selected free-stream flow properties calculated from tunnel surveys and gas properties that are presented in reference 19. The tunnel surveys were obtained using the flow survey apparatus (FSA) after the model was retracted, as shown in figure 19. This figure shows the model, in a triple photographic exposure, leaving the test position and the FSA in its stowed position ready to be driven across the test stream in pendulum fashion. The FSA was instrumented with a total of 37 probes, including pitot and static pressure probes and total temperature probes. The model was tested primarily at a nominal free-stream total temperature and combustor pressure of 3400°R and 1500 psia, respectively, to produce a free-stream Mach number of 6.6 and a unit Reynolds number of 0.86×10^6 per foot. The off-nominal test conditions provided a maximum Reynolds number of 1.400×10^6 per foot in test 6 and a minimum of 0.371×10^6 per foot in test 13. Since the model was maintained at the ambient temperature condition prior to model insertion into the test stream, the ratio of wall temperature to total temperature was about 0.16 for this study.

Data Reduction and Analysis

Model pressures, heating rates, and tunnel data were recorded on magnetic tape at a rate of 20 samples per second using the on-site 8′ HTT computer. The magnetic tapes were then sent to the Langley Central Digital Data Recording Subsystem for processing of the information to engineering units. Model pressure values were selected from the pressure histories when the model reached the tunnel horizontal centerline after steady pressures were established on the surface and in the orifice tubes connecting the transducers. From pretest checks at known pressure levels, the data error of the pressure gauges and the data recording system was less than 0.25 percent of the full-scale range. However, the actual percentage error when the gauge is operating at the bottom of its scale can be intolerable unless the output data are adjusted for the lower range pressures. This adjustment was conveniently accomplished in the present test by adjusting all pressure data to match the data from a reference precision gauge. As a result, the error is limited to the effects of small-gauge nonlinearity between the low reference pressure and full-scale gauge pressures, and therefore the maximum error is assumed to be less than about 0.5 percent.

The surface heating rates on the tiles were calculated from the measured thin-wall temperature-time histories by using the one-dimensional, transient heat balance equation

$$\dot{q} = \rho c_p \tau (\Delta T / \Delta t) \qquad (1)$$

A continuous heating-rate history during the entire model exposure was obtained using the central difference method to obtain the slope of the temperature-time data. Heating-rate values were selected from the heating-rate histories when the model reached the tunnel horizontal centerline. The uncertainty in the wall thickness was about ±2 percent. For the present test, the measured thin-wall temperature rise was less than 200°R when the data value was selected; therefore, radiation losses were negligible. The heating rates were calculated using values of c_p as a function of wall temperature, and the heating rates were adjusted to the equivalent cold-wall heating rate for a wall temperature of 540°R. The thermocouple instrumentation was located at least 0.5 in. from the tile edges to minimize lateral heat-conduction effects at the tile corners. Overall, the errors in the tile heating rates were estimated to be less than about ±5 percent.

The heating rates on the smooth side of the CSTA were measured using Gardon heat-flux gauges, coaxial thermocouples, and thermocouples on the backside of the nickel thick wall. The heat-sink Gardon gauge has proven to be durable and consistent in its output repeatability for the severe aerothermal environment of the 8′ HTT. As shown in figure 11, the gauge body was threaded so that it could be adjusted flush with the outer surface of the model. Since the surface temperature was less than 590°R, the heating rates were not adjusted for surface temperature rise. The primary source of Gardon gauge error is the inherent error associated with the use of a radiant heat source during calibration. Multiple calibrations of individual gauges have been analyzed, and the total error band based on the calibration repeatability was ±7 percent.

The heating rates measured using the coaxial thermocouples were obtained from the temperature history of the thermocouple at the surface of the stainless steel plug shown in figure 12. Using the thermal properties of the stainless steel substrate, the surface heating rate was calculated assuming one-dimensional transient heat conduction of a classic semi-infinite slab with ambient temperature at the inner surface. An integral solution of the temperature history provided a heating-rate history.

The heating rates measured using the thermocouples attached to the backside of the 0.38-in-thick nickel wall were obtained from an inverse solution of a one-dimensional, transient lumped-capacitance analysis. The wall was divided into 10 lumps through its thickness, and the heat balance for each lump was determined including heat convection, conduction, and storage. Assuming the backside thermocouple temperature history for the tenth lump, the temperature histories of the other lumps and the convective heating rate to the outer surface were obtained from the inverse solution.

The experimental heating-rate data of this study were converted to Stanton number based on the free-stream flow conditions given in table III. Stanton number is defined by the expression

$$N_{\mathrm{St},\infty} = \frac{\dot{q}}{(T_{t,c} - T_w)(\rho V c_p)_\infty} \qquad (2)$$

where values of $T_{t,c}$ and $(\rho V c_p)_\infty$ are given in table III.

Results and Discussion

The primary focus of the present study is to define the pressure and heating-rate distributions in tile gaps in typical chine areas for a range of surface pressure gradients and to determine the effects of discrete gap fillers designed to reduce the overall gap heat loads. To properly understand the tile-gap flow, the external pressure and heating-rate distributions are compared with predicted results to verify the general characteristics of the flow environment. Then, the gap pressure and heating-rate distributions for the circumferential and longitudinal gaps in the chine regions of configurations 1 and 2 are presented for a range of surface pressure gradients produced by varying model angle of attack and free-stream Reynolds numbers. Finally, the circumferential gap pressures and heating rates with and without discrete gap fillers are presented to indicate the effects of a limited use of gap filler. Model pressures, listed in tables IV and V, are normalized by the free-stream static pressures given in table III. The heating-rate data are presented in tables VI and VII as Stanton numbers based on free-stream total temperature and on $(\rho V c_p)_\infty$ values which are also given in table III.

Local Flow Field

Free-stream surveys. Following the model tests, a limited number of flow surveys were made using the FSA to define the general flow patterns at two tunnel stations: the nozzle exit and the test-chamber centerline. The FSA was slowly swept transversely across the test flow to measure pitot and static pressures that were used to compute pressure and Mach number contour plots of the complete free stream; and the FSA was stopped at the vertical centerline to obtain near-steady-state total temperature profiles across the free stream. Generally, the pressure and Mach number distributions were axisymmetric about the tunnel horizontal centerline; however, some asymmetry occurred as a result of repair or replacement of combustor hardware during these tests, such as the fuel-injection system and the nozzle-throat film-cooling slot. The overall trend of the surveys indicated that the flow continued to expand to a higher Mach number downstream from the nozzle exit and was a maximum near the center of the test section. The overexpanded flow was then compressed as it approached the downstream diffuser.

Typical free-stream flow for the present tests is illustrated in figure 20 for the two tunnel stations. The pitot pressure and the total temperature normalized by the combustor total condition are plotted against the vertical distance y above the horizontal centerline. The changes in the pitot pressure profile from near the nozzle exit to the vertical centerline are illustrated in the figure and are similar to the survey data obtained about 20 years earlier with a smaller survey rake. (See ref. 18.) In figure 20, the change in pitot pressure profile is primarily a decrease in the pressure ratio from 0.0075 to 0.0065 along the horizontal centerline as the flow expands to a higher Mach number. The variation of the pressure profiles is probably produced by weak shock wave patterns that are not canceled by the nozzle contour.

The temperature profiles in figure 20 indicate a general recovery of centerline free-stream temperature of about 95 percent of the combustor value. The decrease in measured temperature with distance from horizontal centerline is caused by a combination of factors including the flow mixing of the hot gases near the center with the cooling air in the nozzle boundary layer. Also, the measured temperature farther from the horizontal centerline required greater time to reach the same degree of steady state because of lower heat-transfer coefficients on the thermocouples resulting from lower stream pressures. Therefore, the measured temperatures are not steady-state values, and the FSA temperature probes are being redesigned to provide more time-responsive measurements.

The purpose of figure 20 is to show how the windward surface of the CSTA model, shown in the sketch at the top of the figure, cuts across the wavy pressure profiles for the various test angles of attack. A basic difficulty in using the CSTA, as discussed in reference 16, is that the model nose is translated into flow of much-reduced pressure and temperature at moderate angles of attack. In figure 20 for each tunnel station, the intersection of the model surface with the flow survey line is indicated by the symbols that correspond to each angle. The instrumented portion of the chine tile array is located near the pitch center and is instrumented sufficiently to define local flow conditions independent of the uneven nature of the overall flow field. Therefore, the external surface pressure and heating-rate distributions presented in the next sections are used to define the baseline, localized chine flow conditions for the present study.

Surface pressure distributions. Longitudinal pressure distributions of the windward surface for both the small- and large-radius-chine configurations are presented in figure 21 for all three test angles of attack. The measured surface pressure normalized by the free-stream pressure is compared with the predictions of tangent-cone theory (ref. 20). The general magnitude of pressure agrees with theory, but the data have a wavy profile that increases in amplitude with angle of attack. The wavy pressure distribution was caused by weak shock waves in the free stream, and the waviness increased when the model angle of attack increased because the model cuts across more of the test stream as illustrated in figure 20.

The circumferential pressure distribution is presented in figure 22 for both test configurations. The normalized pressure is plotted against the circumferential distance s, normalized by the chine arc length S_R, for pressures measured on both the smooth and tile sides of the model. The pressure distributions on the smooth side of the model at $x/R_n = 25.55$ are compared with the surface pressures on the tile side at about the same model longitudinal location. The curves represent the tangent-cone values calculated from estimated angles between the local surface and the free-stream flow. The circumferential pressure distribution is a similar function of s/S_R for both configurations and is in good agreement with the tangent-cone theory. This agreement indicates that the flow is Newtonian, which is the basic assumption for the tangent-cone theory. The agreement between the open and closed symbols indicates that the surface pressure is not affected by the gaps in the tile array.

As discussed earlier, the two configurations have different chine radii and different tile orientations on the chine regions. The two chine radii produce very different circumferential pressure gradients. For high-pressure gradient regions of the Shuttle, open tile-gap heating was expected to be a function of the local pressure gradient. In reference 15, the pressure gradient required to produce severe gap heating was defined by the following relationship:

$$\frac{\Delta p}{\Delta s}\sqrt{p} > 0.00061 \text{ (psi)}^{3/2}\text{/in.} \qquad (3)$$

where $\Delta p/\Delta s$ is the surface spatial pressure gradient and p is the local surface pressure. The value given above reflects the low atmospheric pressure for the high altitude where the Shuttle experiences its greatest aerodynamic heating.

The present study simulated a lower altitude with greater surface pressures than those assumed in equation (3). The resulting values of the pressure gradient parameter, computed from measured smooth-side pressures, were orders of magnitude higher as indicated in figure 23. The maximum value for the pressure gradient parameter occurred at about $s/S_R = 0.6$ and increased with model angle of attack. In configuration 1, a single tile spanned the entire chine arc length, and the maximum value of pressure gradient parameter was 0.25. This large value was caused by the decrease in pressure occurring over the short-chine arc length covered by the one tile. The maximum pressure gradient parameter for configuration 2 was much smaller because the same pressure decrease occurred over a longer chine arc length. Since the two instrumented tiles covered only two-thirds the distance around the chine, the second instrumented tile reached only to the point of maximum pressure gradient. Therefore, the two configurations represent contrasting conditions in terms of the spatial pressure gradients, although the actual pressure distributions correlate with chine angular position as shown in figure 22.

Surface heating distributions. Longitudinal heating distributions for the windward surface, corresponding to the pressure distributions of figure 21, are presented as a function of x/R_n in figure 24 for both test configurations and all angles of attack. The measured heating-rate data from the Gardon gauges on the smooth side of the model for each configuration are in agreement within the scatter of the data. The solid symbols for $\alpha = 10^\circ$ represent data obtained from the thermocouples attached on the backside of the 0.38-in. nickel smooth surface. The thermocouple and Gardon gauge results agree and indicate an increase in surface heating with increasing longitudinal distance along the model. Predictions of the longitudinal heating are also presented for each angle of attack using the same approach as that described for CSTA calibration studies in reference 16 for both sharp and blunt cones. These predictions are for a turbulent boundary layer using the computed tangent-cone pressures of figure 21, the local flow conditions for sharp and blunt cones, and the Eckert's reference temperature (ref. 21) for evaluation of gas thermal properties. The reduced heating for the blunt prediction was caused by the increased entropy associated with the normal shock wave that stands off from the model nose. For blunt bodies, the entropy-layer thickness decreases along the model length. Therefore, the measured heating rates tend to agree with the blunt-cone predictions near the nose but agree with the sharp-cone predictions farther along the model length.

The circumferential heating-rate distributions around the small and large chines for configurations 1 and 2 are presented in figures 25 and 26, respectively. The heat-transfer coefficient is plotted as a function of s/S_R to cover the model windward surface from the centerline to the side flat. The heating rates measured from the Gardon gauges on the smooth side of the model at $x/R_n = 25.88$ (circular symbols) are shown for comparison with the heating rates computed from the thermocouples attached to the thin-wall tiles at about $x/R_n = 25$ (square symbols). The heating rates measured on the smooth model and on the tiles are generally in good agreement for both configurations. However, for configuration 1 (fig. 25) near the chine tangent line ($s/S_R = 0$), heating rates are much lower on the tile than on the smooth surface. There are two factors that may have contributed to the reduced heating rates measured on the tile surface. First, the higher heating rates on the tile heating could have caused lateral conduction errors that would affect the indicated heating rates. Second, the curvature of the sheet-metal tile may have been less than that of the smooth reference side because of the difficulty in fabrication. The tile outer edges matched the machined model curvature, but there was no method to ensure the midspan curvature of the unsupported tile outer surface.

A comparison of the circumferential heating distributions on the two chine radii (figs. 25 and 26) shows that there is considerable difference. Therefore, the same data for both configurations at $\alpha = 10^\circ$ are presented in figure 27 along with additional data for $x/R_n = 34.88$ from the smooth side of the model. The heating-rate distributions from the second location include results obtained from coaxial gauges as well as from the Gardon gauges and the thermocouples. The solid curves in figure 27 are hand faired through the data from the smooth side of the model and illustrate the higher heating at the windward tangent line ($s/S_R = 0$) on the smooth side compared with that on the tile side. In figure 27(a), the heating on the smooth side is about 50 percent higher at $s/S_R = 0$ than the average heating on the flat surface near the windward centerline. The heating distribution on the large chine shown in figure 27(b) indicated a much flatter profile near $s/S_R = 0$, but the tile heating (open squares) was still less than the heating on the smooth side. The greater heating at the windward tangent line of the small-radius chine of configuration 1 resulted from a thinning of the boundary layer caused by the sharper turning angles of the flow (greater localized crossflow) with the small chine. These differences were also noted in the calibration results of the CSTA in reference 16.

One of the reasons for defining the circumferential heating distribution was to determine a normalizing value for presenting the gap heating in the following sections of this paper. Because of the general rise in heating at $s/S_R = 0$, the reference location at the model windward centerline was selected. Both the model reference pressure p_{ref} and heating rate $\dot{q}_{\text{ref}}$ at this location were obtained from the measured data, and the values are given in table VIII. All gap pressure and heating data are normalized by these reference values in the remainder of the paper.

Gap Flow for Configuration 1

Effects of angle of attack. The purpose of testing at the various angles of attack was to determine the effect on tile-gap heating for various pressure gradient conditions over the tile array. As indicated in figure 23(a), the local spatial pressure gradient was significantly different for tests at $\alpha = 7^\circ$, 10°, and 13°, and the overall pressure differential around the chine increased with angle of attack as indicated in figure 22.

The gap pressure and heating-rate distributions in the circumferential gaps of configuration 1 are presented as a function of s/S_R in figure 28. The results obtained at the mid-depth position are presented for gaps A and B located upstream and downstream of the instrumented tile, respectively. The data obtained on the tile outer surface are also presented for comparison and are represented by the closed symbols. The surface pressure distribution was obtained at $x/R_n = 24$, which was upstream of gap A. The circumferential gap pressure distributions with s/S_R did not have the same trend as the circumferential surface pressure distributions. For both gap A and gap B, the gap pressure distributions had a flatter profile and the pressure level was a function of gap width. The pressure in the smaller gap A ($w = 0.075$ in.) was greater than that in the larger gap B ($w = 0.103$ in.). The pressure in the circumferential gaps varied inversely with gap width, and the pressure in the larger gap B approached the tile surface pressure at the side of the model. Therefore, in the chine region, more gap-flow venting to the low-pressure regions of the model occurred for the large gap than for the small gap.

The circumferential gap heating for gaps A and B is presented in the lower plots in figure 28 with the heating data plotted on a log scale. The surface heating, shown by the closed symbols, was obtained on the tile at $x/R_n = 25$. The gap heating was generally an order of magnitude less than the surface heating. In the smaller gap A, the heating did not vary substantially with α; but in the larger gap B, the gap heating increased with α. The increase in heating with α in gap B was probably due to the increase in gap-flow venting, noted previously to be indicated by the lower gap pressure.

The longitudinal gap pressure and heating distributions for gaps at $s/S_R = 0$ and 1 are presented as a function of ℓ/L in figure 29. Even though the pressure instrumentation is limited, the results indicated that the gap pressure at $s/S_R = 0$ was about constant at the surface (reference) pressure level. Although p/p_{ref} at $s/S_R = 1$ varied with angle of attack, the absolute gap pressure was constant and equal to the model side pressure. The corresponding gap heating is presented in the lower plots in figure 29. The heating in the longitudinal gap that was aligned with the windward flow at $s/S_R = 0$ ranged from 10 to 30 percent of the surface reference heating and was higher than the circumferential gap heating in figure 28. The closed-symbol results from Gardon heat gauges located in the gap on adjacent tiles (see fig. 14) agreed with the open-symbol results from the instrumented tile thermocouples located on the opposite gap walls. The gap heating increased with distance along the longitudinal gap length. As indicated in references 9 and 10, heating in gaps aligned to the local flow varies as a function of gap length. The gap heating in the longitudinal gap at $s/S_R = 1$ was much lower because the local surface flow was not aligned with this gap, and thus less flow ingress into the gap occurred.

A limited amount of data was obtained to indicate the gap pressure and heating-rate distributions through the depth of the tile gaps, and the results are presented in figures 30 and 31. In figure 30, the distributions are presented as a function of z/D for the circumferential gaps A and B at $s/S_R = 0.5$. The gap pressure did not vary much with gap depth at these locations. The gap heating in gap A decreased significantly with an increase in z, but the heating in gap B increased slightly. In gap B, the lower gap heating at $z/D = 0.2$ was probably due to flow separation on the downstream wall of the instrumented tile. The longitudinal gap heating at $\ell/L = 0.5$ for $s/S_R = 0$ and 1 is shown in figure 31. At both locations, the gap heating decreased consistently with increasing z/D. Overall, the gap heating for configuration 1 decreased with depth into the gaps.

Effects of Reynolds number. The variation of Reynolds number in the present study provided a variation of pressure differential around the chine for a fixed angle of attack of 10°. The effect of Reynolds number is illustrated in the circumferential pressure and heating-rate distributions presented in figure 32. The surface pressure distributions at $x/R_n = 24$ (closed symbols) did not vary significantly for the range of Reynolds numbers tested, but the overall pressure differential varied by a factor of 3.6 because of the change in p_{ref}.

The gap pressure distributions in figure 32 varied slightly with Reynolds number for both circumferential gaps A and B. The pressure in the smaller width gap, gap A, was greater than the pressure in gap B because of the greater pressure venting in the larger width gap, gap B, to the lower pressure region on the side of the model. In both gaps the pressure varied inversely with Reynolds number. Apparently, for a given gap width, the pressure venting was proportional to the overall pressure differential around the chine.

The surface heating distributions in figure 32 did not vary for the range of Reynolds number tested. The heating in both gaps increased with Reynolds number because of the corresponding increase in overall pressure differential that produced greater venting of gap flow. Overall, the gap heating was at least an order of magnitude lower than the surface heating q_{ref}.

Gap Flow for Configuration 2

Effects of angle of attack. The pressure gradients produced on configuration 2 were much less than those produced on configuration 1, as shown in figure 23(b), and the maximum gradient occurred at about $s/S_R = 0.6$ which coincides with the leeward edge of the second instrumented tile. However, the overall pressure differential for configuration 2 did increase with angle of attack. (See fig. 22.) As noted previously, the purpose of testing at the various angles of attack was to determine the effect on gap heating when the pressure gradient over the tile array on the chine was varied.

The gap pressure and heating-rate distributions in the circumferential gaps of configuration 2 are presented as a function of s/S_R in figure 33. The outer surface pressure distributions for $x/R_n = 25.2$ are also presented for comparison and are represented by the closed symbols. The pressure in gap A was less than the surface pressure, but the circumferential trend was the same as the surface pressure. The pressure distributions in gap B are not presented in figure 33 because the measurements are insufficient in number and inconsistent with the other measurements surrounding gap B. However, gap B pressure measurements are included in table V. For test 12, PG103 in gap B near the windward tangent line is 30 percent higher than the adjacent surface pressure of PS72, and this seems physically impossible.

The circumferential gap heating for gaps A and B are presented in the lower plots in figure 33. The surface heating, shown by the closed symbols, was about constant for the circumferential distance covered by the two instrumented tiles from $s/S_R = -0.19$ to 0.60. The surface heating was obtained on the tile at $x/R_n = 26.2$. The average gap heating was an order of magnitude below the reference surface heating, but maximum gap heating occurred at the intersection of longitudinal and circumferential gaps forming what is termed a T-gap, shown in the sketch in figure 33. Local flow, ingested into the longitudinal gap, impinges on the transverse wall of the circumferential gaps and causes large localized gap heating on the transverse wall. This same gap-flow phenomenon has been the subject of many gap studies with flat tiles. (See, for example, refs. 4–8.)

The T-gap impingement heating was obtained in gap A at the two locations of $s/S_R = 0$ and 0.45. The impingement heating for the T-gap at $s/S_R = 0$ increased with α more than at $s/S_R = 0.45$ because the longitudinal gap at $s/S_R = 0$ was more aligned with the local flow. Generally, as α increased, the gap heating nearest the windward pitch plane ($s/S_R = -0.19$) increased but the heating nearer the side at $s/S_R = 0.6$ decreased, indicating that surface flow ingestion into the circumferential gap decreased with increasing s/S_R.

Three T-gap locations are included in gap B at $s/S_R = -0.19, 0.21$, and 0.60, as shown by the sketch in figure 33. There was no increase in gap heating associated with the T-gap at $s/S_R = -0.19$, but the reason for low gap heating is unknown. However, the measured gap pressure, as indicated earlier, was unexplainably high at that location. The gap-heating profile at the T-gap locations of $s/S_R = 0.21$ and 0.60 differed from that of gap A because in gap B the heating was measured on the downstream wall of the instrumented tiles adjacent to the T-gaps. Overall, the heating in gap B nearest the windward pitch plane ($s/S_R = -0.19$) increased with α, and the gap heating toward the side of the model ($s/S_R = 0.60$) decreased in a manner similar to that for gap A. The gap heating measured with Gardon gauges (represented by the cross-filled symbols) agreed with the thermocouple data on the opposite wall of the gap.

The heating distributions in longitudinal gaps at $s/S_R = -0.19$, 0.21, and 0.60 are presented as a function of ℓ/L in figure 34. At $s/S_R = -0.19$, which was near the windward pitch plane, the gap heating was about 1 to 5 percent of the reference surface heating. For configuration 2, the length of the longitudinal gaps was one tile long ($L = 6$ in.) compared with the continuous longitudinal gaps for configuration 1. The gap heating was much less for the shorter longitudinal gap of configuration 2 than for the longer gap of configuration 1 (fig. 29). Apparently, the difference in gap heating between configurations 2 and 1 was caused by the reduced flow penetration into the shorter longitudinal gap of configuration 2. In figure 34 for the longitudinal gap at $s/S_R = 0.21$, the gap heating was higher than that obtained at $s/S_R = -0.19$. The gap heating at $s/S_R = 0.6$ was low at the front end of the longitudinal gap, but the heating increased by at least an order of magnitude in the rear half of the gap to about 20 percent of the surface reference heating. Apparently, this increase in heating was produced by greater flow penetration into the gap that was caused by the local maximum surface pressure gradient at $s/S_R = 0.60$. (See fig. 23(b).)

Typical gap pressure and heating distributions for circumferential and longitudinal gaps are presented as a function of gap depth in figures 35 and 36, respectively. In figure 35, gap pressure and heating near the T-gap locations in gap A are plotted as a function of z/D. The gap pressure was about constant with gap depth at $s/S_R = -0.07$ and 0.36 where the measurements were obtained on the upstream wall of gap A. The gap heating, presented in the lower plots in figure 35, was obtained near the flow-impingement region of the T-gaps. At a gap depth of $z/D = 0.2$, the gap heating was approximately twice the surface reference heating. The gap heating decreased linearly with depth on the logarithm scale and did not vary significantly with angle of attack. In figure 36, the gap heating is presented as a function of gap depth in the longitudinal gaps at $\ell/L = 0.275$ and $s/S_R = -0.19, 0.21$, and 0.60. Generally, the gap heating varied inversely with depth into the gaps for configuration 2 in a manner similar to that for configuration 1.

Effects of forward-facing steps. The basic aluminum tile array on the present model was fabricated in a manner to ensure machine precision in the outer mold line of the tiles. However, the instrumented sheet-metal tiles were worked by hand to align them within the array of precision tiles. Therefore, in configuration 2 the tiles were inadvertently installed with misalignment, and two tests (tests 15 and 16) were made before tile-to-tile forward-facing steps were discovered. (Tests are not chronologically numbered.) Misalignment of these curved tiles on such a large-scale model was difficult to detect, but the irregular gap-heating distribution suggested the tile misalignment. Upon closer examination, the forward-facing steps were estimated to be between 0.015 and 0.035 in. The instrumented tiles were then reinstalled and shims were adjusted to minimize the tile misalignment to eliminate forward-facing steps.

A comparison of the gap pressure and heating distribution in the circumferential gaps A and B with and without the steps (tests 16 and 11, respectively) are presented in figure 37. The sketch in figure 37 shows the approximate location where the forward-facing steps were measured for each gap. The surface pressure and heating were not affected by the steps, and the gap pressure showed no significant effects from the tile-to-tile steps. In gap A at $s/S_R = -0.12$ and 0.22, the gap heating was increased by factors of about 2 and 3, respectively, because of the tile steps. In gap B, similar increases in gap heating were also obtained because of the steps at $s/S_R = 0$ and 0.35. The increases in gap heating near the steps were caused by increased local pressure on the raised portion of the tile that increased flow penetration into the gaps. It is interesting to note that the magnitude of the peak heating at the T-gap locations was not affected by the tile-to-tile steps.

Overall, the test results for configuration 2 show that the gap heating for configuration 2 was much lower than the surface reference heating. The regions of greatest gap heating were caused by the impingement heating at T-gaps and forward-facing steps. This was true in the case of earlier studies with flat tile arrays (refs. 4–8) and in postflight tile-damage reports for the early Shuttle flights described in reference 20.

Effects of Flow Stoppers

In this study, discrete "flow stoppers" (gap filler) were installed in selected gap locations for both test configurations. The purpose was to determine if the basic gap flow pattern could be significantly altered and the gap heating reduced. The flow stoppers consisted of fibrous quartz packed into the full depth of the gaps for a length along the gap of about 0.3 in. A form was used to contain the fiber column, and a liquid quartz adhesive was poured into the form to bind the fibers and to shape the outer edge flush with the outer mold line of the model. The flow stoppers appeared to survive each test, but they were not absolute seals and they were not examined near the bottom of the gaps.

Configuration 1. Flow stoppers were used with configuration 1 in three tests. In test 7, the flow stoppers were placed in the longitudinal gap at $s/S_R = 0$ upstream of circumferential gaps A and B. The effect of flow stoppers in test 7 on the circumferential gap pressure and heating is presented in figure 38 for comparison with data obtained in test 2 without flow stoppers. The locations of the stoppers are shown in the sketch. The gap pressures for gap A were not affected, but the gap pressures for gap B were slightly increased. The corresponding gap heating indicates conflicting results. The gap heating in gap A at $s/S_R = 0.3$ decreased because of flow stoppers, but the heating at $s/S_R \geq 0.5$ increased. In gap B the gap heating in the entire gap decreased by a factor of about 5 because of the flow stoppers. In subsequent tests 8 and 9, additional stoppers were installed in gaps A and B at s/S_R locations of 0.45 and 0.95, respectively. The test results are more complex and no further data plots are presented. The gap heating was expected to decrease when stoppers were installed. However, the increases in gap heating that occurred may have resulted from increased sensitivity to slight misalignments in the tile array discussed earlier or from complex changes in the basic gap flow pattern.

Configuration 2. In configuration 2, the flow stoppers were placed upstream of each T-gap location as shown in the sketch in figure 39. This arrangement provided a continuous circumferential gap without the interruption of the T-gap flow impingement. The effects of the flow stoppers on the circumferential gap pressure and heating are presented for test 17 in figure 39 for comparison with data obtained in test 11 without flow stoppers. The pressure for gap A was not affected by the flow stoppers. The gap heating in gaps A and B was reduced on the average about an order of magnitude. Also, the peak heating at the T-gaps in gap A was eliminated. The effects of the flow stoppers on the gap pressure and heating distributions through the gap depth in the T-gap locations are further illustrated in figure 40. The gap heating at $s/S_R = 0$ and 0.45 was reduced by 1 or 2 orders of magnitude when using discrete flow stoppers in critical locations. Thus, a limited use of flow stoppers or gap filler in longitudinal gaps could reduce gap heating in open circumferential gaps in regions of high surface pressure gradients.

Concluding Remarks

Surface and gap pressures and heating-rate distributions were obtained for simulated thermal protection system (TPS) tile arrays on the curved-surface test apparatus of the Langley 8-Foot High-Temperature Tunnel. Tile configurations representing two different chine radii were tested at nominal angles of attack of 7°, 10°, and 13° and unit Reynolds numbers from 0.371×10^6 to 1.400×10^6 per foot. The tests were made at a nominal Mach number of 6.6 and a nominal total temperature of 3400°R. Aerodynamic heating rates were determined from thin-wall metallic tiles located in the chine region to assess the effects of gap heating with and without filler material, and the pressures were obtained from orifices in the surrounding solid tiles of the array.

The results indicated that the chine gap pressures varied inversely with gap width because larger gap widths allowed greater venting from the gap to the lower model side pressures. Lower gap pressures caused greater flow ingress from the surface and increased gap heating. Generally, gap heating was greater in the longitudinal gaps than in the circumferential gaps. Gap heating decreased with increasing gap depth. Circumferential gap heating at the mid-depth was generally less than about 10 percent of the external surface value. Gap heating was most severe at local T-gap junctions and tile-to-tile forward-facing steps that caused the greatest heating from flow impingement. The use of flow stoppers at discrete locations reduced heating in most gaps but increased heating in others. A limited use of flow stoppers or gap filler in longitudinal gaps could reduce gap heating in open circumferential gaps in regions of high surface pressure gradients.

NASA Langley Research Center
Hampton, VA 23665-5225
March 29, 1990

References

1. Anderson, Roger A.; Brooks, William A., Jr.; Leonard, Robert W.; and Maltz, Joseph: Structures—A Technology Overview. *Astronaut. & Aeronaut.*, vol. 9, no. 2, Feb. 1971, pp. 38–47.
2. Emde, Wendall D.: Thermal Protection System for the Shuttle Orbiter. *Bicentennial of Materials Progress, Volume 21 of National SAMPE Symposium and Exhibition*, Soc. for the Advancement of Material & Process Engineering, 1976, pp. 964–978.
3. Foster, Thomas F.; Lockman, William K.; and Grifall, William J.: *Thermal Protection System Gap Heating Rates of the Rockwell International Flat Plate Heat Transfer Model* (OH2A/OH2B). NASA CR-134077, 1973.
4. Dunavant, James C.; and Throckmorton, David A.: Aerodynamic Heat Transfer to RSI Tile Surfaces and Gap Intersections. *J. Spacecr. & Rockets,* vol. 11, no. 6, June 1974, pp. 437–440.
5. Weinstein, Irving; Avery, Don E.; and Chapman, Andrew J.: *Aerodynamic Heating to the Gaps and Surfaces of Simulated Reusable-Surface-Insulation Tile Arrays in Turbulent Flow at Mach 6.6.* NASA TM X-3225, 1975.
6. Avery, Don E.: *Aerodynamic Heating in Gaps of Thermal Protection System Tile Arrays in Laminar and Turbulent Boundary Layers.* NASA TP-1187, 1978.
7. Avery, Don E.: *Experimental Aerodynamic Heating to Simulated Space Shuttle Tiles in Laminar and Turbulent Boundary Layers With Variable Flow Angles at a Nominal Mach Number of 7.* NASA TP-2307, 1985.
8. Christensen, H. E.; and Kipp, H. W.: *Data Correlation and Analysis of Arc Tunnel and Wind Tunnel Tests of RSI Joints and Gaps. Volume I—Technical Report.* NASA CR-134345, 1974.
9. Bertin, John J.; and Goodrich, Winston D.: Aerodynamic Heating for Gaps in Laminar and Transitional Boundary Layers. AIAA-80-0287, Jan. 1980.
10. Throckmorton, David A.: *Pressure Gradient Effects on Heat Transfer to Reusable Surface Insulation Tile-Array Gaps.* NASA TN D-7939, 1975.
11. Rochelle, W. C.; Battley, H. H.; Hale, W. M.; Gallegos, J. J.; and Kimbrough, B. S.: Arc-Jet Test and Analysis of Orbiter TPS Inter-Tile Heating in High Pressure Gradient Flow. AIAA Paper 78-845, May 1978.
12. Scott, Carl D.; and Maraia, Robert J.: Gap Heating With Pressure Gradients. AIAA Paper 79-1043, June 1979.
13. Petley, D. H.; Smith, D. M.; Edwards, C. L. W.; and Carlson, A. B.: *Analysis of Gap Heating Due to Stepped Tiles in the Shuttle Thermal Protection System.* NASA TP-2209, 1983.
14. Dotts, Robert L.; Smith, James A.; and Tillian, Donald J.: Space Shuttle Orbiter Reusable Surface Insulation Flight Results. *Shuttle Performance: Lessons Learned,* James P. Arrington and Jim J. Jones, compilers, NASA CP-2283, Part 2, 1983, pp. 949–966.
15. Neuenschwander, W. E.; McBride, D. U.; and Armour, G. A.: Shuttle TPS Thermal Performance and Analysis Methodology. *Shuttle Performance: Lessons Learned,* James P. Arrington and Jim J. Jones, compilers, NASA CP-2283, Part 2, 1983, pp. 1025–1064.
16. Albertson, Cindy W.: *Aerothermal Evaluation of a Spherically Blunted Body With a Trapezoidal Cross Section in the Langley 8-Foot High-Temperature Tunnel.* NASA TP-2641, 1987.
17. Craig, Mark K.: Shuttle Launch Debris—Sources, Consequences, Solutions. *Shuttle Performance: Lessons Learned,* James P. Arrington and Jim J. Jones, compilers, NASA CP-2283, Part 1, 1983, pp. 159–185.
18. Deveikis, William D.; and Hunt, L. Roane: *Loading and Heating of a Large Flat Plate at Mach 7 in the Langley 8-Foot High-Temperature Structures Tunnel.* NASA TN D-7275, 1973.
19. Leyhe, E. W.; and Howell, R. R.: *Calculation Procedure for Thermodynamic, Transport, and Flow Properties of the Combustion Products of a Hydrocarbon Fuel Mixture Burned in Air With Results for Ethylene-Air and Methane-Air Mixtures.* NASA TN D-914, 1962.
20. Ames Research Staff: *Equations, Tables, and Charts for Compressible Flow.* NACA Rep. 1135, 1953. (Supersedes NACA TN 1428.)
21. Kays, W. M.: *Convective Heat and Mass Transfer.* McGraw-Hill Book Co., Inc., c.1966.

Table I. Location of Model Instrumentation for Configuration 1

(a) Smooth side

Name	x/R_n	S_R, in.	s/S_R	z/D
Pressure orifice				
P2	2.88	4.77	−0.04	0
P4	6.88	4.96	−.36	
P16	10.88	5.14	−.66	
P18	16.55	5.40	−1.05	
P33	21.05	5.61	−1.34	
P35	25.55	5.82	−1.60	
P36			−.89	
P37			−.43	
P38			0	
P39			.25	
P40			.50	
P41			.75	
P42			1.00	
P44	↓	↓	1.98	
P51	30.05	6.03	−1.92	
P53	34.55	6.24	−2.08	↓
Gardon heat-flux gauge				
Q2	3.21	4.79	−0.06	0
Q4	7.21	4.97	−.39	
Q16	11.21	5.16	−.69	
Q18	16.88	5.42	−1.08	
Q33	21.38	5.63	−1.36	
Q35	25.88	5.84	−1.62	
Q36			−.86	
Q37			−.43	
Q38			0	
Q39			.25	
Q40			.50	
Q41			.75	
Q42			1.00	
Q44	↓	↓	1.99	
Q51	30.38	6.04	−1.87	
Q53	34.88	6.25	−2.10	↓
Backside thermocouple				
QW1	5.21	4.88	−0.23	0
QW2	7.21	4.97	−.26	
QW3	9.21	5.06	−.54	
QW4	14.05	5.29	−.89	
QW5	16.88	5.42	−.86	
QW7	19.13	5.52	−1.22	
QW8	23.63	5.73	−1.49	
QW9	28.13	5.94	−1.75	
QW10	32.63	6.15	−1.98	
QW11	34.88	6.25	−1.87	
QW12	34.88	6.25	−1.56	↓
Coaxial thermocouple				
QX41	34.88	6.25	−0.61	0
QX42	34.88	6.25	−.37	0
QX43	34.88	6.25	0	0

Table I. Continued

(b) Tile side

Name	x/R_n	S_R, in.	s/S_R	ℓ/L	z/D
Pressure orifice					
PS1	23.83	5.74	−0.13	−0.31	0
PS2	23.96	5.75	.14	−.24	
PS3			.32		
PS4			.50		
PS5			.68		
PS6	↓	↓	.86	↓	
PS7	23.90	5.74	1.12	−.27	
PS8	25.25	5.79	−.60	.21	
PS9			−.33	.21	
PS10			−.13	.21	
PS11	↓	↓	1.11	.24	
PS12	25.92	5.84	−.13	.71	
PS13	25.92	5.84	1.11	.75	
PS14	25.92	5.84	1.44	.72	
PS15	26.93	5.88	.14	1.27	
PS16	26.93		.32		
PS17	26.93		.50		
PS18	26.93		.68		
PS19	26.93	↓	.86	↓	
PS20	26.83	5.88	−.13	1.22	
PS21	26.90	5.88	1.11	1.26	↓
PG31	23.45	5.72	0	0	.50
PG32	24.47	5.77	.14		.50
PG33			.32		.50
PG34			.50		.20
PG35					.50
PG36					.80
PG37			↓		1.00
PG38			.68		.50
PG39	↓	↓	.86	↓	
PG40	24.99	5.80	0	.21	
PG41	24.99	5.80	1.00	.21	
PG42	25.45	5.82	−.60	.46	
PG43			−.33	.46	
PG44			−.13	.46	
PG45			1.11	.50	
PG46	↓	↓	1.44	.47	
PG47	25.88	5.84	0	.71	
PG48	25.88	5.84	1.00	.72	
PG49	26.40	5.86	0	.97	
PG50	26.44	5.86	.14	1.00	
PG51			.32		↓
PG52			.50		.20
PG53					.50
PG54					.80
PG55			↓		1.00
PG56			.68		.50
PG57	↓	↓	.86	↓	.50
PG58	26.85	5.88	1.00	1.23	.50

Table I. Concluded

(b) Concluded

Name	x/R_n	S_R, in.	s/S_R	ℓ/L	z/D
Backside thermocouple					
QS1	24.95	5.79	0.14	0.25	0
QS2			.32		
QS3			.50		
QS4			.68		
QS5	↓	↓	.86	↓	
QS6	25.44	5.82	.50	.50	
QS7	25.92	5.84	.50	.75	↓
QG11	24.45	5.77	.14	0	.50
QG12			.32		.50
QG13			.50		.20
QG14			.50		.50
QG15			.50		.80
QG16			.68		.50
QG17	↓	↓	.86	↓	
QG18	24.64	5.78	0	.08	
QG19	24.64	5.78	1.00	.08	
QG20	24.96	5.79	0	.25	
QG21	24.96	5.79	1.00	.25	↓
QG22	25.46	5.82	0	.50	.20
QG23					.50
QG24					.80
QG25			↓		.90
QG26			1.00		.20
QG27					.50
QG28					.80
QG29	↓	↓	↓	↓	.90
QG30	25.95	5.84	0	.71	.20
QG31			0		.50
QG32			0		.80
QG33			1.00		.20
QG34			1.00		.50
QG35	↓	↓	1.00	↓	.80
QG36	26.27	5.85	0	.92	.50
QG37	26.27	5.85	1.00	.92	
QG38	26.44	5.86	.14	1.00	
QG39			.32		↓
QG40			.50		.20
QG41			.50		.50
QG42			.50		.80
QG43			.68		.50
QG44	↓	↓	.86	↓	.50
Gardon heat-flux gauge					
QG1	25.63	5.82	0	0.60	0.50
QG2	25.12	5.80	1.00	.33	.50

Table II. Location of Model Instrumentation for Configuration 2

(a) Smooth side

Name	x/R_n	S_R, in.	s/S_R	z/D
Pressure orifice				
P14	6.88	7.14	−0.06	0
P31	16.55	11.09	−.19	
P42	25.55	14.78	1.39	
P44			1.00	
P45			.75	
P46			.50	
P47			.25	
P48			0	
P49	↓	↓	−.25	
P67	34.55	18.46	−.28	↓
Gardon heat-flux gauge				
Q14	7.21	7.27	−0.06	0
Q31	16.88	11.23	−.19	
Q42	25.88	14.91	1.39	
Q44			1.00	
Q45			.75	
Q46			.50	
Q47			.25	
Q48			0	
Q49	↓	↓	−.25	
Q67	34.88	18.60	−.28	↓
Backside thermocouple				
QW31	3.21	5.64	0.04	0
QW32	5.21	6.46	−.02	
QW33	9.21	8.09	−.10	
QW34	11.21	8.91	−.13	
QW35	14.05	10.07	−.16	
QW36	16.88	11.23	−.19	
QW37	19.13	12.15	−.21	
QW38	21.38	13.07	−.22	
QW39	23.63	13.99	−.24	
QW40	28.13	15.84	−.26	
QW41	30.38	16.67	−.27	
QW42	32.63	17.68	−.27	
QW43	34.88	18.60	−.21	
QW44	34.88	18.60	−.10	↓
Coaxial thermocouple				
QX51	34.88	18.60	0	0
QX52	34.88	18.60	.25	0
QX53	34.88	18.60	.50	0

Table II. Continued

(b) Tile side

Name	x/R_n	S_R, in.	s/S_R	ℓ/L	z/D
Pressure orifice					
PS61	25.18	14.63	−0.14	−0.24	0
PS62			−.07		
PS63			.05		
PS64			.13		
PS65			.21		
PS66			.29		
PS67			.37		
PS68			.50		
PS69	↓	↓	.59	↓	
PS70	26.18	15.03	−.22	.25	
PS71	26.18	15.03	.66	.26	
PS72	28.18	15.85	−.06	1.26	
PS73			.11		
PS74			.24		
PS75	↓	↓	.49	↓	↓
PG81	25.18	14.63	0	−.26	.50
PG82	25.18	14.63	.45	−.27	.50
PG83	25.67	14.83	−.14	0	.50
PG84			−.07		.26
PG85					.50
PG86					.74
PG87			↓		1.00
PG88			.04		.50
PG89			.12		.26
PG90					.50
PG91					.74
PG92			↓		1.00
PG93			.20		.50
PG94			.28		.50
PG95			.36		.26
PG96					.50
PG97					.75
PG98			↓		1.00
PG99			.49		.43
PG100	↓	↓	.58	↓	.44
PG101	26.14	15.02	−.19	.23	.47
PG102	26.14	15.02	.60	.23	.48
PG103	27.68	15.65	−.06	1.00	.50
PG104			.12		.52
PG105			.25		.52
PG106	↓	↓	.50	↓	.51
Backside thermocouple					
QS51	26.22	15.05	−0.15	0.28	0
QS52			−.08		
QS53			−.01		
QS54			.08		
QS55			.17		
QS56			.25		
QS57	↓	↓	.32	↓	↓

Table II. Continued

(b) Continued

Name	x/R_n	S_R, in.	s/S_R	ℓ/L	z/D
Backside thermocouple					
QS58	26.22	15.05	0.40	0.28	0
QS59	26.22	15.05	.48	.28	
QS60	26.22	15.05	.56	.28	
QS61	26.67	15.24	−.01	.50	
QS62	26.67	15.24	.40	.50	
QS63	27.10	15.41	−.02	.72	
QS64	27.10	15.41	.39	.72	↓
QG71	25.67	14.83	−.15	0	.50
QG72			−.07		.50
QG73			0		.20
QG74			0		.50
QG75			0		.80
QG76			.09		.50
QG77			.19		
QG78			.26		
QG79			.34		↓
QG80			.42		.20
QG81			.42		.50
QG82			.42		.80
QG83			.50		.50
QG84	↓	↓	.57	↓	
QG85	25.84	14.90	−.18	.08	
QG86			.21		
QG87			.22		
QG88	↓	↓	.60	↓	↓
QG89	26.27	15.07	−.18	.29	.20
QG90					.50
QG91					.80
QG92			↓		.90
QG93			.21		.20
QG94					.50
QG95					.80
QG96			↓		.90
QG97			.21		.20
QG98					.50
QG99					.80
QG100			↓		.90
QG101			.60		.20
QG102					.50
QG103					.80
QG104	↓	↓	↓	↓	.90
QG105	26.70	15.25	−.19	.50	.50
QG106			.20		
QG107			.21		
QG108	↓	↓	.59	↓	
QG109	27.14	15.43	−.19	.72	
QG110			.19		
QG111			.20		
QG112	↓	↓	.59	↓	↓

Table II. Concluded

(b) Concluded

Name	x/R_n	S_R, in.	s/S_R	ℓ/L	z/D
Backside thermocouple					
QG113	27.51	15.58	−0.19	0.92	0.50
QG114			.19		
QG115			.20		
QG116	↓	↓	.58	↓	
QG117	27.68	15.65	−.17	0	
QG118			−.09		
QG119			−.02		
QG120			.07		
QG121			.16		
QG122			.24		
QG123			.32		
QG124			.39		
QG125			.47		
QG126	↓	↓	.55	↓	↓
Gardon heat-flux gauge					
QG3	26.70	15.25	0.59	0.50	0.50
QG4	27.68	15.65	−.10	1.00	.50
QG5	27.68	15.65	.31	1.00	.50

Table III. Test Conditions

Test	$T_{t,c}$, °R	$p_{t,c}$, psia	$p_{t,\infty}$, psia	p_∞, psia	q_∞, psi	M_∞	$N_{\mathrm{Re},\infty}$, ft^{-1}	$(\rho V c_p)_\infty$	α, deg	Remarks
Configuration 1										
1	3370	1500	913	0.185	5.67	6.67	0.851×10^6	2.03	7	
2	3340	1500	875	.184	5.61	6.64	.852	2.02	10	
3	3300	1500	839	.185	5.56	6.60	.857	2.02	13	
4	3390	703	436	.086	2.67	6.69	.397	.95	10	
5	3550	1000	756	.122	3.95	6.84	.559	1.36	10	
6	3430	2480	1610	.304	9.49	6.72	1.400	3.35	10	
7	3350	1480	868	.182	5.54	6.64	.839	1.99	10	Gap filler
8	3480	1480	1020	.181	5.72	6.77	.842	2.00	10	Gap filler
9	3530	1480	1080	.181	5.81	6.82	.828	2.01	10	Gap filler
Configuration 2										
10	3270	1500	811	0.185	5.52	6.57	0.859×10^6	2.02	7	
11	3500	1510	1070	.185	5.89	6.79	.846	2.05	10	
12	3310	1500	846	.185	5.57	6.61	.855	2.02	13	
13	3520	664	485	.081	2.60	6.82	.371	.90	10	
14	3280	1010	555	.125	3.75	6.58	.581	1.37	10	
15	3280	1500	819	.185	5.53	6.58	.859	2.02	7	Forward step
16	3420	1510	967	.185	5.76	6.71	.851	2.04	10	Forward step
17	3190	1500	739	.185	5.40	6.49	.868	2.02	10	Gap filler

Table IV. Model Pressure Data for Configuration 1

Name	Values of p/p_∞ for tests—								
	1	2	3	4	5	6	7	8	9
Smooth-side surface									
P2	4.40	5.14	6.24	5.12	5.27	5.22	5.10	5.35	5.19
P4	3.98	5.62	7.74	5.59	5.47	5.74	5.37	5.69	5.48
P16	4.10	5.98	7.92	6.04	5.81	6.10	5.67	5.97	5.88
P18	3.99	5.31	6.64	5.43	5.23	5.51	5.14	5.59	5.30
P33	4.19	5.41	6.83	5.62	5.45	5.67	5.29	5.53	5.39
P35	4.52	5.83	7.46	6.04	5.90	6.17	5.83	5.79	5.75
P36	4.51	5.87	7.44	6.01	5.90	6.11	5.79	5.73	5.80
P37	4.60	6.01	7.53	6.08	6.04	6.16	5.87	5.66	5.97
P38	4.75	6.21	7.73	6.22	6.12	6.35	6.05	5.95	6.17
P39	4.81	6.12	7.40	6.11	6.01	6.22	5.96	5.90	6.09
P40	4.58	5.50	6.34	5.48	5.42	5.61	5.39	5.27	5.50
P41	3.62	3.98	4.33	4.01	3.95	4.03	3.94	3.91	4.01
P42	2.97	2.81	2.67	2.87	2.83	2.87	2.84	2.87	2.81
P44	2.45	1.57	2.63	2.63	2.53	2.62	2.56	2.56	2.55
P51	4.46	6.04	7.56	6.10	6.10	6.18	5.95	5.79	5.96
P53	4.55	6.27	7.74	6.22	6.31	6.30	6.12	5.97	6.17
P67	.95	.75	.61	.90	.77	.82	.75	.81	.70
Tile-side surface									
PS1	4.56	5.94	7.40	6.05	6.00	6.20	5.87	5.68	5.59
PS2	4.68	6.04	7.40	6.15	6.08	6.23	5.96	5.57	5.64
PS3	4.60	5.75	6.83	5.85	5.80	5.90	5.62	5.53	5.45
PS4	4.30	5.15	5.91	5.16	5.14	5.29	5.05	4.96	
PS5	3.60	4.02	4.42	4.09	4.07	4.11	4.00	3.94	3.84
PS6	3.09	3.26	3.45	3.34	3.34	3.33	3.28	3.26	3.13
PS7	2.62	2.50	2.50	2.58	2.58	2.57	2.51	2.42	2.35
PS8	4.44	5.84	7.42	5.96	5.90	6.15	5.72	5.72	5.59
PS9	4.45	5.86	7.34	5.97	5.90	6.11	5.75	5.63	5.55
PS10	4.52	5.93	7.38	6.05	5.95	6.11	6.30	5.93	5.86
PS11	2.57	2.49	2.51	2.61	2.58	2.49	2.52	2.49	2.42
PS12	4.22	5.58	6.94	5.65	5.63	5.76	5.39	5.37	5.28
PS13	2.66	2.59	2.62	2.68	2.67	2.64	2.62	2.60	2.49
PS14	2.60	2.65	2.61	2.75	2.73	2.72	2.68	2.63	2.58
PS15	4.56	6.00	7.30	6.13	6.03	6.11	5.90	6.08	6.01
PS16	4.49	5.64	6.54	5.77	5.73	5.71	5.57	5.28	5.23
PS17	3.98	4.86	5.64	4.94	5.01	4.90	4.82	4.75	4.65
PS18	3.56	3.99	4.36	4.09	4.10	4.01	3.97	3.90	3.82
PS19	2.78	2.87	2.96	2.92	2.96	2.87	2.88	2.74	2.66
PS20	4.56	6.06	7.53	6.16	6.08	6.25	5.97	5.97	6.14
PS21	2.67	2.62	2.67	2.73	2.74	2.61	2.66	2.65	2.60

Table IV. Concluded

Name	Values of p/p_∞ for tests –								
	1	2	3	4	5	6	7	8	9
Tile gap									
PG31	3.97	4.90	5.99	5.28	5.09	4.87	6.63	9.85	12.82
PG32	4.13	4.88	5.65	5.38	5.20	4.93	4.74	5.48	5.17
PG33	4.13	4.78	5.44	5.24	5.12	4.87	4.72	5.42	5.10
PG34	4.51	5.43	6.33	5.56	5.51	5.64	4.78	3.93	4.97
PG35	4.05	4.66	5.25	5.02	4.93	4.75	4.59	3.92	4.90
PG36	3.89	4.20	4.58	4.74	4.60	4.33	4.53	4.08	4.98
PG37	2.32	2.51	2.70	2.58	2.47	2.40	2.71	2.47	3.09
PG38	3.96	4.50	5.06	4.80	4.72	4.58	4.41	3.91	5.03
PG39	3.46	3.89	4.35	4.07	4.01	4.01	3.70	3.44	4.94
PG40	4.31	5.40	6.67	5.62	5.47	5.62	4.81	5.55	5.18
PG41	2.98	3.16	3.36	3.28	3.23	3.22	3.17	2.98	2.72
PG42	4.41	5.69	7.08	5.98	5.76	5.76	5.41	5.67	5.46
PG43	4.33	5.61	6.99	5.87	5.68	5.73	5.29	5.58	5.41
PG44	4.29	5.59	6.96	5.78	5.58	5.71	5.14	4.95	5.33
PG45	2.91	2.98	3.01	3.11	3.07	3.09	3.00	2.91	2.67
PG46	2.51	2.65	2.74	2.78	2.72	2.62	2.66	2.56	2.39
PG47	3.95	5.06	6.26	5.27	5.09	5.16	5.02	5.32	5.10
PG48	3.00	3.09	3.23	3.23	3.18	3.21	3.17	3.05	2.73
PG49	4.18	5.91	7.63	5.40	5.45	6.58	4.91	12.35	6.83
PG50	3.07	3.45	3.86	3.79	3.56	3.35	3.64	6.61	5.34
PG51	3.01	3.31	3.69	3.62	3.43	3.26	3.55	5.66	5.29
PG52	2.48	2.62	2.82	2.76	2.67	2.69	2.84	2.43	2.97
PG53	2.98	3.16	3.45	3.41	3.26	3.13	3.39	3.12	3.56
PG54	3.00	3.24	2.59	3.38	3.30	3.27	3.21	3.10	3.57
PG55	2.82	2.86	2.97	3.09	2.98	3.02	3.03	4.14	3.59
PG56	3.03	3.18	3.40	3.40	3.27	3.16	3.38	3.05	3.59
PG57	3.00	3.15	3.34	3.31	3.22	3.17	3.29	3.00	3.54
PG58	2.98	3.11	3.27	3.21	3.15	3.20	3.15	3.16	3.07

Table V. Model Pressure Data for Configuration 2

Name	Values of p/p_∞ for tests—							
	10	11	12	13	14	15	16	17
				Smooth-side surface				
P14	3.98	5.70	7.80	6.02	5.69	3.98	5.69	5.56
P31	3.97	5.88	7.10	6.19	6.03	4.17	5.71	5.66
P42	2.07	2.31	2.33	2.20	2.15	2.09	2.22	2.27
P44	2.59	2.86	2.73	2.73	2.78	2.64	2.73	2.83
P45	3.13	3.66	3.91	3.56	3.50	3.23	3.56	3.58
P46	4.05	5.24	6.08	4.98	4.94	4.22	5.18	5.04
P47	4.38	5.90	7.26	5.72	5.67	4.61	5.99	5.73
P48	4.16	5.64	7.36	5.72	5.58	4.49	5.97	5.76
P49	3.64	5.65	7.40	5.79	5.58	4.53	6.02	5.91
P53	1.00	2.33	2.47	1.47	.95	1.02	2.49	1.83
P67	4.26	5.95	7.40	5.94	5.71	4.42	5.99	5.72
				Tile-side surface				
PS61	4.17	5.67	7.45	5.78	5.63	4.52	6.01	5.94
PS62	4.02	5.54	7.20	5.69	5.54	4.42	5.91	5.87
PS63	4.24	5.71	7.37	5.94	5.70	4.58	6.07	5.91
PS64	4.06	5.43		5.63	5.41	4.29	5.78	5.62
PS65	4.18	5.57	7.01	5.79	5.57	4.45	5.85	5.69
PS66	4.25	5.57	6.88	5.90	5.61	4.52	5.85	5.77
PS67	4.09	5.28	6.40	5.68	5.37	4.35	5.54	5.52
PS68	3.80	4.75	5.59	5.23	4.84	4.00	4.98	4.92
PS69	3.67	4.39	5.03	4.90	4.54	3.83	4.60	4.60
PS70	2.33	5.49	7.19	3.10	2.88	4.46	6.04	3.89
PS71	3.34	4.19	4.75	4.56	4.29	3.73	4.42	4.33
PS72	4.17	5.69	7.28	5.80	5.58			5.74
PS73	4.37	5.95	7.46	6.15	5.87	4.59	6.13	6.03
PS74	4.42	5.86	7.27	6.09	5.85	4.64	6.08	5.77
PS75	3.71	4.64	5.57	4.96	4.72	3.92	4.90	4.79
				Tile gap				
PG81	3.94	5.20	6.44	5.53	5.29	4.14	5.45	5.63
PG82	3.80	4.84	5.81	5.19	4.90	4.02	5.13	5.07
PG83	4.05	5.50	7.29	5.63	5.46	4.80	6.44	5.72
PG84	3.96	5.34	6.98	5.56	5.31	4.60	6.23	5.66
PG85	3.95	5.22	6.69	5.49	5.30	4.36	5.85	5.67
PG86	3.94	5.21	6.53	5.46	5.30	4.20	5.61	5.60
PG87	3.85	5.11	6.50	5.26	5.14	4.09	5.55	5.50
PG88	3.86	5.08	6.31	5.40	5.16	4.16	5.45	5.58
PG89	3.47	5.09	6.46	4.89	4.74	4.54	6.27	4.97
PG90	3.87	5.11	6.37	5.37	5.14	4.44	5.85	5.45

Table V. Concluded

Name	Values of p/p_∞ for tests—							
	10	11	12	13	14	15	16	17
				Tile gap (Concluded)				
PG91	3.64	4.90	6.01	5.05	4.85	3.99	5.27	5.23
PG92	3.96	5.17	6.36	5.47	5.24	4.54	5.74	5.59
PG93	4.00	5.24	6.36	5.51	5.31	4.17	5.59	5.43
PG94	3.83	5.06	6.60	5.40	5.10	4.00	5.31	5.15
PG95	3.83	4.91	6.14	5.42	4.98	3.99	5.13	5.04
PG96	3.67	4.68	5.72	5.16	4.76	3.86	4.97	5.04
PG97		4.71	5.80			3.92	5.05	
PG98	3.69	4.75	5.90	5.14	4.79	3.94	5.03	
PG99	3.58	4.57	5.51	5.00	4.67	3.85	4.91	4.54
PG100	3.27	3.86		4.43	4.03	3.43	4.33	4.33
PG101		5.85	7.65			4.85	6.56	
PG102	3.04	3.70	4.14	4.15	3.67	3.14	3.87	4.23
PG103	4.99	7.05	9.44	6.67	6.72	5.58	7.56	5.55
PG104	4.85	6.53	8.53	6.73	6.49	5.22	6.44	5.40
PG105	4.19	4.84	4.89	5.84	5.53	3.61	3.98	4.76
PG106	4.35	5.56	7.01	5.58	5.58	4.79	6.04	4.47

Table VI. Model Heat-Transfer Data for Configuration 1

Name	Stanton numbers $N_{\mathrm{St},\infty} \times 10^3$ for tests—								
	1	2	3	4	5	6	7	8	9
Smooth-side surface									
Q2	2.10	2.39	2.92	2.41	2.56	2.11	2.51	2.36	2.33
Q4	1.65	2.14	2.80	2.29	2.32	1.78	2.22	2.15	2.05
Q16	2.03	2.73	3.56	3.03	3.03	2.26	2.83	2.80	2.66
Q18	1.95	2.67	3.52	2.96	2.97	2.31	2.72	2.75	2.64
Q33	2.18	2.93	3.86	3.30	3.25	2.57	2.94	2.98	2.87
Q35	1.77	2.46	3.40	2.76	2.76	2.55	2.76	2.75	2.66
Q36	2.51	3.21	4.10	3.48	3.48	2.90	3.23	3.20	3.14
Q37	2.70	3.33	4.05	3.58	3.57	2.94	3.33	3.25	3.21
Q38	3.70	4.67	5.62	4.90	4.94	4.13	4.67	4.54	4.51
Q39	3.98	4.68	5.36	5.17	5.11	3.89	5.10		
Q40	2.91	3.22		3.62	3.53		3.18	3.10	
Q41	2.76	2.92	3.10	3.17	3.15		2.98	2.91	2.87
Q42	2.06	1.90	1.79	1.92	1.95	1.64	1.99	1.93	1.88
Q44	1.89	1.94	1.98	2.18	2.13	1.61	2.02	1.96	1.90
Q51	2.79	3.89	5.03	4.06	4.15	3.45	3.80	3.71	3.70
Q53	2.08	2.90	3.64	3.10	3.21	2.55	2.88	2.79	2.81
Tile-side surface									
QS1	3.00	3.74	4.48	4.06	4.05	3.29	3.97	3.78	3.55
QS2	3.23	3.94	4.62	4.30	4.29	3.49	3.72	3.80	3.54
QS3	3.09	3.66	4.11	4.00	3.89	3.33	3.47	3.44	3.17
QS4	2.24	2.71	2.59	2.72	2.69	2.27	2.33	2.30	2.28
QS5	2.11	2.23	2.30	2.36	2.45	1.95	2.17	1.97	2.13
QS6	3.16	3.63	4.07	3.90	3.86	3.22	3.73	3.56	3.32
QS7	2.99	3.45	3.85	3.78	3.69	3.05	3.56	3.40	3.18
Tile gap									
QG1	0.29	0.54	0.79	0.38	0.41	0.62	0.02	0.03	0.01
QG2	.03	.02	.03	.01	.01	.03	.04	.04	.04
QG11									
QG12	.12	.21	.32	.20	.20	.21	.04	.04	.00
QG13	.39	.57	.79	.37	.44	.59	.96	1.11	.35
QG14	.13	.18	.26	.16	.16	.17	.30	.24	.00
QG15	.06	.06	.06	.03	.04	.06	.06	.11	.01
QG16	.17	.21	.25	.12	.17	.18	.54	.73	.14
QG17	.16	.20	.24	.11	.14	.19	.49	.42	.03
QG18	.28	.44	.61	.33	.38	.50	.01	.04	.02
QG19	.14	.18	.21	.07	.11	.18	.30	.18	.02
QG20	.24	.44	.60	.30	.32	.40	.01	.05	.01

Table VI. Concluded

Name	Stanton numbers $N_{St,\infty} \times 10^3$ for tests—								
	1	2	3	4	5	6	7	8	9
Tile gap (Concluded)									
QG21	0.02	0.05	0.04	0.01	0.04	0.06	0.07	0.05	0.05
QG22	1.33	1.98	2.61	1.68	1.84	2.14	1.09	.40	.55
QG23	.31	.56	.79	.42	.46	.62	.02	.02	.01
QG24	.06	.09	.12	.07	.06	.07	.05	.11	.04
QG25	.04	.08	.09	.04	.04	.06	.08	.16	.07
QG26	.13	.07	.10	.04	.05	.09	.09	.25	.53
QG27	.03	.02	.05	.00	.01	.04	.02	.04	.06
QG28	.01	.03	.04	.00	.01	.01	.01	.01	.01
QG29	.02	.01	.02	.01	.00	.01	.02	.02	.02
QG30	1.48	2.13	2.79	1.97	2.06	2.05	1.88	1.14	1.27
QG31	.34	.59	.84	.43	.49	.67	.10	.06	.06
QG32	.05	.09	.15	.04	.08	.08	.07	.16	.10
QG33	.11	.06	.11	.04	.04	.07	.08	.23	.42
QG34	.02	.01	.05	.00	.04	.03	.03	.04	.10
QG35	.01	.00	.02	.02	.01	.01	.02	.02	.03
QG36	.60	1.02	1.41	.69	.81	1.12	1.28	1.61	.05
QG37	.05	.10	.17	.04	.05	.13	.06	.05	.16
QG38	.13	.22	.37	.17	.19	.27	.06	.12	.07
QG39	.14	.36	.51	.22	.29	.37	.06	.08	.05
QG40	.03	.03	.08	.07	.04	.04	.29	.02	.02
QG41	.06	.18	.30	.12	.17	.17	.03	.01	.01
QG42	.07	.15	.17	.11	.12	.17	.08	.02	.01
QG43	.05	.13	.22	.09	.12	.13	.04	.05	.01
QG44	.06	.12	.19	.06	.09	.12	.05	.11	.01

Table VII. Model Heat-Transfer Data for Configuration 2

Name	Stanton numbers $N_{St,\infty} \times 10^3$ for tests—							
	10	11	12	13	14	15	16	17
				Smooth-side surface				
Q14	1.72	2.18	2.89	2.26	2.60	1.87	2.18	2.11
Q31	2.24	3.33	3.93	4.16	3.49	2.31	3.11	2.92
Q42	1.27	1.41	1.39	1.45	1.57	1.37	1.34	1.28
Q44	1.83	1.95	1.86	1.93	2.18	2.00	1.89	1.80
Q45	2.07	2.33	2.38	2.45	2.58	2.25	2.27	2.15
Q46	2.82			3.67	3.74	2.98	3.21	3.11
Q47	2.95	3.58	4.09	4.21	3.97	3.06	3.55	3.51
Q48	2.34	2.95	3.55	3.49	3.29			2.95
Q49	2.56	3.36	4.11	4.03	3.77	2.63	3.35	3.35
Q67	1.97	2.47	2.94	3.08	2.77	2.04	2.56	2.43
				Tile-side surface				
QS51	2.10	2.73	3.31	3.34	3.08	2.18	2.56	2.66
QS52	2.28	2.95	3.57	3.65	3.30	2.34	2.73	2.90
QS53	2.25	2.87	3.57	3.40	3.15	2.27	2.68	2.99
QS54	2.38	2.97	3.57	3.55	3.32			2.97
QS55	2.53	3.08	3.59	3.85	3.55			3.03
QS56	2.58	3.09	3.55	3.85	3.50	2.69	2.95	3.10
QS57	2.61	3.08	3.56	3.88	3.48	2.70	2.89	3.05
QS58		2.87		3.25	3.31	2.55	2.26	
QS59	2.42	2.75	3.15	3.53	3.14	2.48	2.63	2.72
QS60	2.42	2.65	2.90	3.57	3.14	2.46	2.52	2.69
QS61	2.43	3.17	3.84	3.44	3.41	2.46	2.91	3.02
QS62	2.57	3.00	3.38	3.70	3.39	2.70	2.83	2.85
QS63	2.36	2.13	2.44	2.43	2.38	1.67	1.85	2.83
QS64	2.56	2.98	3.37	3.77	3.39	2.68	2.81	2.87
				Tile gap				
QG3	0.05	0.07	0.09	0.04	0.08	0.06	0.06	0.02
QG4	.09	.14	.29	.04	.10	.13	.22	.01
QG5	.21	.34	.62	.19	.28	.66	.93	.06
QG71	.07	.19	.29	.06	.17	.28	.39	.09
QG72	.07	.19	.30	.06	.11	.22	.37	.02
QG73	3.39	5.61	6.96	5.38	5.46	3.89	4.85	.04
QG74	.32	.79	1.10	.42	.70	.52	.89	.02
QG75	.03	.02	.05	.00	.00	.04	.09	.02
QG76	.09	.16	.24	.09	.12	.33	.42	.03
QG77	.10	.16	.21	.11	.14	.40	.59	.02
QG78	.19	.28	.41	.20	.26	.18	.23	.04
QG79	.16	.23	.33	.23	.26	.18	.21	.02
QG80	3.61	4.06	4.54	5.82	4.94	3.74	3.40	.26
QG81	.33	.49	.60	.53	.57	.42	.42	.00

Table VII. Concluded

Name	Stanton numbers $N_{St,\infty} \times 10^3$ for tests—							
	10	11	12	13	14	15	16	17
Tile gap (Concluded)								
QG82	0.03	0.06	0.08	0.00	0.06	0.03	0.06	0.01
QG83	.14	.17	.21	.13	.18	.14	.17	.03
QG84	.06	.06	.02	.07	.07	.15	.16	.00
QG85	.00	.13	.19	.04	.08	.07	.11	.07
QG86	.16	.28	.34	.15	.21	.29	.41	.25
QG87	.19	.27	.36	.15	.24	.28	.41	.27
QG88	.03	.03	.02	.00	.02	.06	.03	.02
QG89	.08	.84	1.06	.98	.99	.70	.84	.20
QG90	.01	.02	.03	.06	.01	.01	.02	.04
QG91	.02	.04	.04	.06	.02	.02	.04	.23
QG92	.05	.05	.06	.00	.02	.01	.04	.47
QG93	.24	.40	.59	.16	.31	.83	1.00	.18
QG94	.07	.12	.15	.07	.10	.14	.19	.13
QG95	.03	.07	.08	.05	.11	.11	.17	.54
QG96	.02	.07	.08	.02	.06	.10	.18	.44
QG97	.41	.59	.83	.28	.49	.99	1.16	.27
QG98	.08	.13	.17	.05	.12	.14	.17	.14
QG99	.06	.10	.14	.06	.07	.13	.19	.44
QG100	.05	.07	.13	.05	.08	.13	.24	.46
QG101	.48	.62	.68	.41	.71	.60	.56	.17
QG102	.02	.01	.01	.00	.02	.00	.02	.03
QG103	.00	.00	.00	.02	.01	.00	.01	.09
QG104	.01	.01	.01	.01	.00	.01	.01	.34
QG105	.02	.02	.05	.01	.02	.05	.03	.02
QG106	.04	.07	.06	.03	.08	.13	.15	.05
QG107	.06	.10	.13	.05	.07	.14	.15	.05
QG108	.06	.10	.12	.04	.07	.09	.10	.08
QG109	.04	.03	.04	.02	.01	.02	.04	.08
QG110	.03	.08	.12	.01	.04	.32	.35	.07
QG111	.06	.10	.14	.04	.10	.37	.39	.08
QG112	.60	.73	.80	.73	.89	.71	.67	.28
QG113	.07	.11	.16	.04	.10	.05	.08	.36
QG114	.28	.41	.62	.35	.37	1.02	1.03	1.83
QG115	.27	.40	.61	.30		.99	1.01	1.01
QG116	.57	.59	.61	.59	.76	.62	.58	.80
QG117	.06	.08	.16	.02	.15	.10	.16	.00
QG118	.05	.11	.25	.04	.07	.14	.24	.02
QG119	.10	.22	.44	.01	.10	.33	.45	.01
QG120	.38	.54	.83	.28	.48	.86	1.05	.00
QG121	.56	.78	1.12	.58	.73	.89	.96	.08
QG122	.37	.43	.56	.42	.48	.67	.68	.14
QG123	.17	.30	.52	.17	.25	.55	.73	.06
QG124	.13	.15	.20	.06	.10	.17	.20	.03
QG125	.21	.22	.22	.19	.23	.21	.27	.02
QG126	.38	.28	.28	.28	.38		.28	.03

Table VIII. Model Reference Conditions

Test	p_{ref}, psia	$\dot{q}_{\text{ref}}$, Btu/ft^2-sec
	Configuration 1	
1	0.832	13.82
2	1.088	17.55
3	1.378	22.33
4	.518	9.76
5	.734	13.94
6	1.855	26.16
7	1.063	17.34
8	1.048	18.24
9	1.050	18.63
	Configuration 2	
10	0.767	13.24
11	1.053	18.82
12	1.368	22.41
13	.466	9.67
14	.701	12.75
15	.833	13.30
16	1.111	18.21
17	1.102	16.54

ORIGINAL PAGE
BLACK AND WHITE PHOTOGRAPH

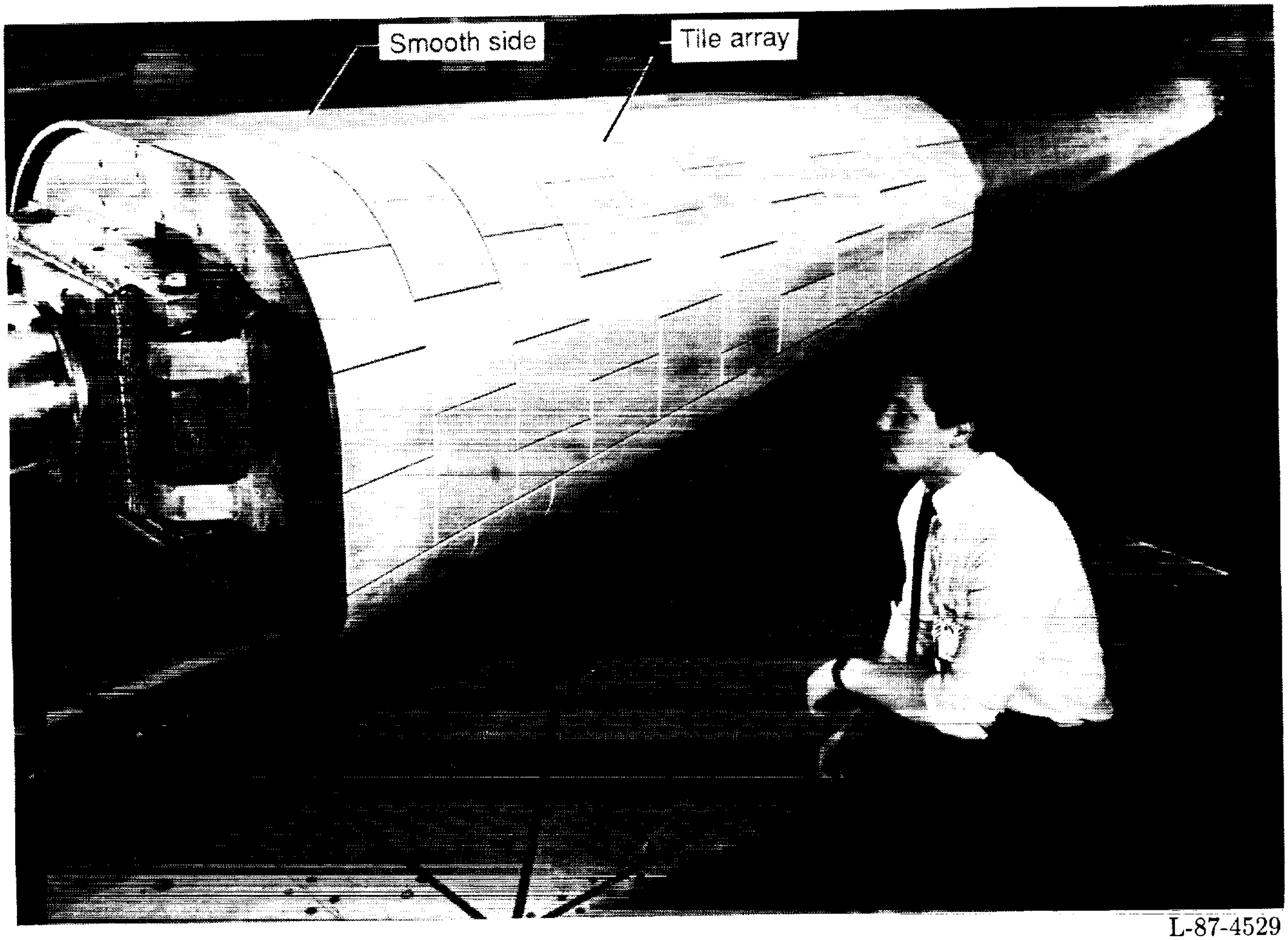

L-87-4529

Figure 1. Simulated Shuttle tiles on curved-surface test apparatus installed in the Langley 8-Foot High-Temperature Tunnel.

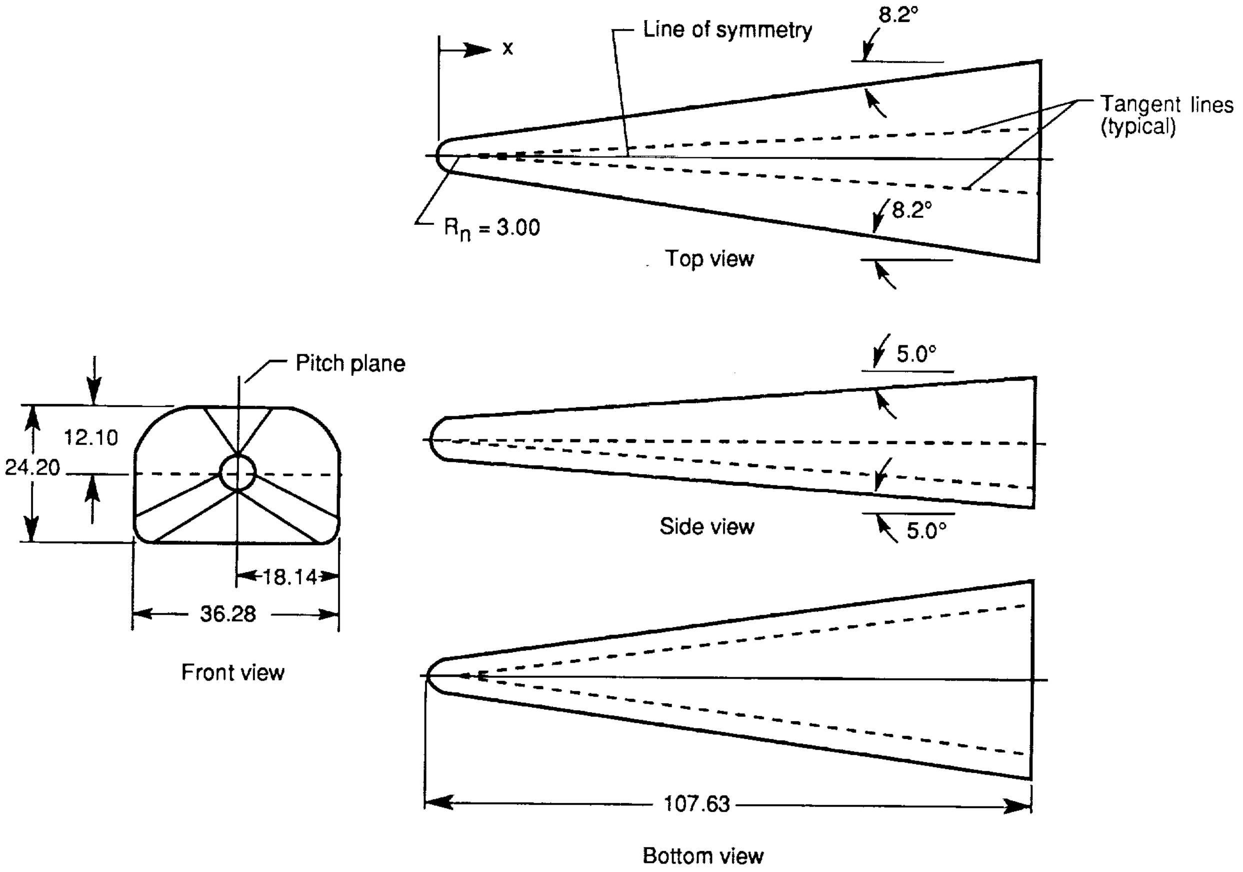

Figure 2. Schematic of model. Linear dimensions are given in inches.

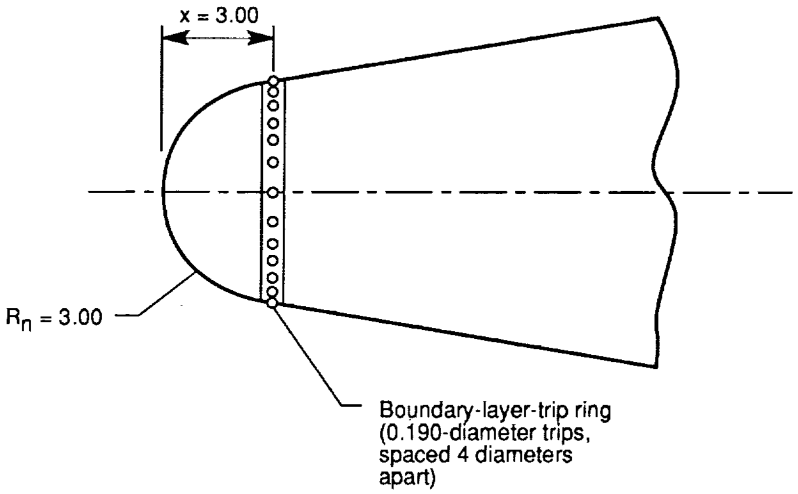

Figure 3. Model nose region showing boundary-layer-trip ring. Dimensions are given in inches.

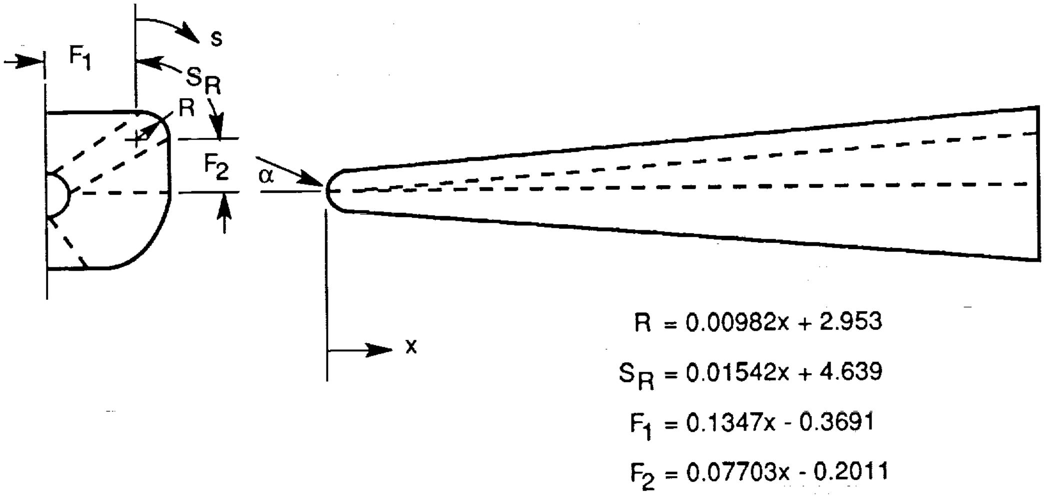

$$R = 0.00982x + 2.953$$
$$S_R = 0.01542x + 4.639$$
$$F_1 = 0.1347x - 0.3691$$
$$F_2 = 0.07703x - 0.2011$$

(a) Configuration 1; small chine.

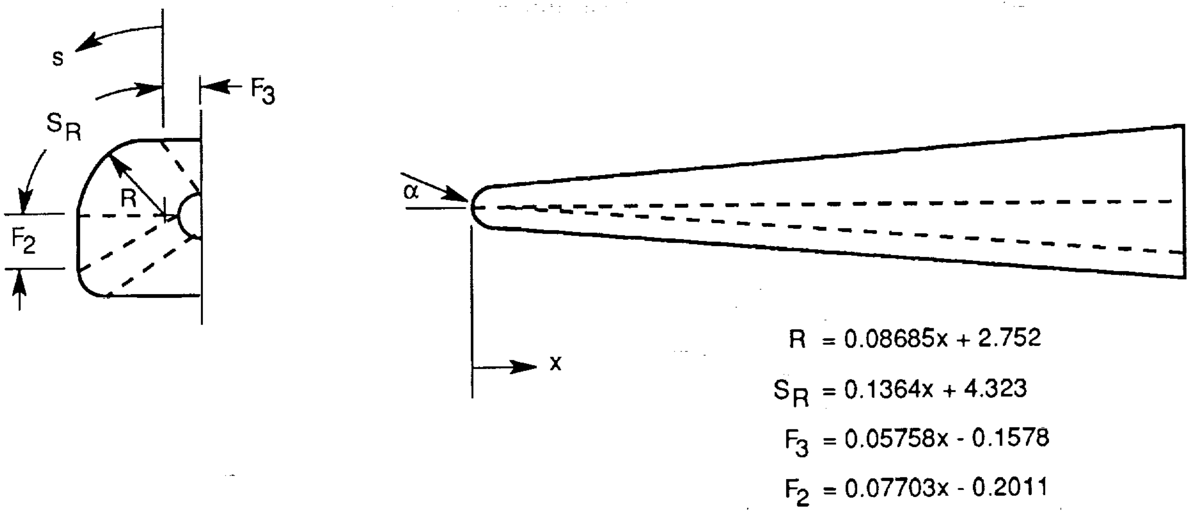

$$R = 0.08685x + 2.752$$
$$S_R = 0.1364x + 4.323$$
$$F_3 = 0.05758x - 0.1578$$
$$F_2 = 0.07703x - 0.2011$$

(b) Configuration 2; large chine.

Figure 4. Schematic of model with shape functions. Dimensions are given in inches.

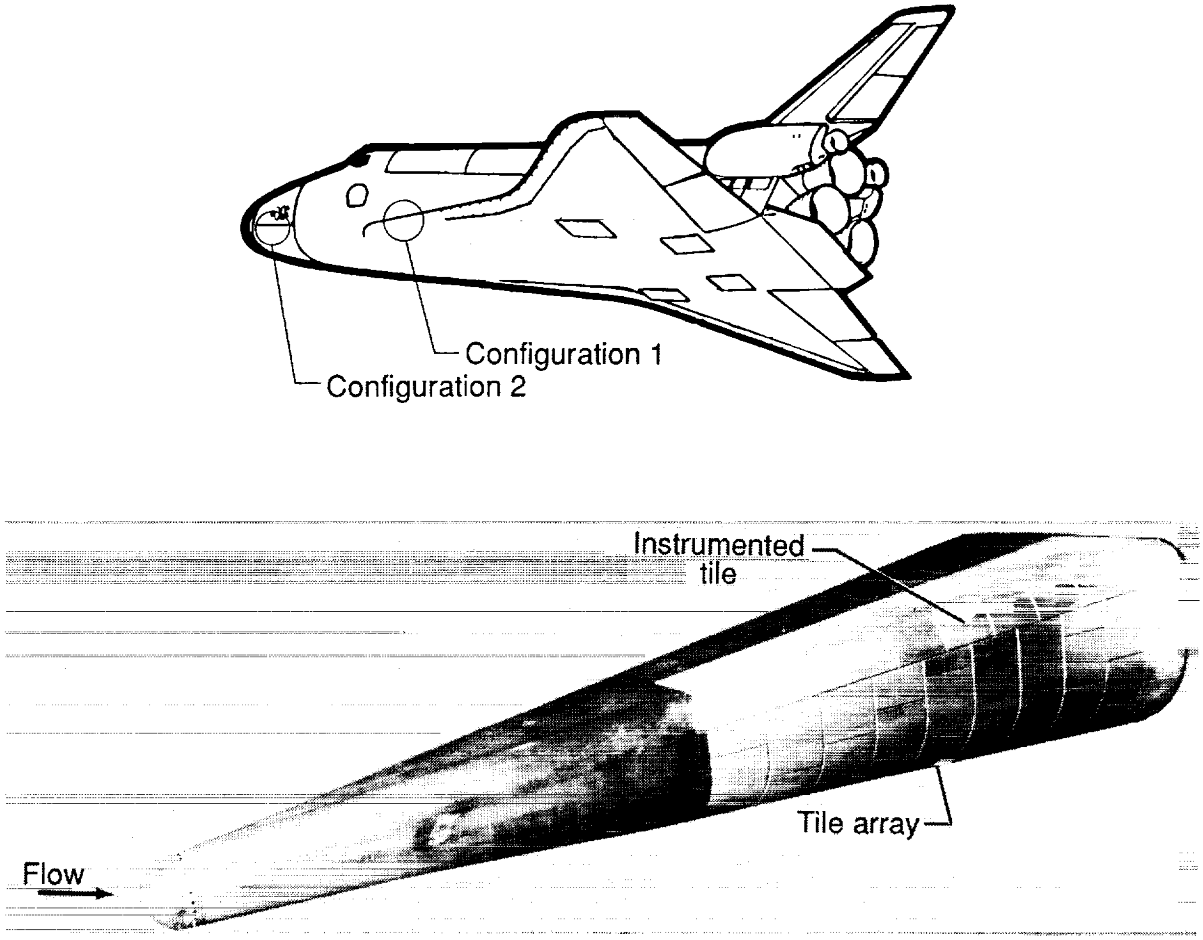

(a) Configuration 1; small chine.

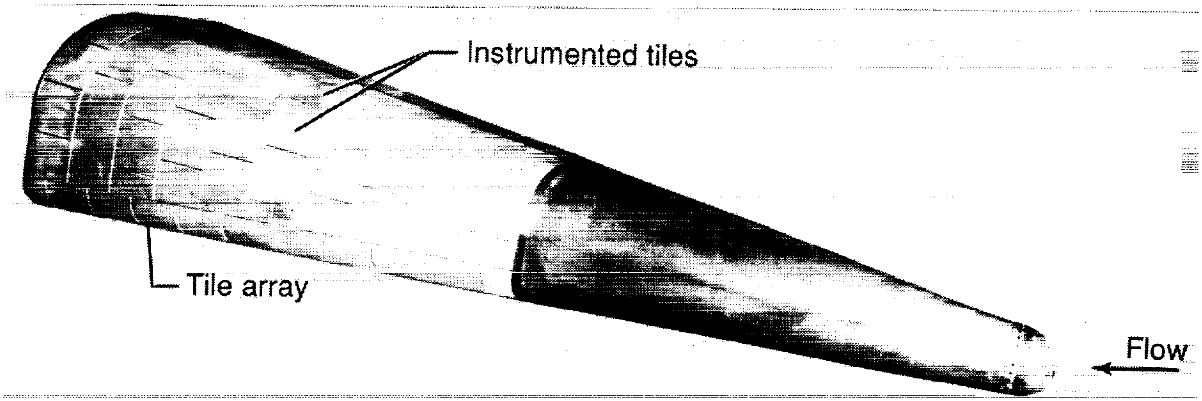

(b) Configuration 2; large chine.

L-90-26

Figure 5. Location of instrumented tiles in model tile array.

ORIGINAL PAGE
BLACK AND WHITE PHOTOGRAPH

L-84-10,028

Figure 6. Small-radius-chine thin-wall tile.

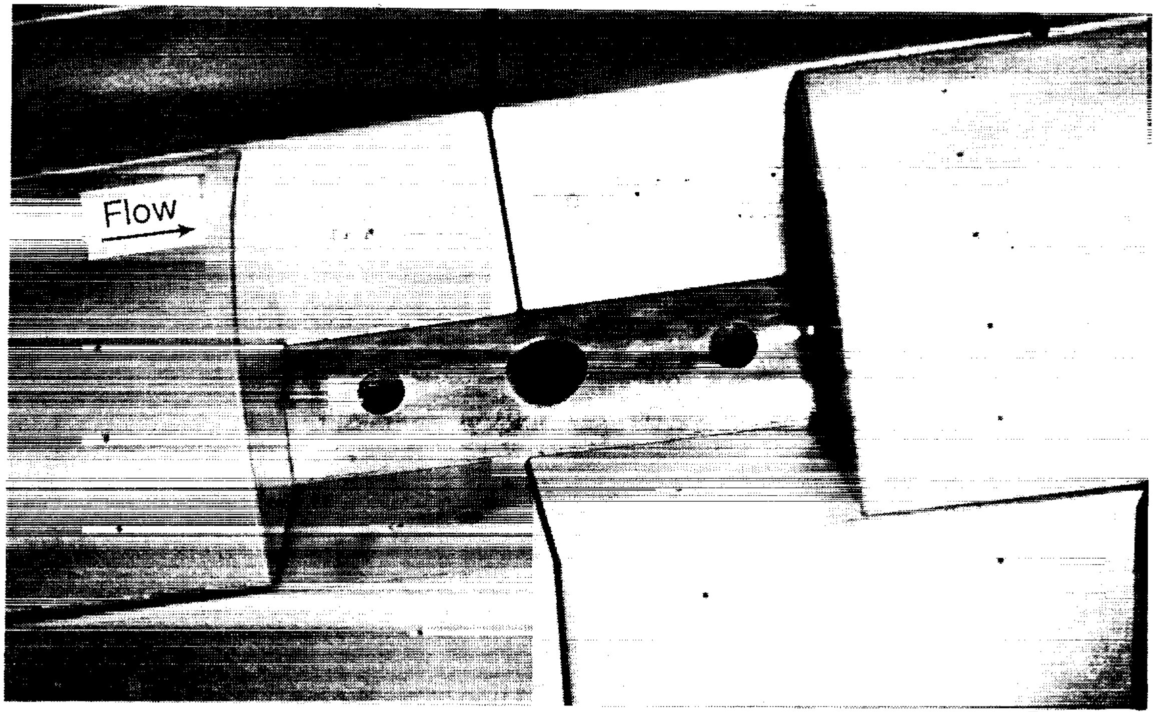

L-87-5449

(a) Tile removed.

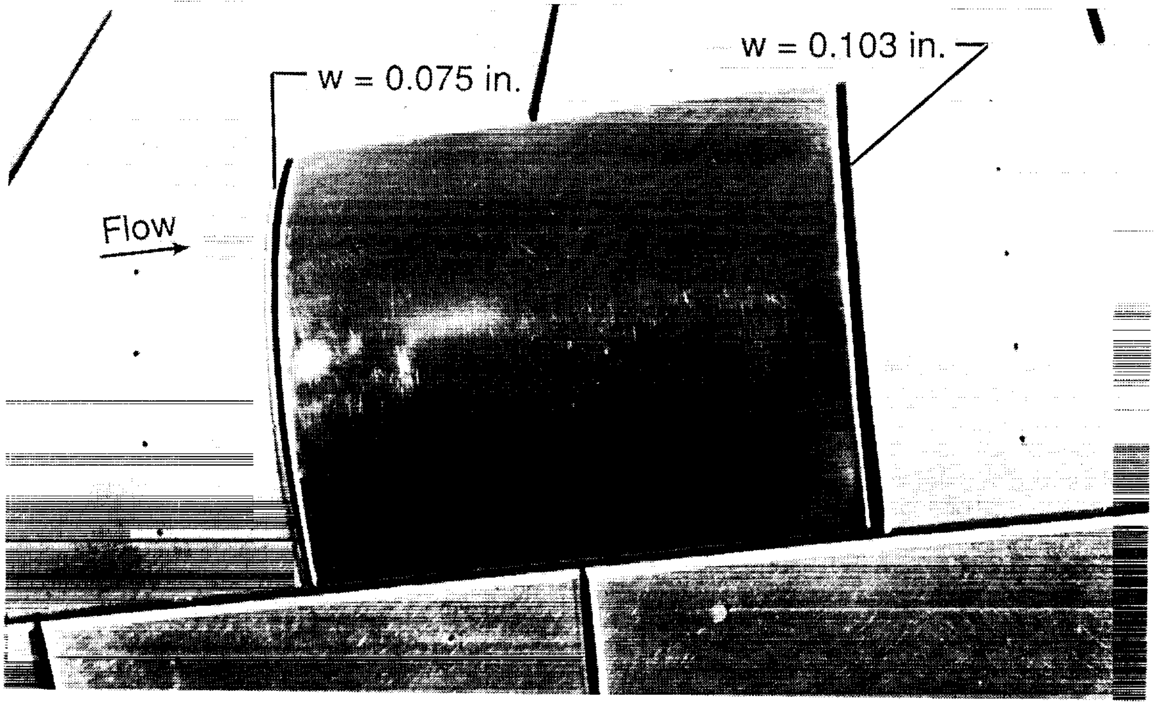

L-87-5445

(b) Tile installed.

Figure 7. Small-radius-chine instrumented region.

ORIGINAL PAGE
BLACK AND WHITE PHOTOGRAPH

ORIGINAL PAGE
BLACK AND WHITE PHOTOGRAPH

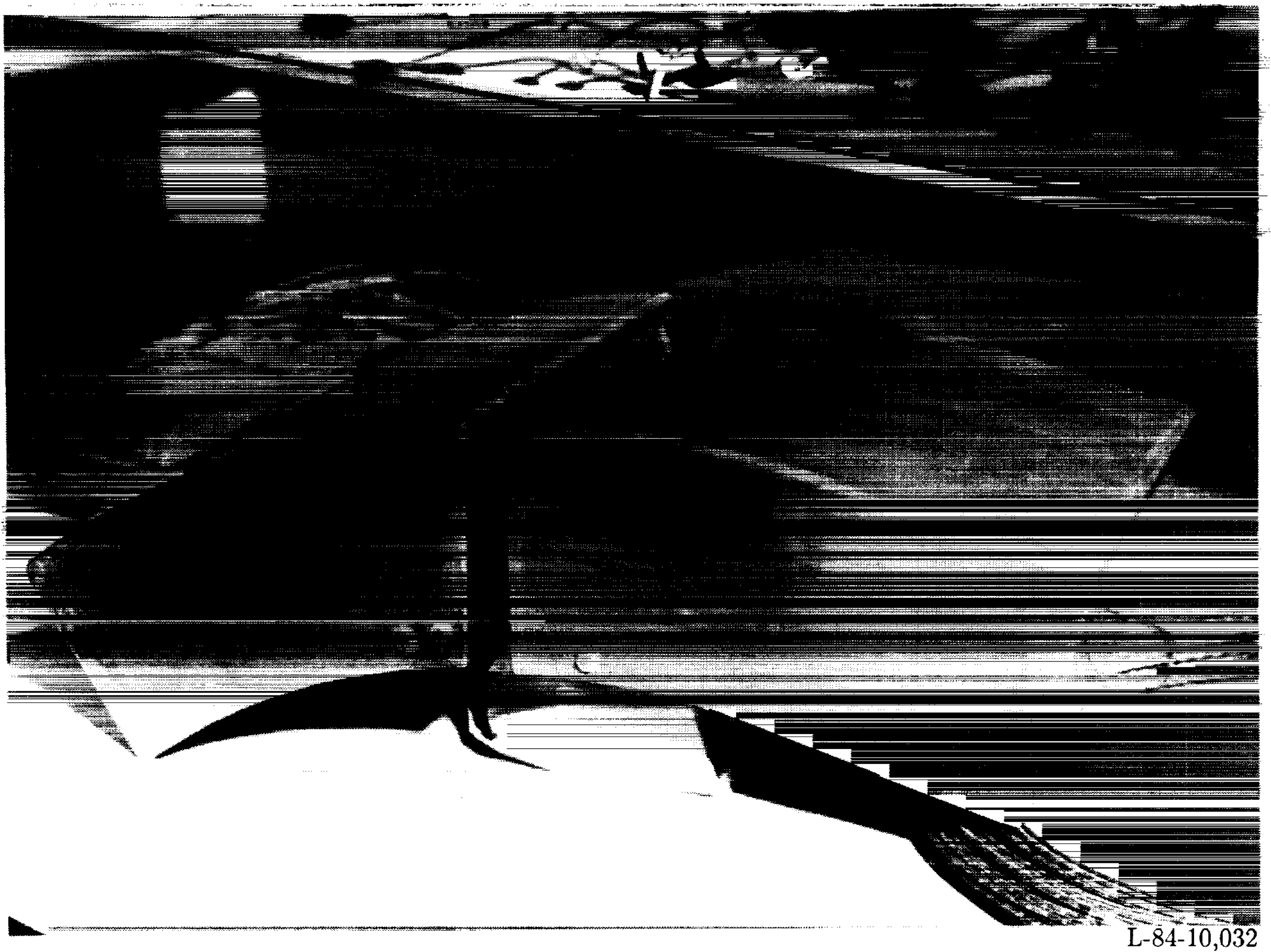
L-84-10,032

Figure 8. Large-radius-chine thin-wall tiles.

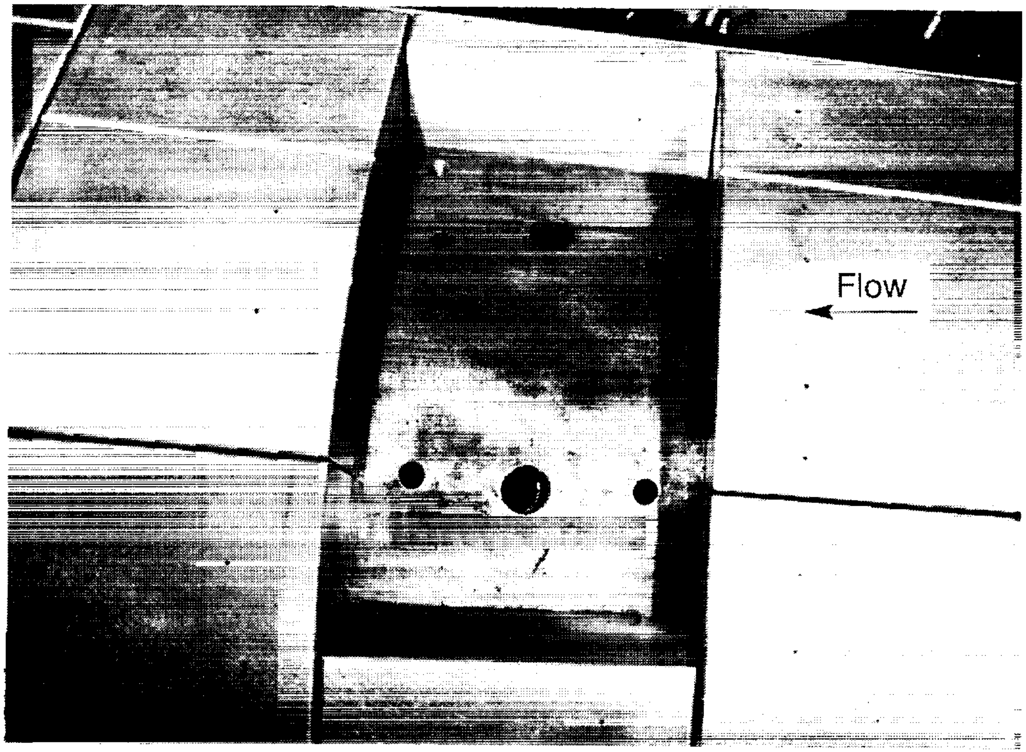

L-87-5450

(a) Tiles removed.

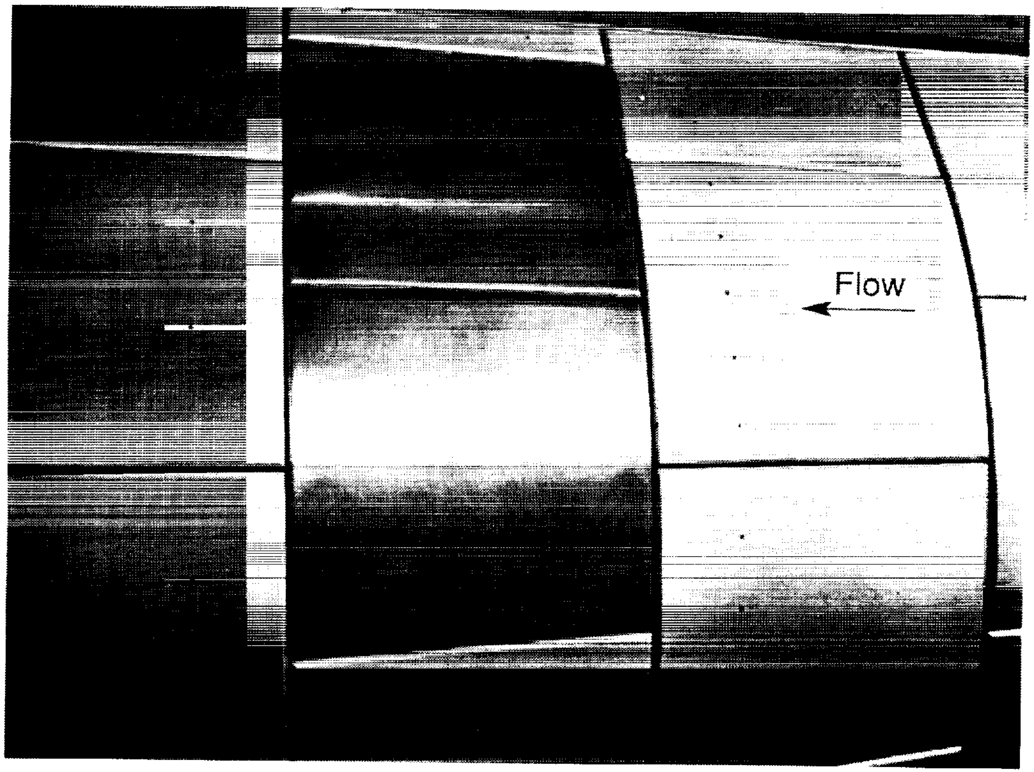

L-87-8410

(b) Tiles installed.

Figure 9. Large-radius-chine instrumented region.

ORIGINAL PAGE
BLACK AND WHITE PHOTOGRAPH

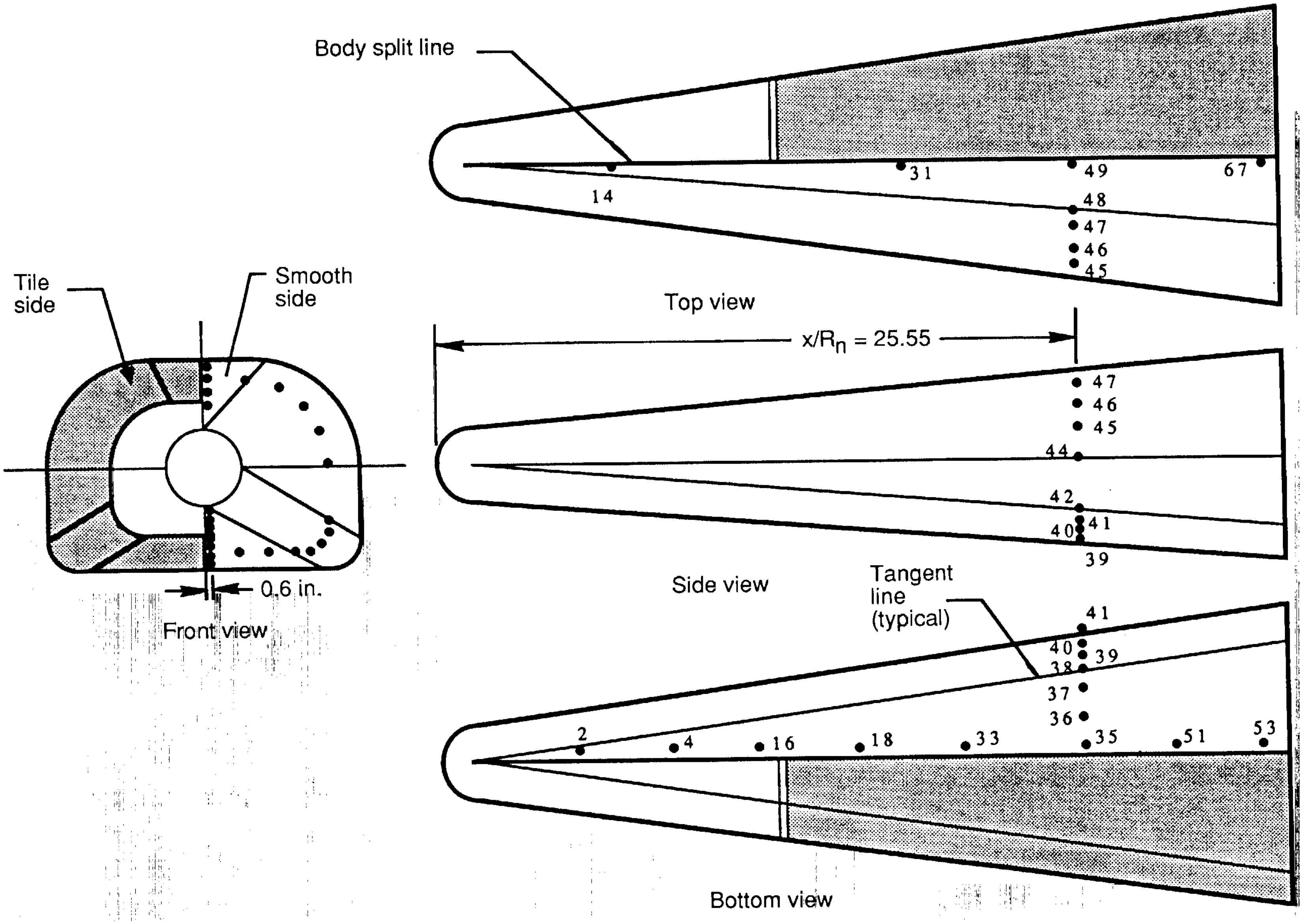

(a) Presure and Gardon sensors.

Figure 10. Location of model smooth-side instrumentation.

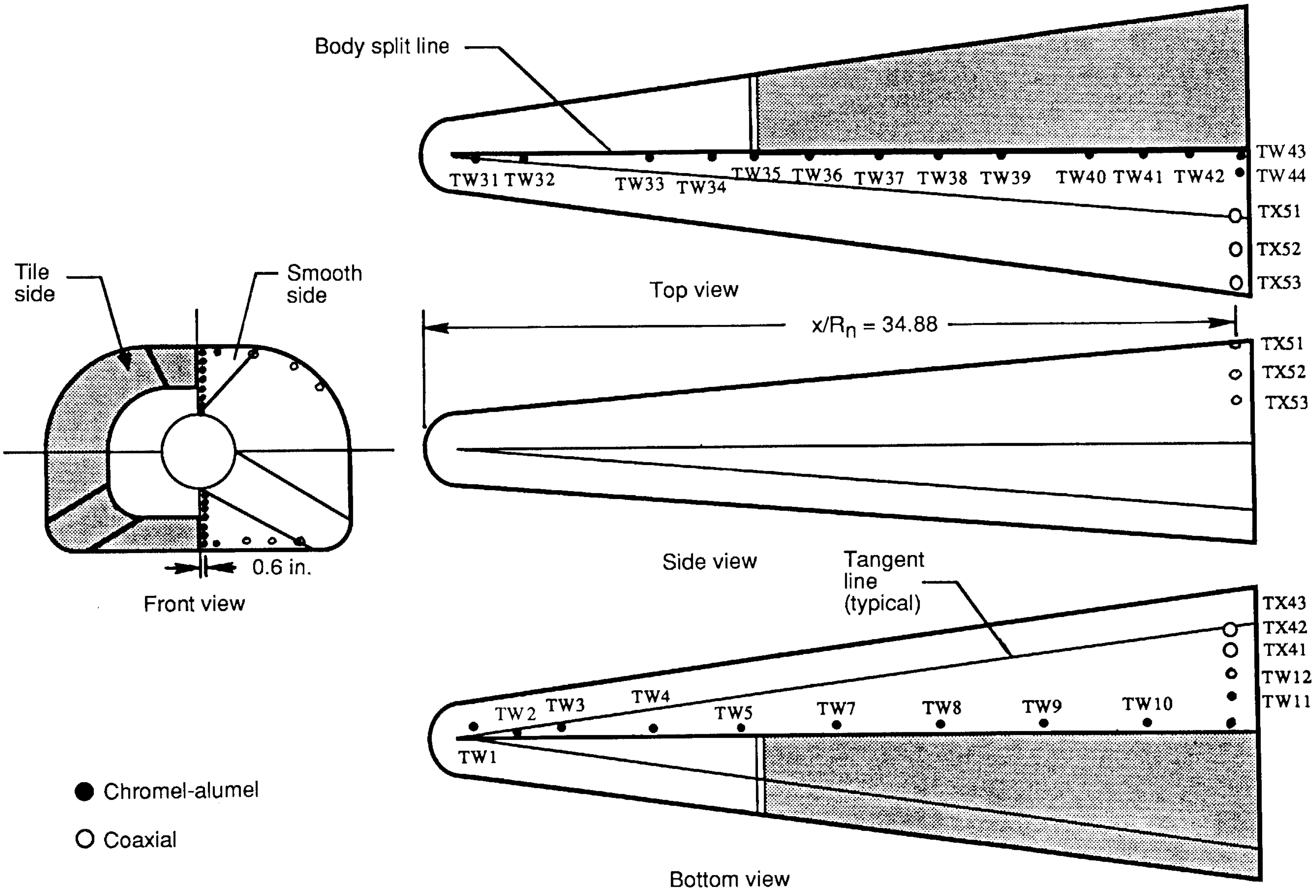

(b) Thermocouples.

Figure 10. Concluded.

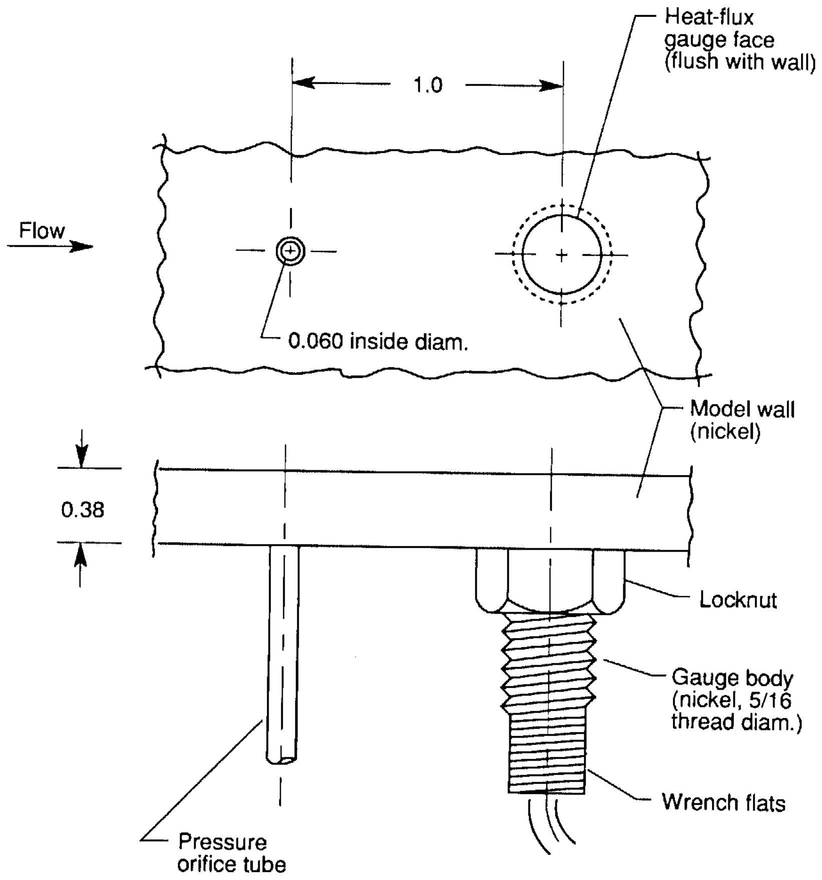

Figure 11. Typical model surface pressure and heat-flux gauge installation. All dimensions are given in inches.

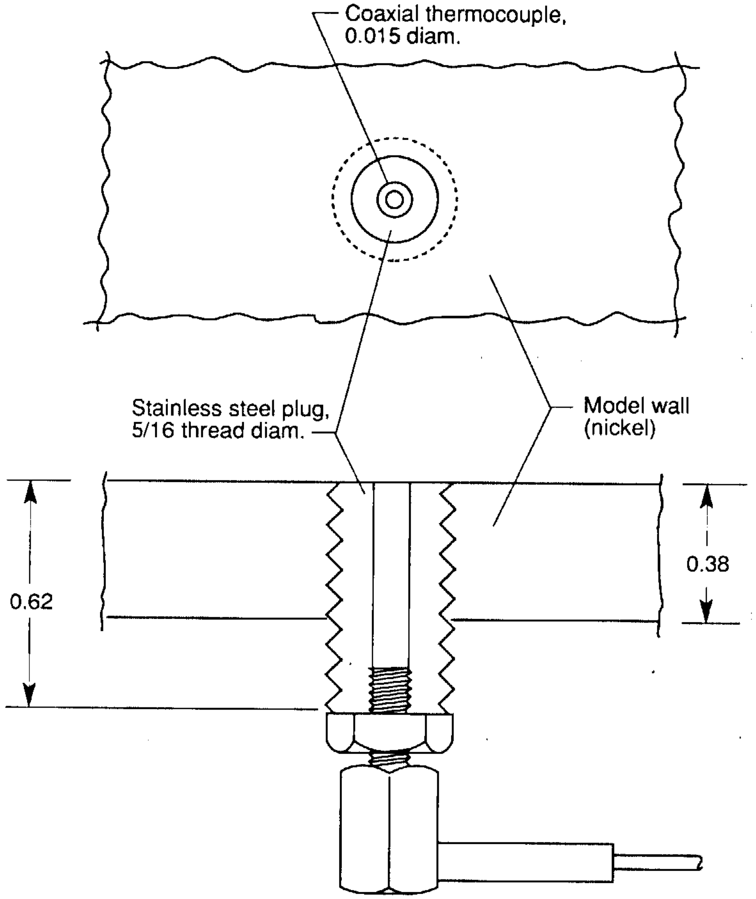

Figure 12. Coaxial thermocouple installation. All dimensions are given in inches.

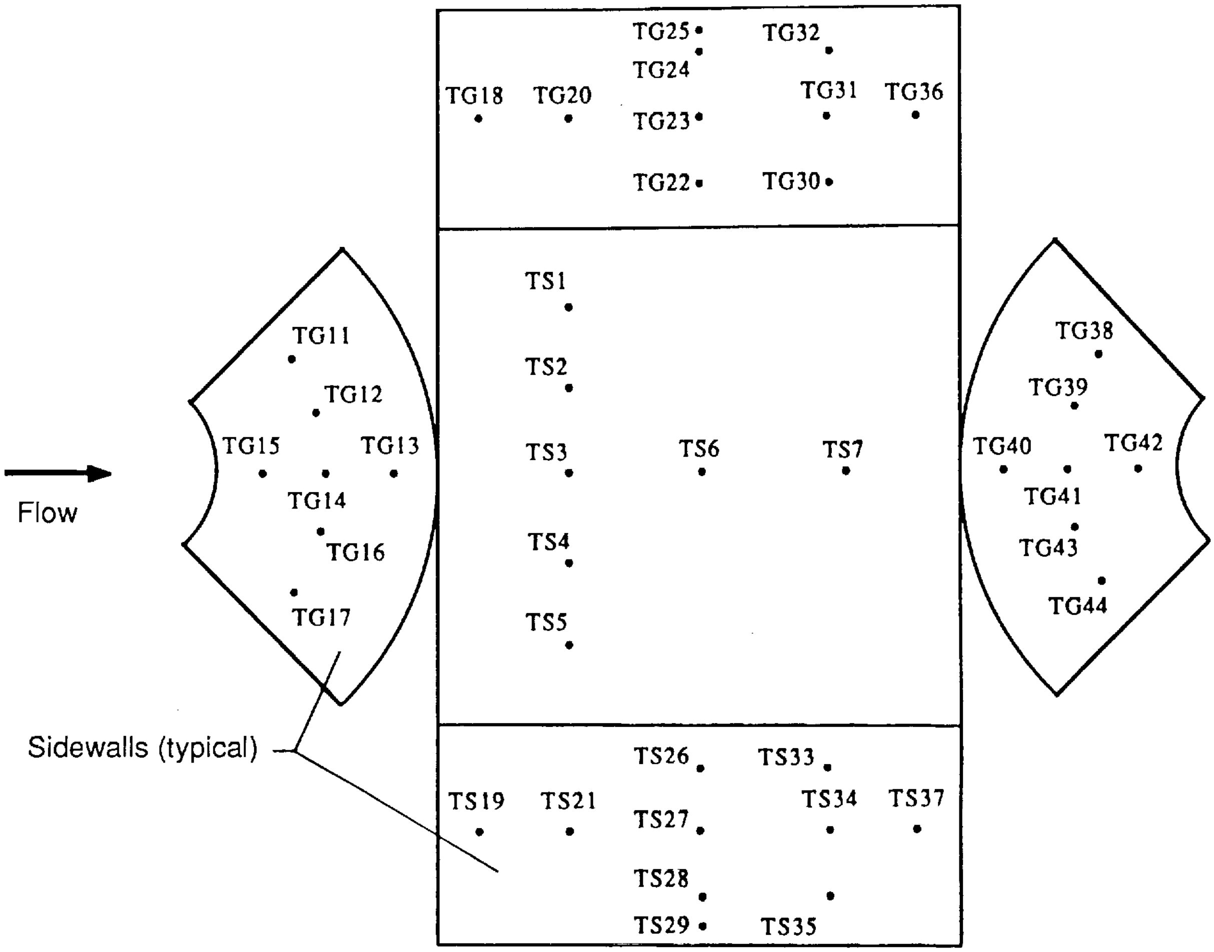

Figure 13. Location of thermocouples for small-radius-chine (configuration 1) instrumented tile.

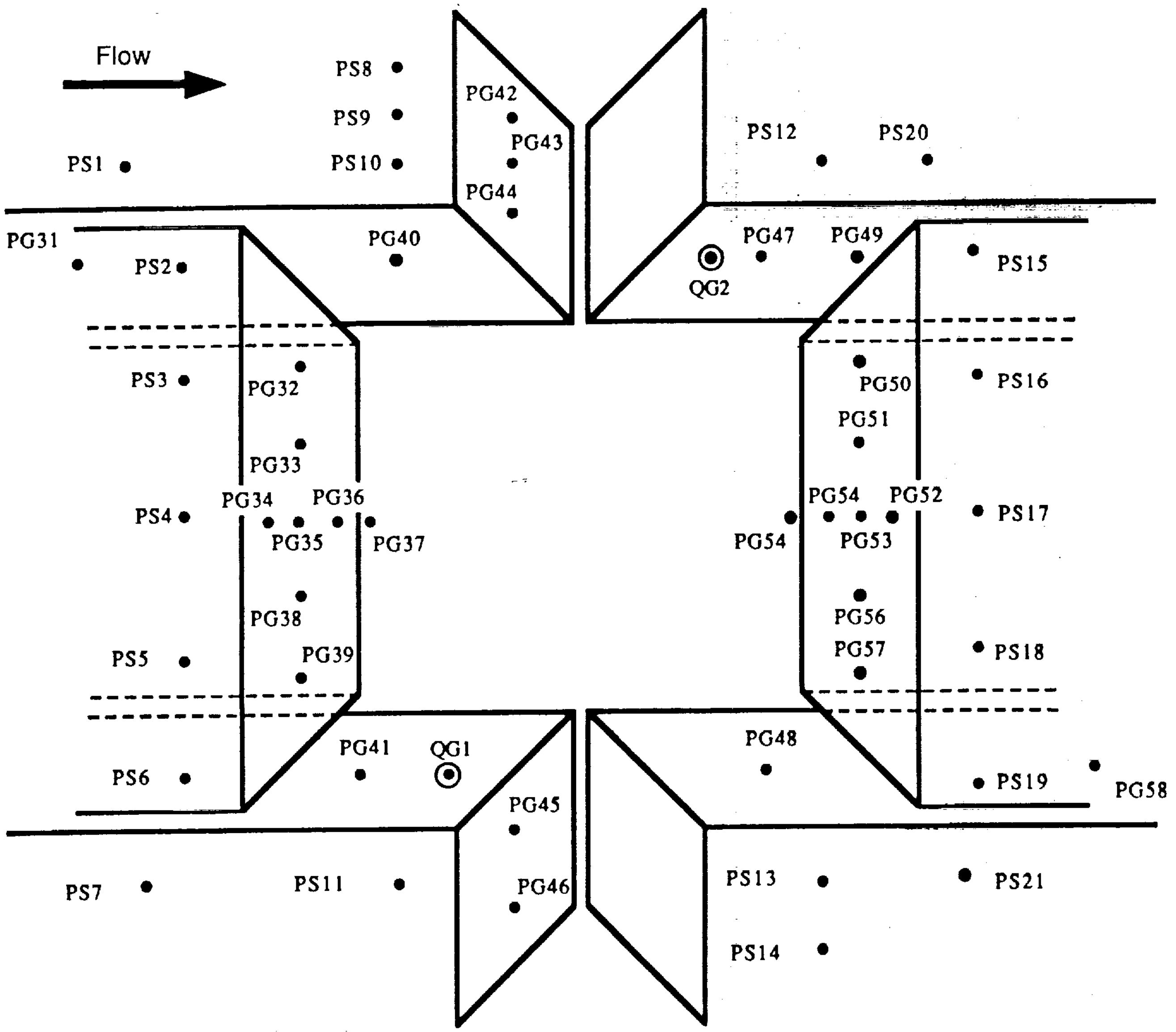

Figure 14. Location of pressure orifices and Gardon sensors surrounding small-radius-chine (configuration 1) instrumented tile.

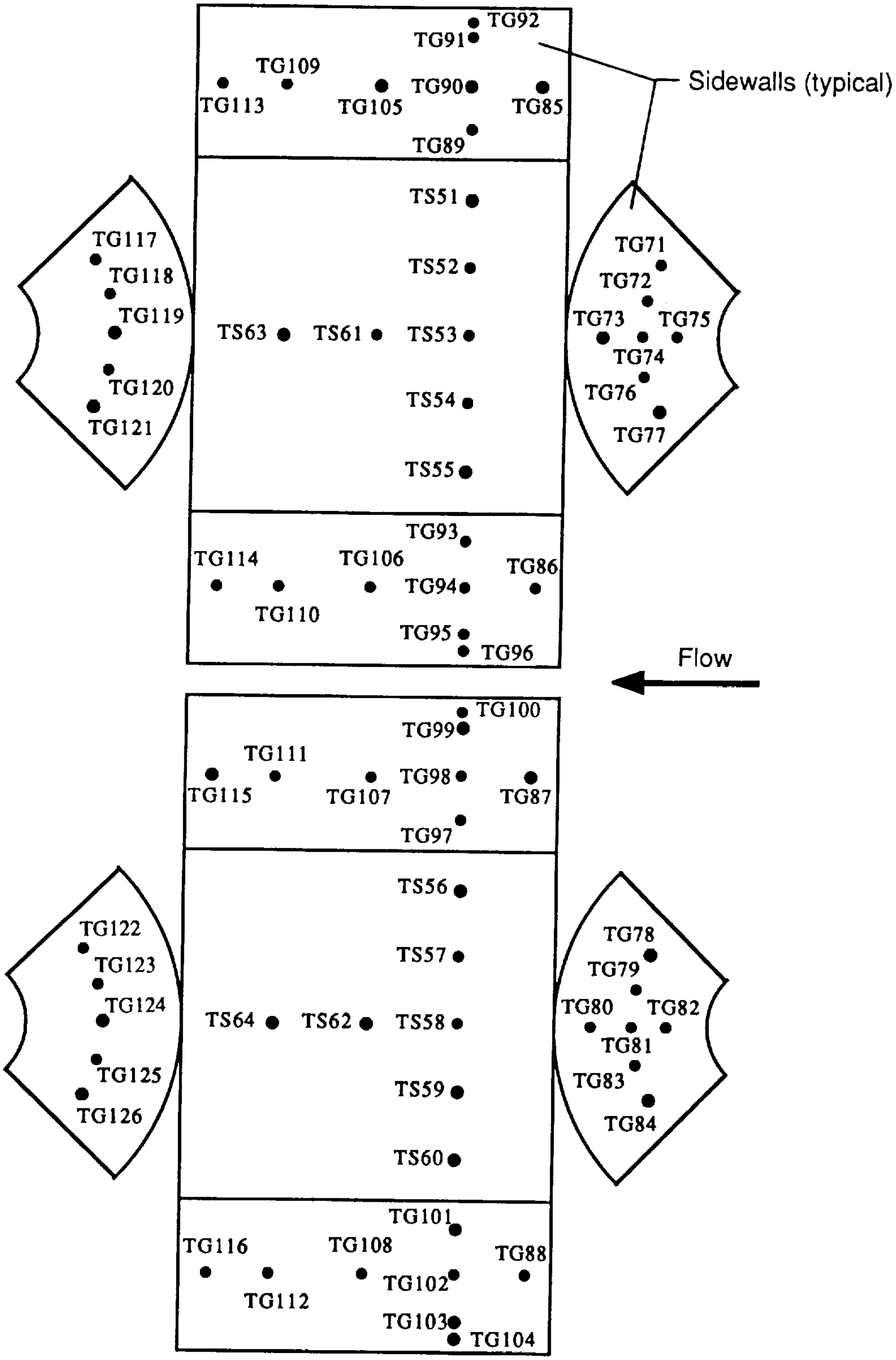

Figure 15. Location of thermocouples for large-radius-chine (configuration 2) instrumented tiles.

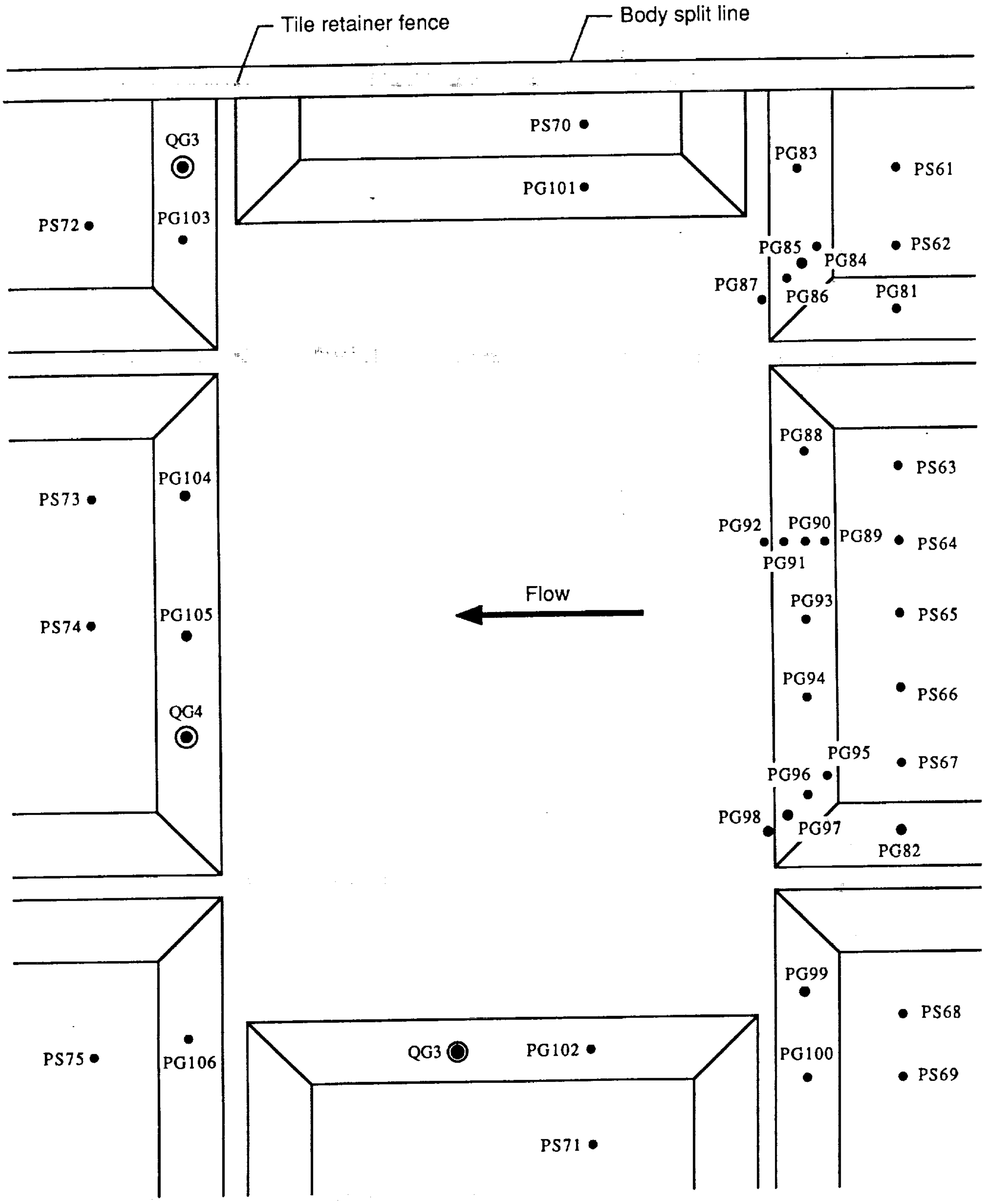

Figure 16. Location of pressure orifices and Gardon sensors surrounding large-radius-chine (configuration 2) instrumented tiles.

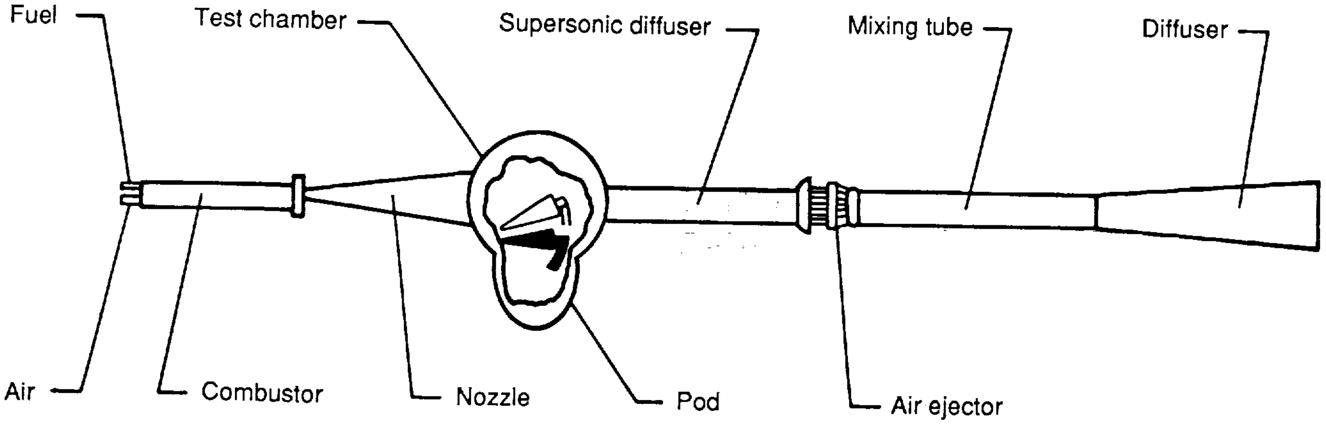

Figure 17. Schematic of the Langley 8-Foot High-Temperature Tunnel.

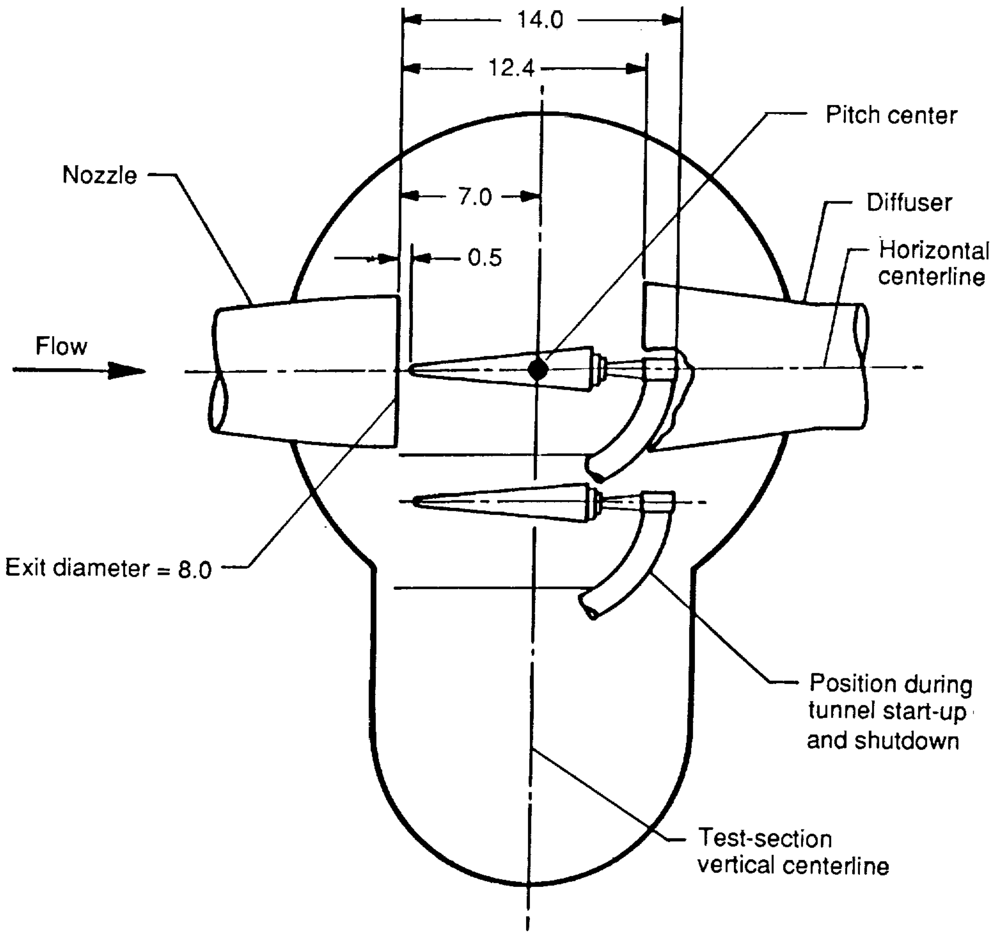

Figure 18. Cross-sectional view of test section of the Langley 8-Foot High-Temperature Tunnel with CSTA model installed. Dimensions are given in feet.

ORIGINAL PAGE
BLACK AND WHITE PHOTOGRAPH

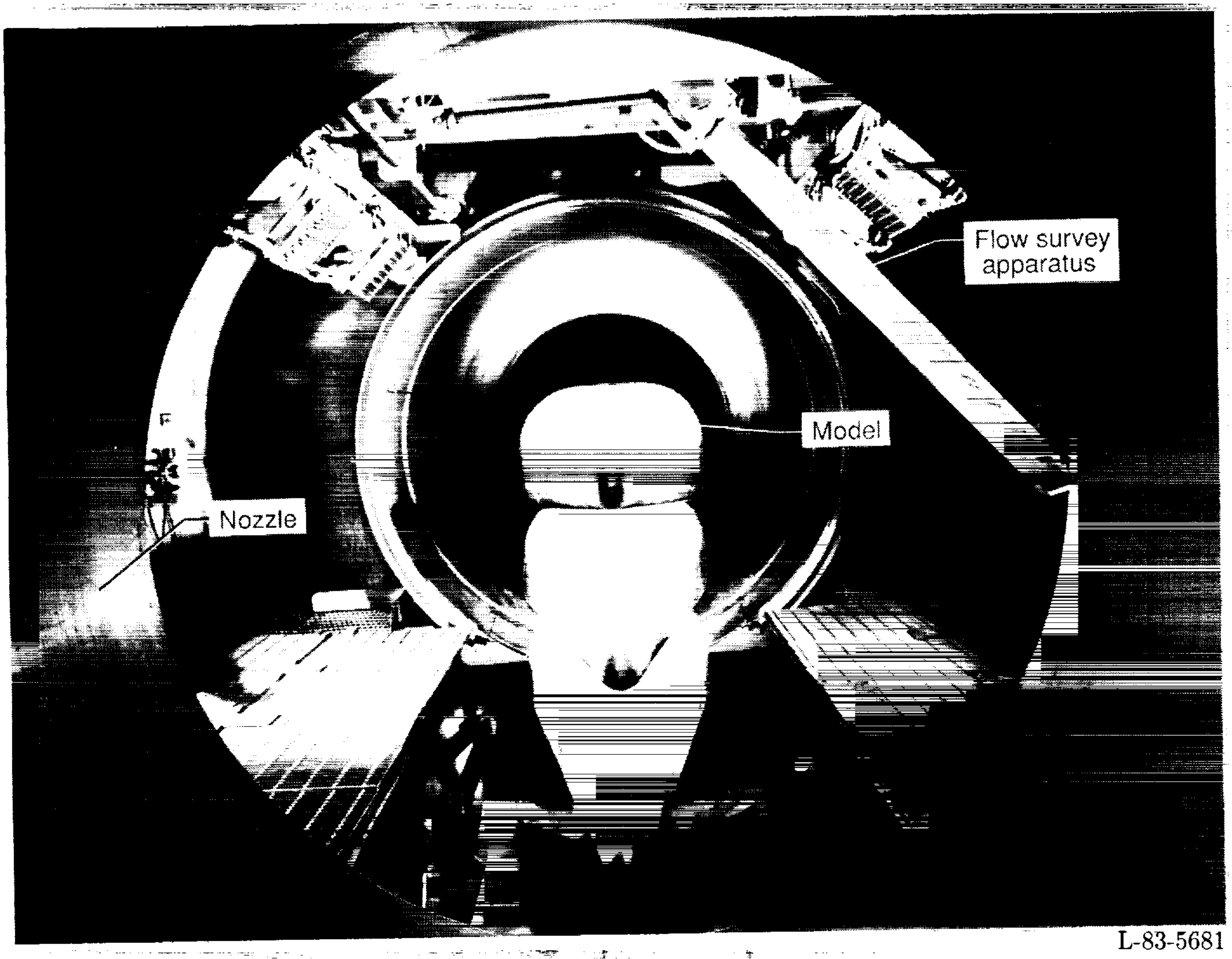

L-83-5681

Figure 19. Triple exposure of model entering test section of the Langley 8-Foot High-Temperature Tunnel with flow survey apparatus in stowed position.

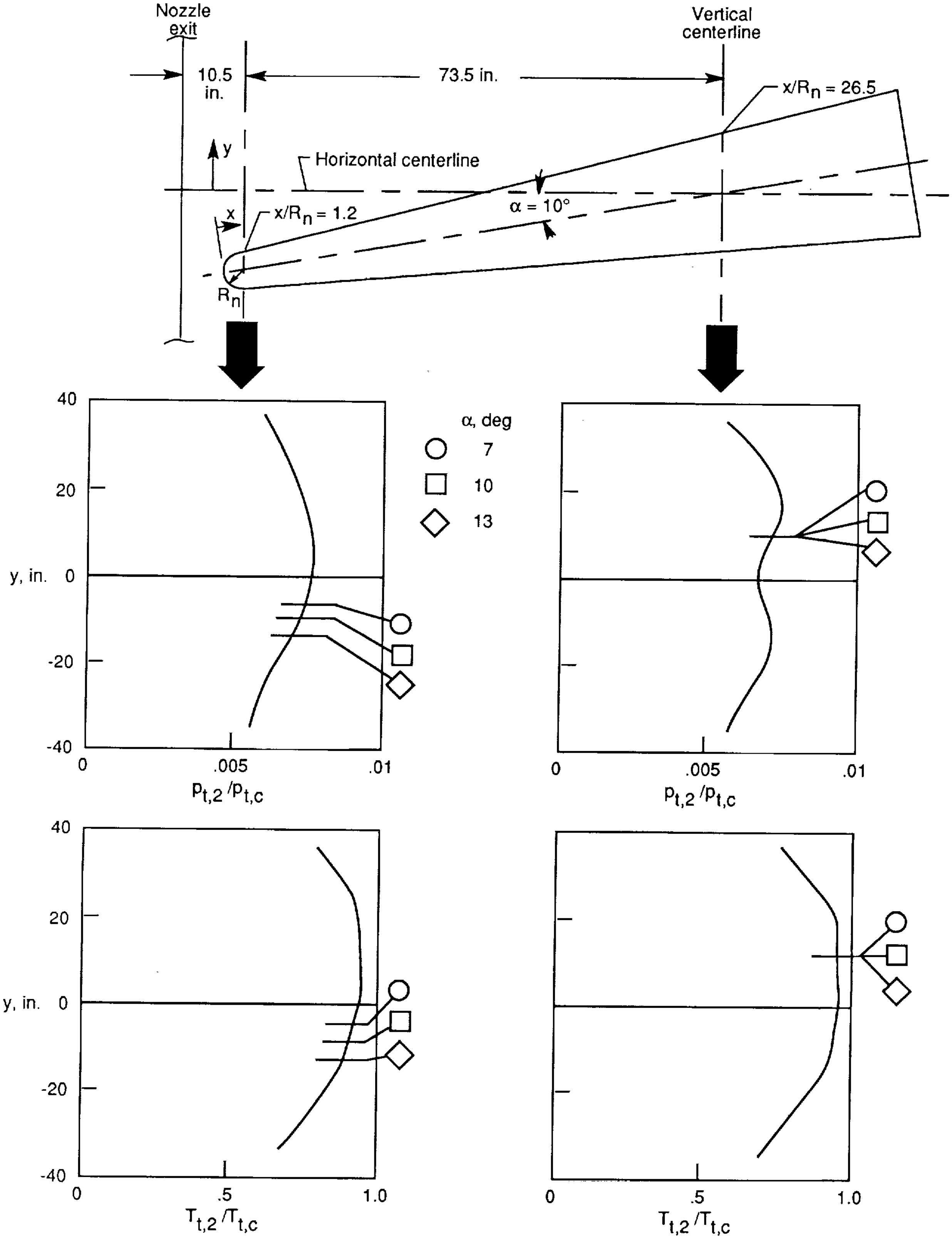

Figure 20. Stream pitot pressure and total temperature distributions for present tests in the Langley 8′ HTT.

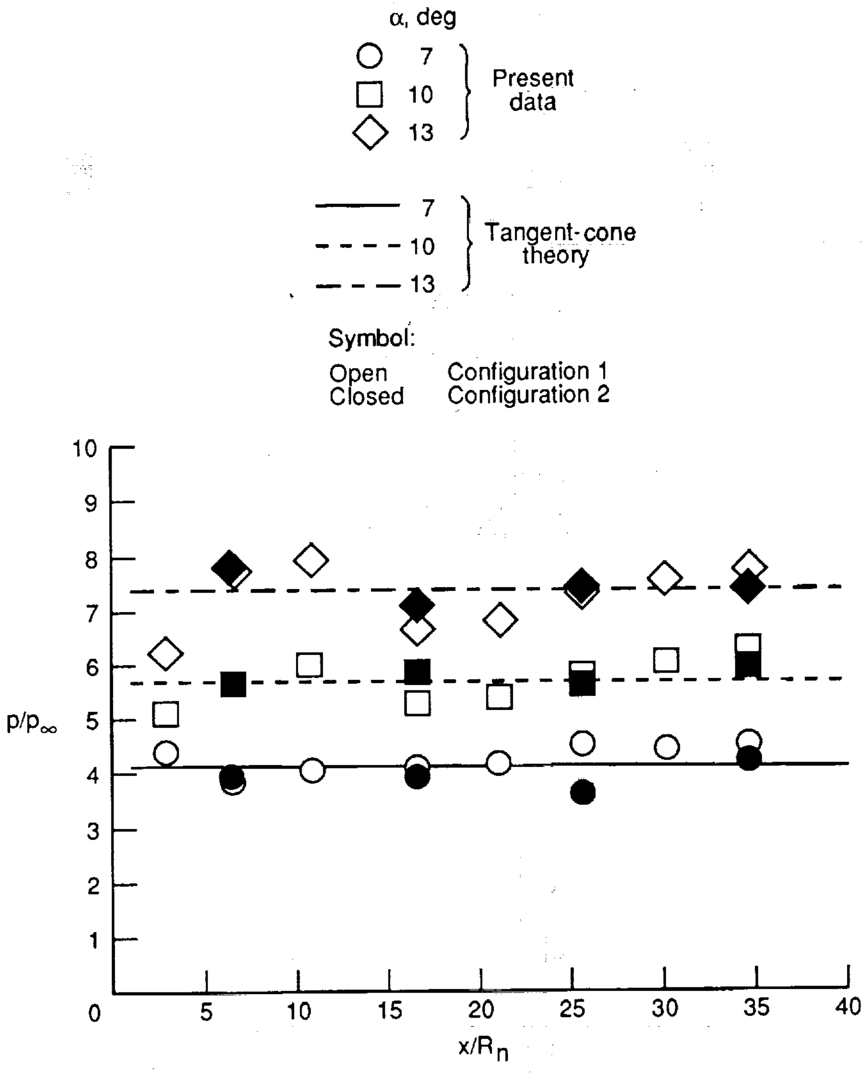

Figure 21. Windward-surface longitudinal pressure distributions.

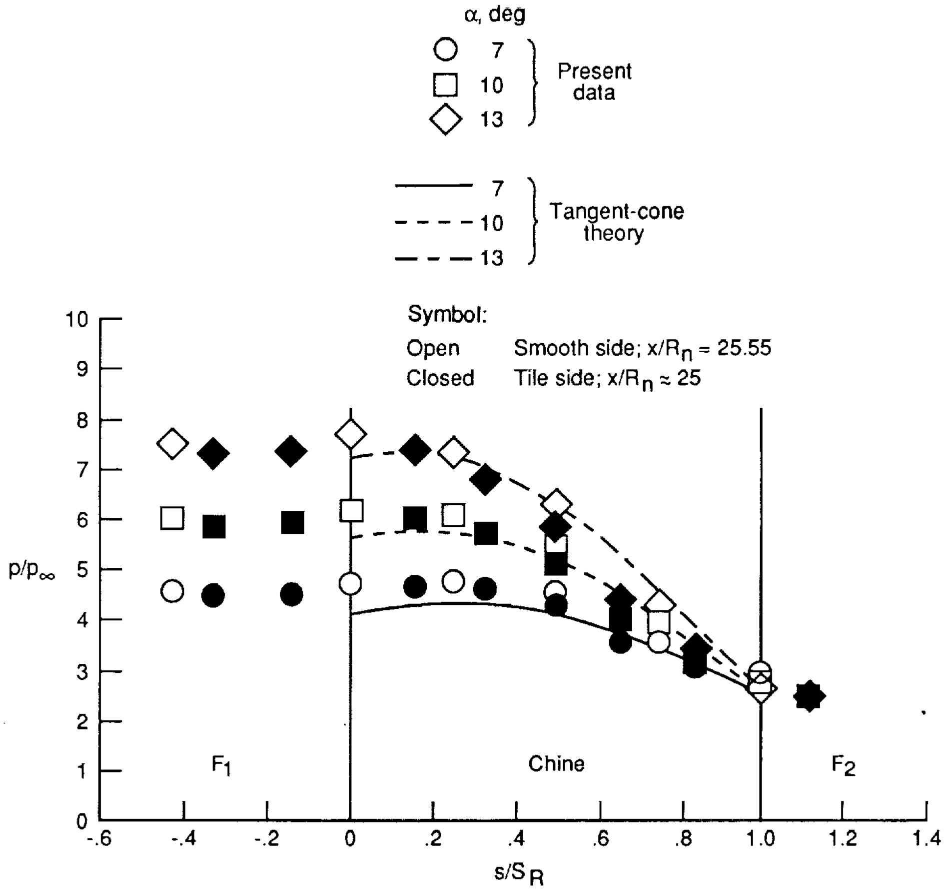

(a) Configuration 1.

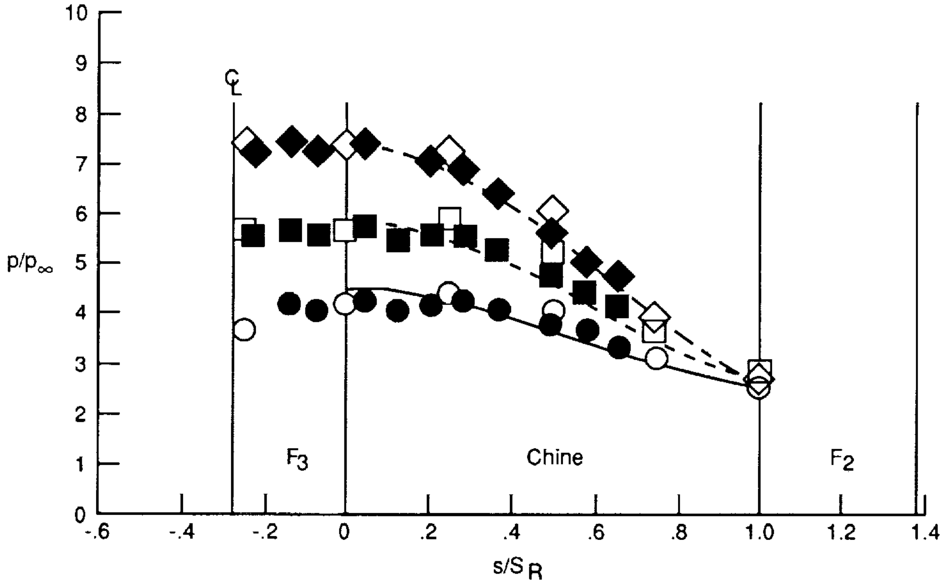

(b) Configuration 2.

Figure 22. Surface circumferential pressure distributions at $x/R_n = 25.55$.

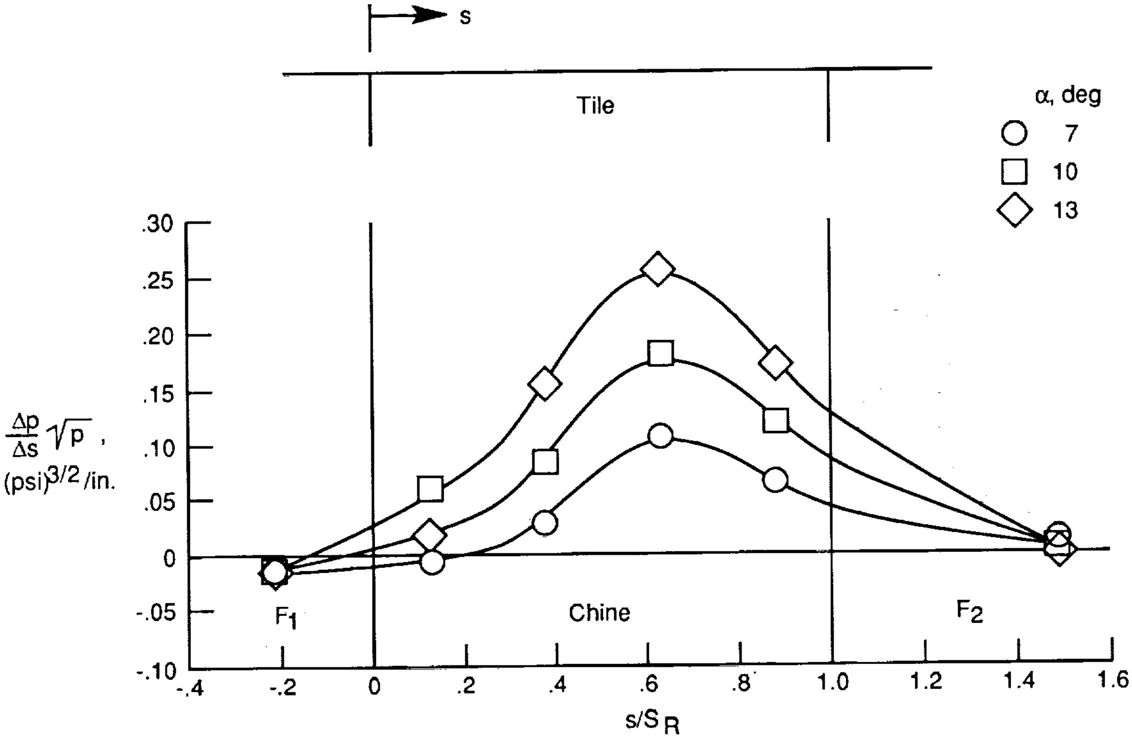

(a) Configuration 1.

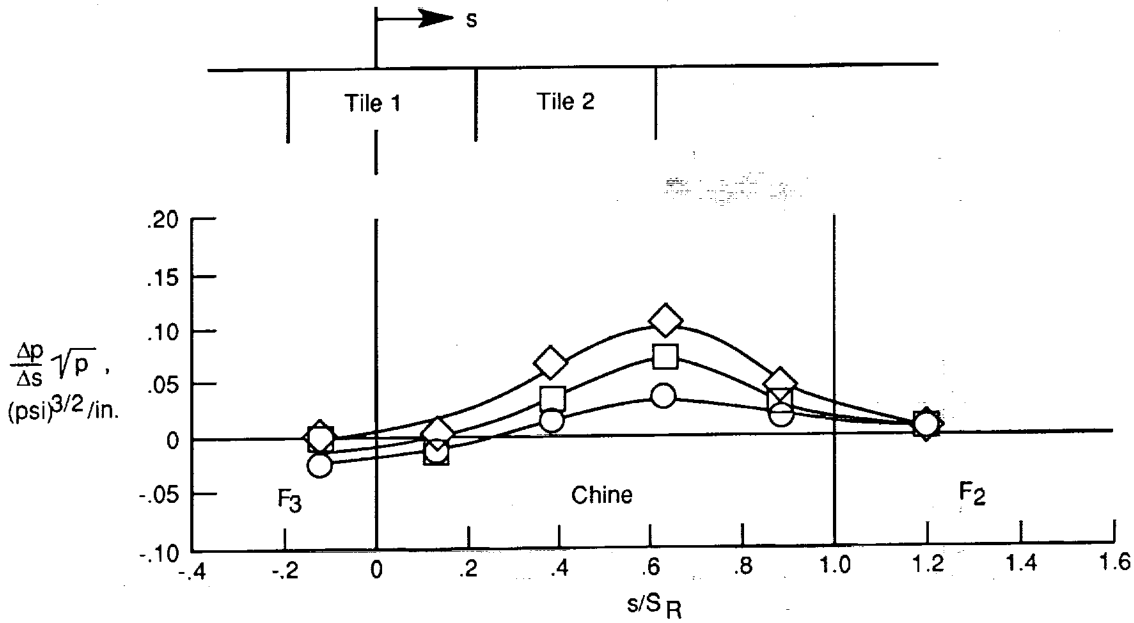

(b) Configuration 2.

Figure 23. Variation of circumferential pressure differential parameter at $x/R_n = 25.55$ on smooth side.

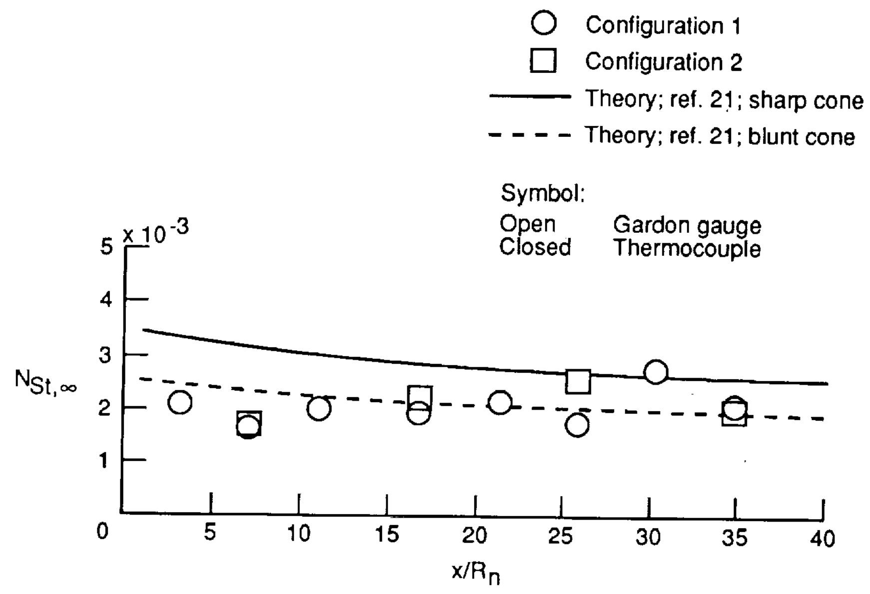

(a) $\alpha = 7°$.

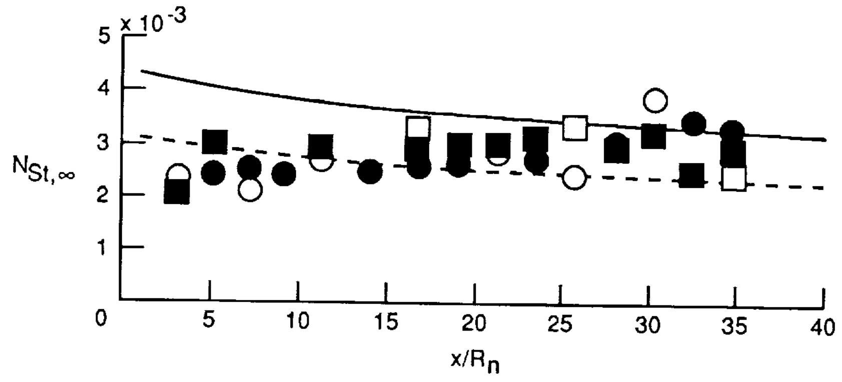

(b) $\alpha = 10°$.

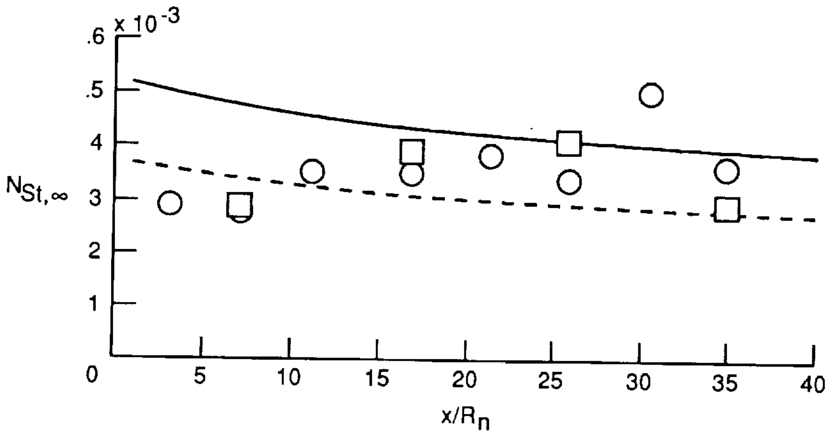

(c) $\alpha = 13°$.

Figure 24. Windward-surface longitudinal heating distributions on smooth side.

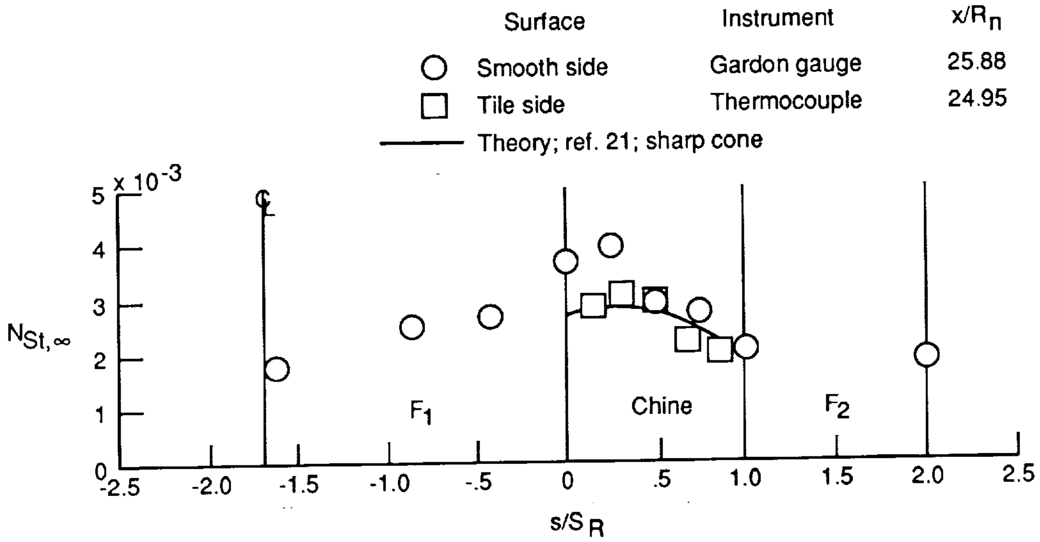

(a) $\alpha = 7^\circ$.

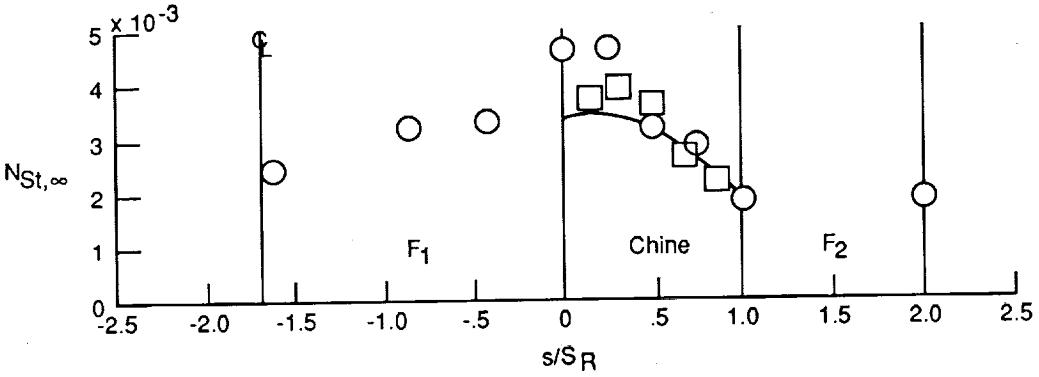

(b) $\alpha = 10^\circ$.

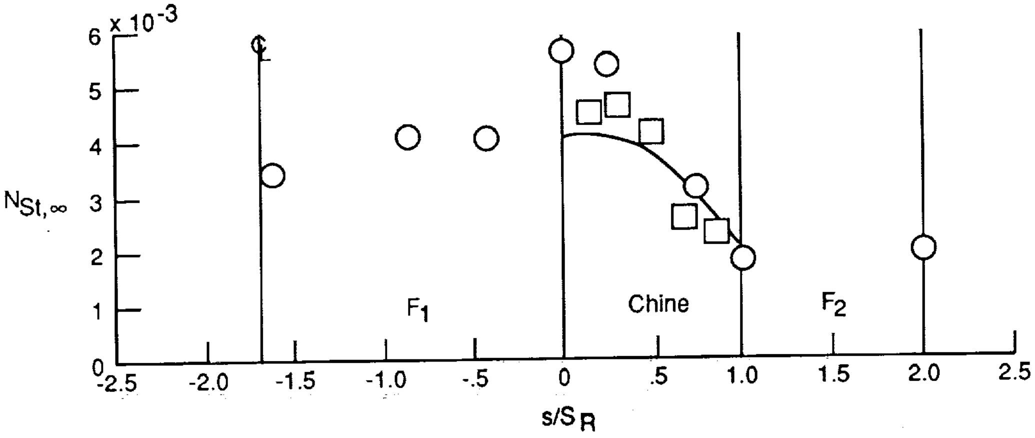

(c) $\alpha = 13^\circ$.

Figure 25. Surface circumferential heating distributions for configuration 1 at $x/R_n = 25.88$.

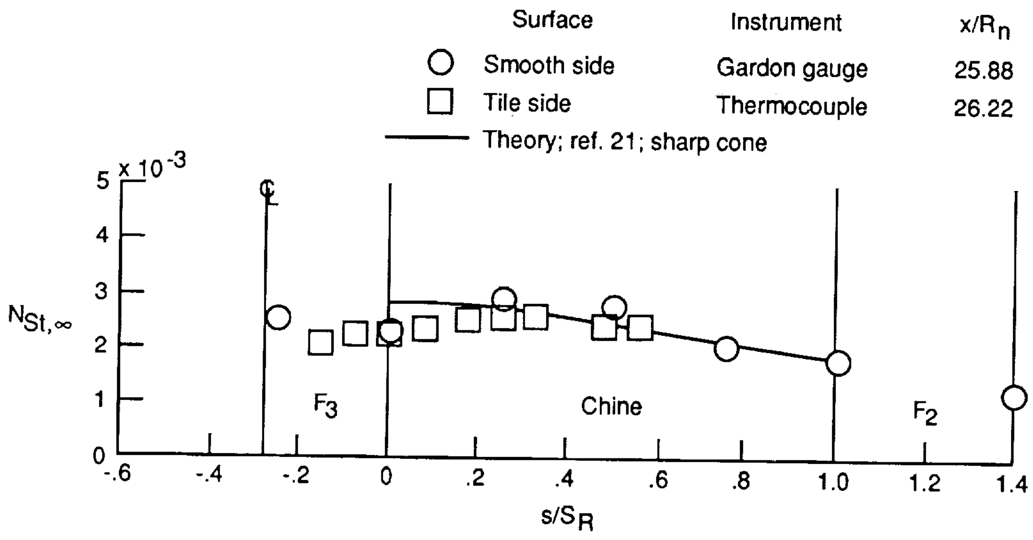

(a) $\alpha = 7°$.

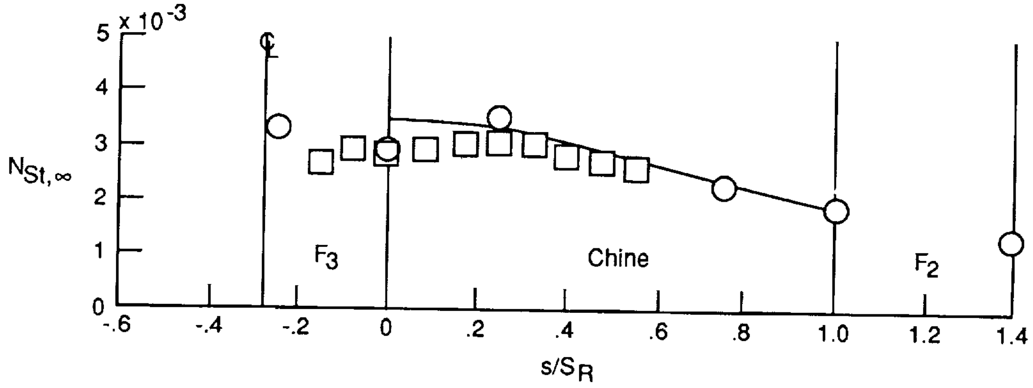

(b) $\alpha = 10°$.

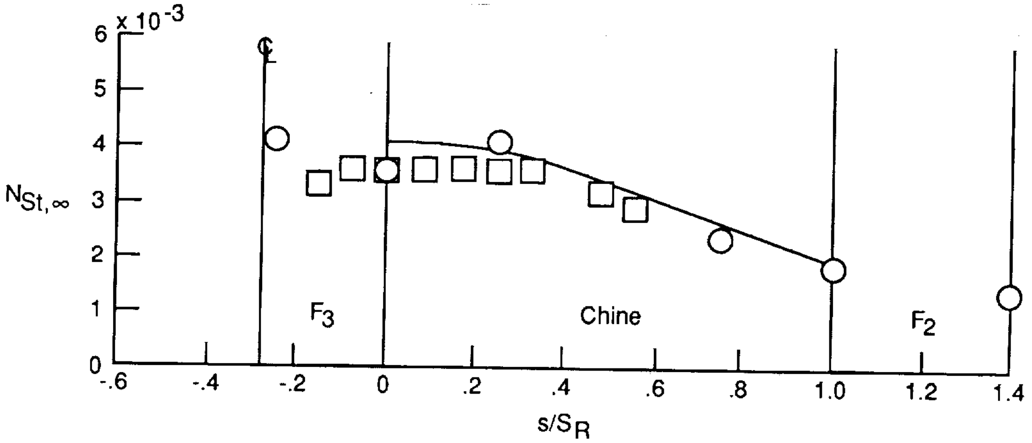

(c) $\alpha = 13°$.

Figure 26. Surface circumferential heating distributions for configuration 2 at $x/R_n = 25.88$.

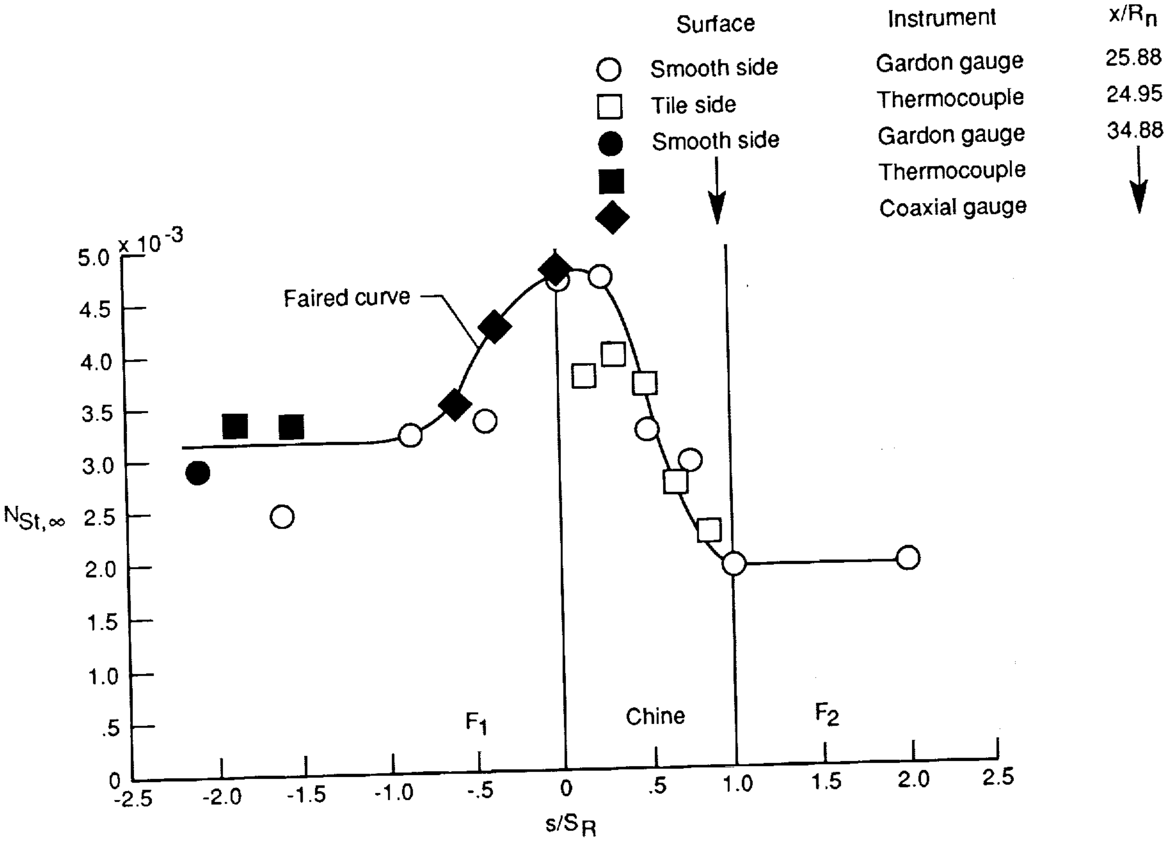

(a) Configuration 1.

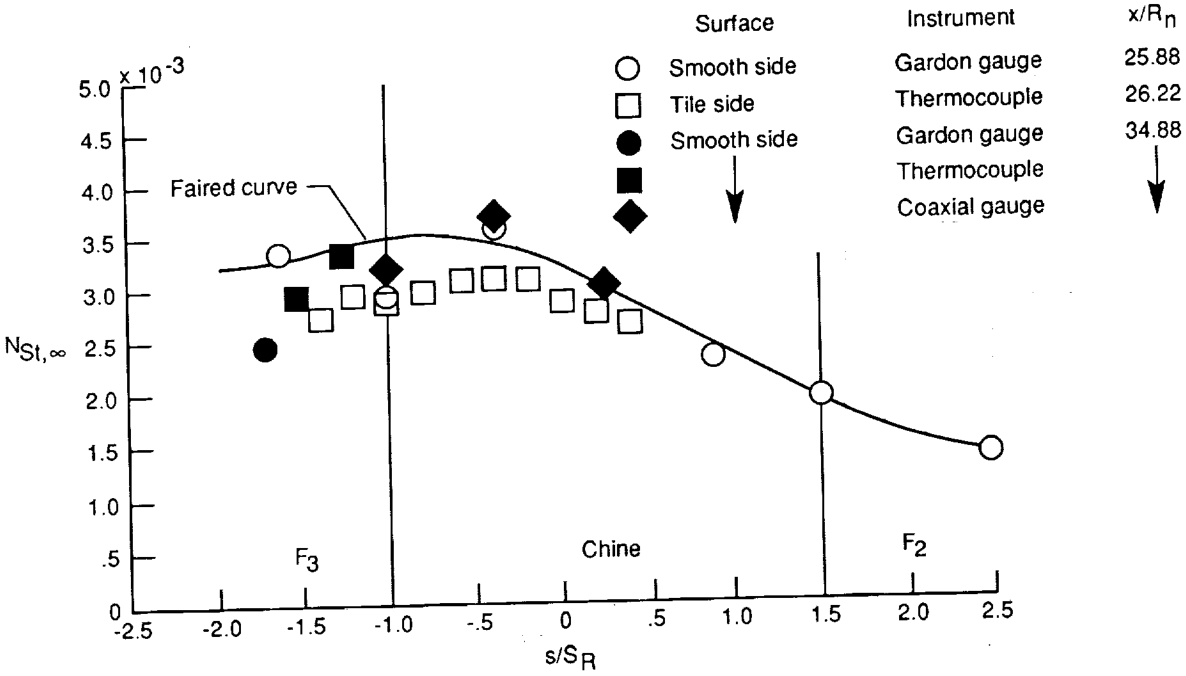

(b) Configuration 2.

Figure 27. Surface circumferential heating distributions for $\alpha = 10°$ at $x/R_n = 25.88$ and 34.88.

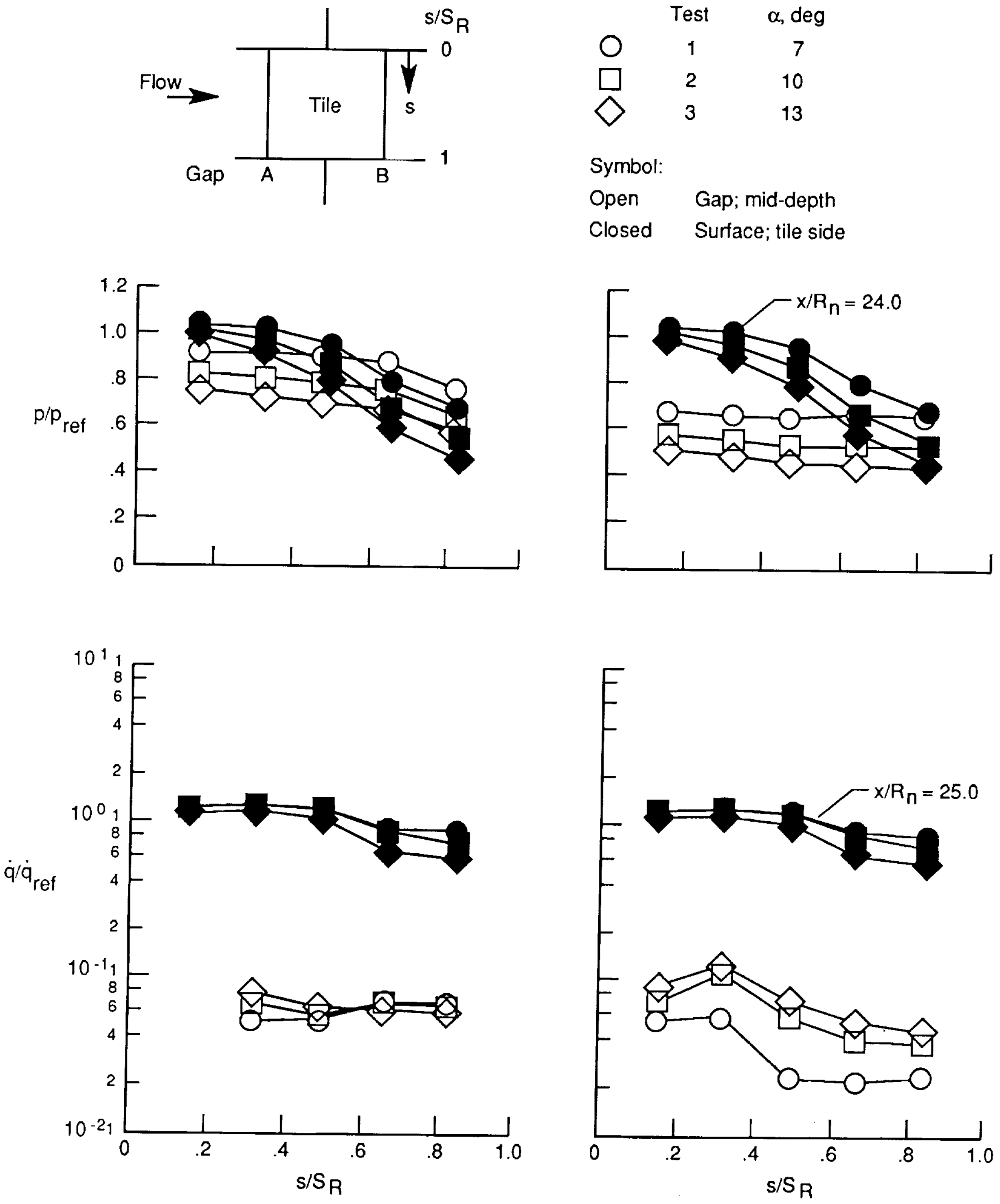

(a) Gap A. $x/R_n = 24.4$; $w = 0.075$ in.

(b) Gap B. $x/R_n = 26.4$; $w = 0.103$ in.

Figure 28. Variation of circumferential gap pressure and heating distributions with angle of attack for configuration 1.

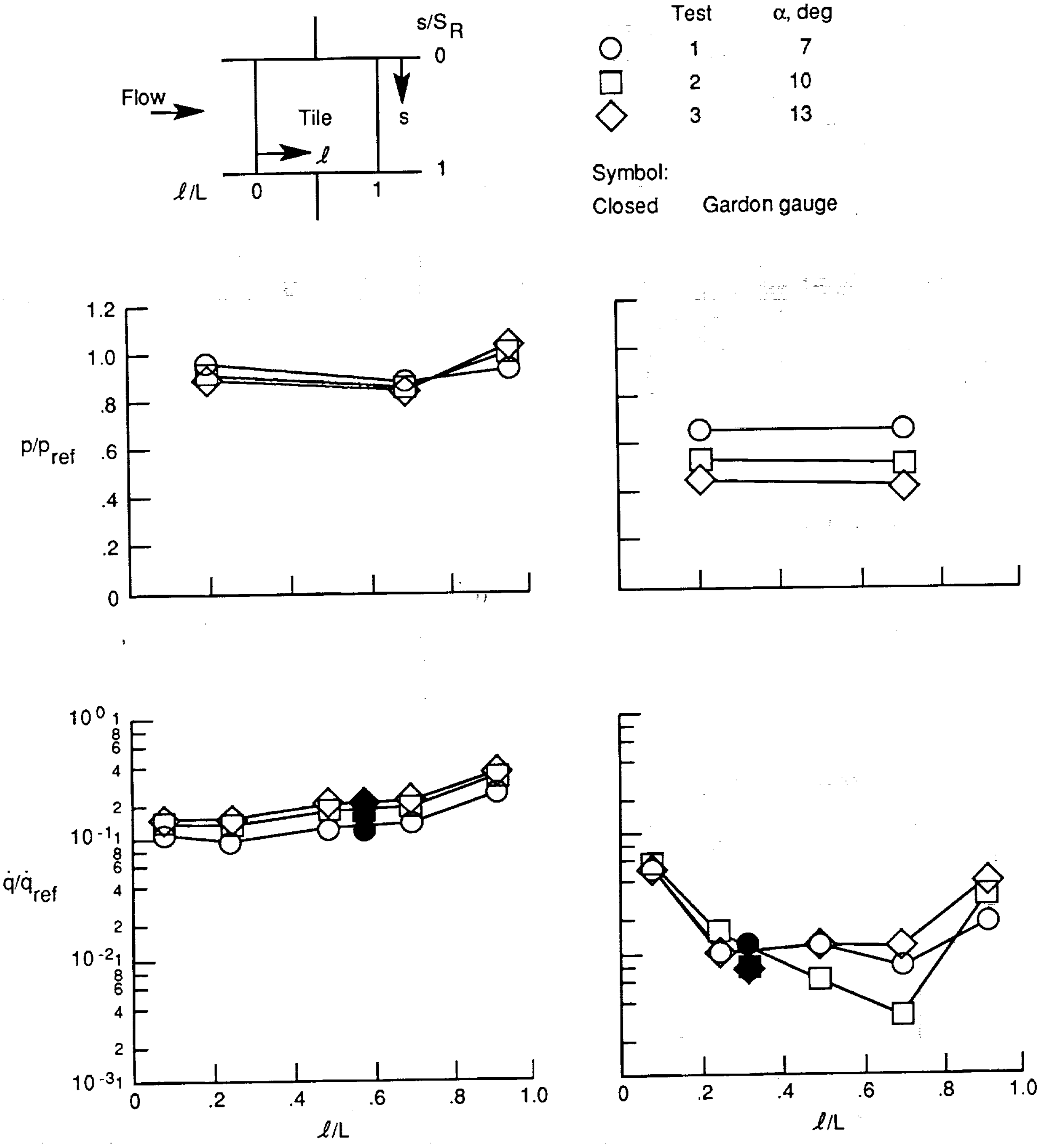

(a) $s/S_R = 0$.

(b) $s/S_R = 1$.

Figure 29. Variation of longitudinal gap pressure and heating distributions with angle of attack for configuration 1.

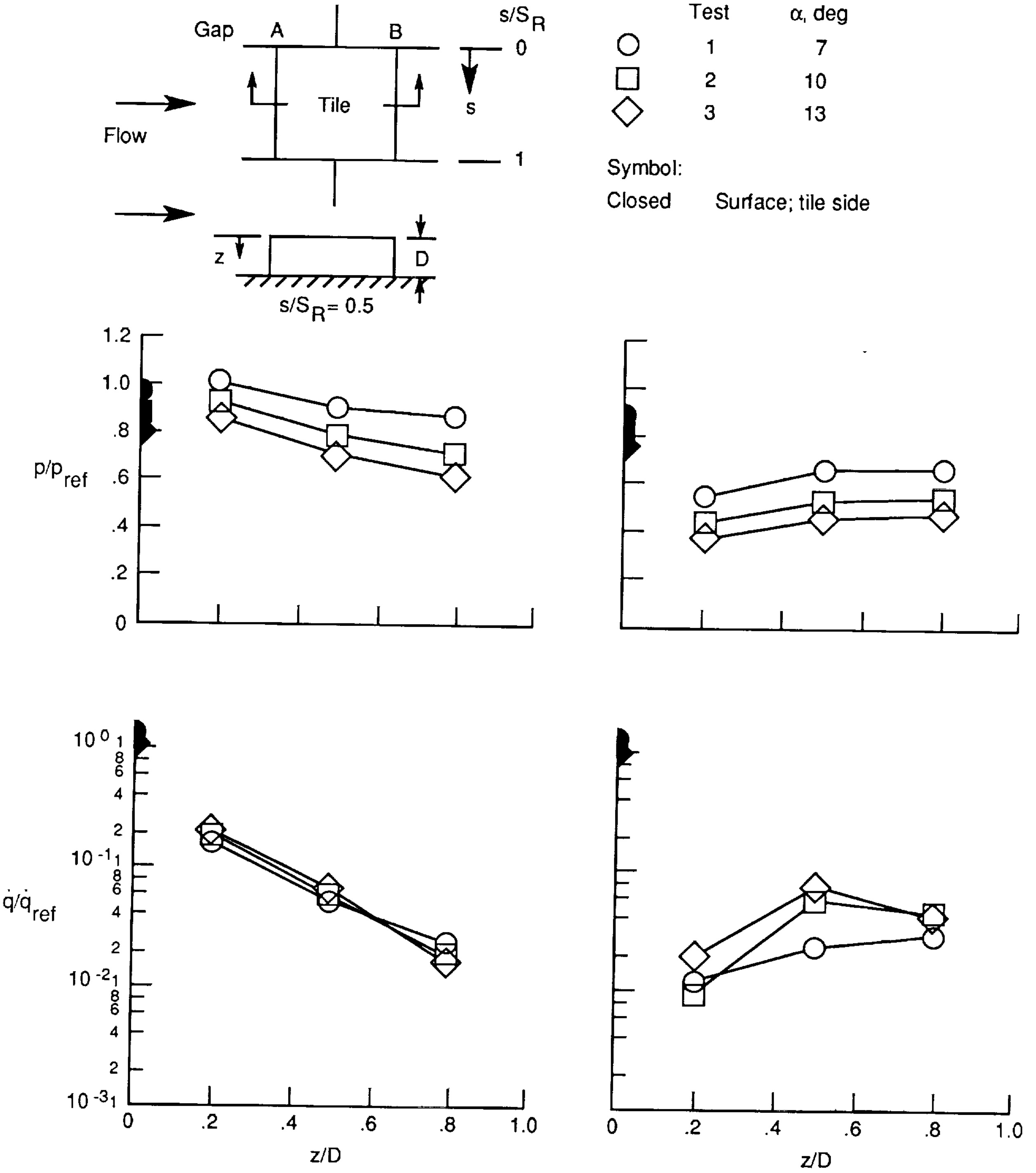

(a) Gap A. $x/R_n = 24.4$; $s/S_R = 0.5$.

(b) Gap B. $x/R_n = 26.4$; $s/S_R = 0.5$.

Figure 30. Variation of gap pressure and heating distribution into depth of circumferential gaps for configuration 1.

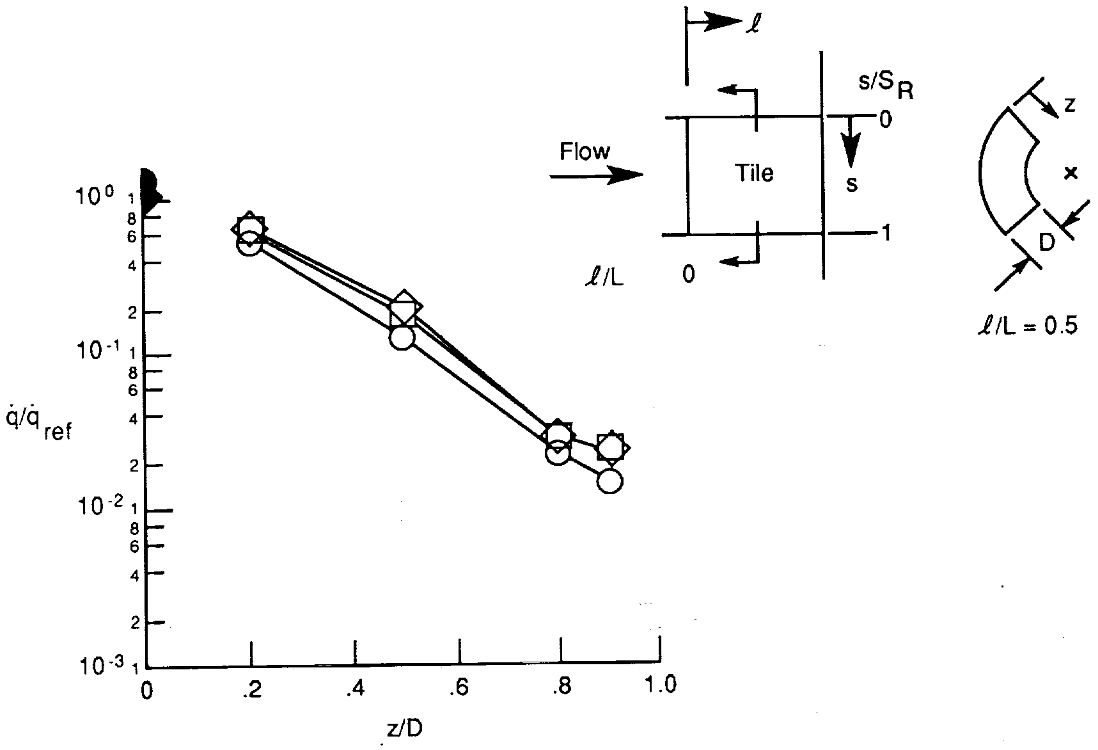

(a) $s/S_R = 0$.

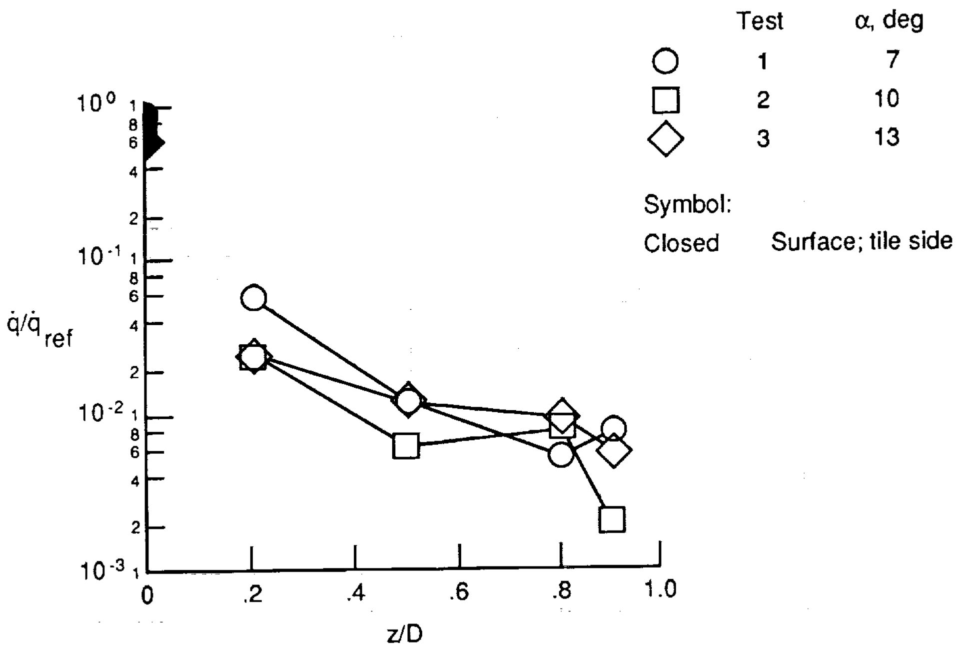

(b) $s/S_R = 1$.

Figure 31. Variation of gap heating distributions into depth of longitudinal gaps for configuration 1.

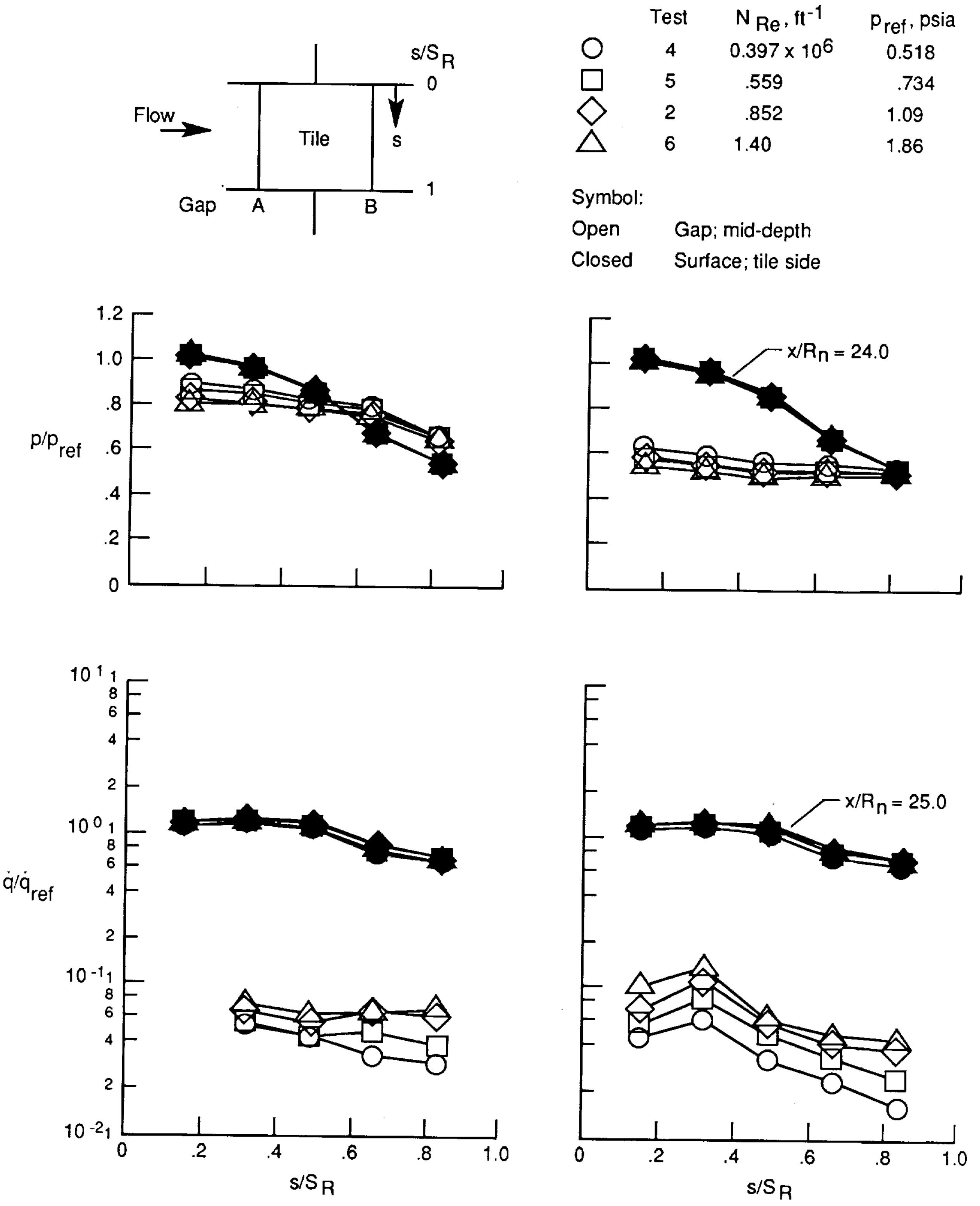

(a) Gap A. $x/R_n = 24.4$; $w = 0.075$ in.

(b) Gap B. $x/R_n = 26.4$; $w = 0.103$ in.

Figure 32. Variation of circumferential gap pressure and heating distributions with angle of attack for configuration 2 .

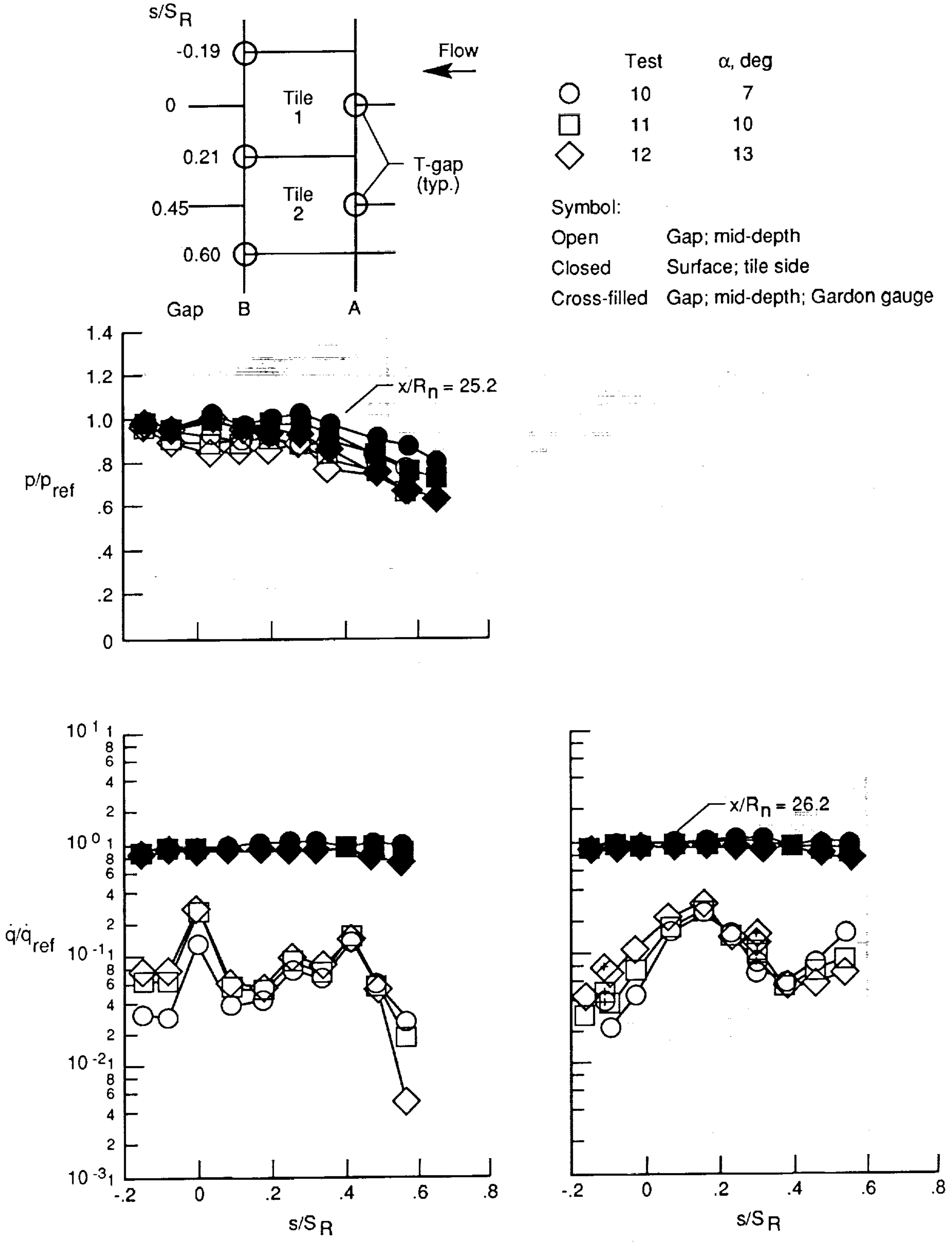

(a) Gap A. $x/R_n = 25.7$.

(b) Gap B. $x/R_n = 27.7$.

Figure 33. Variation of circumferential gap pressure and heating distributions with angle of attack for configuration 2 .

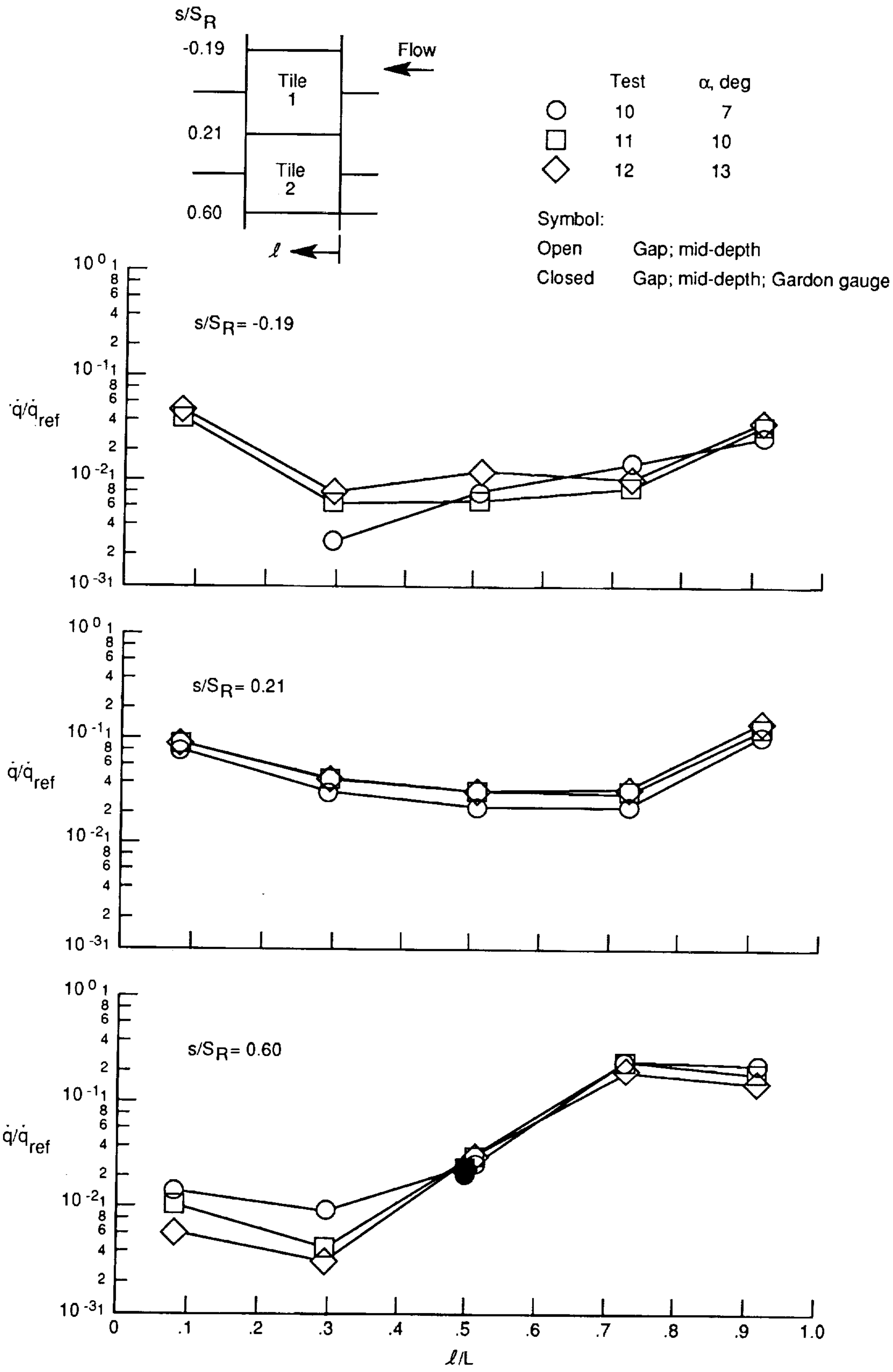

Figure 34. Variation of longitudinal gap heating distributions with angle of attack for configuration 2.

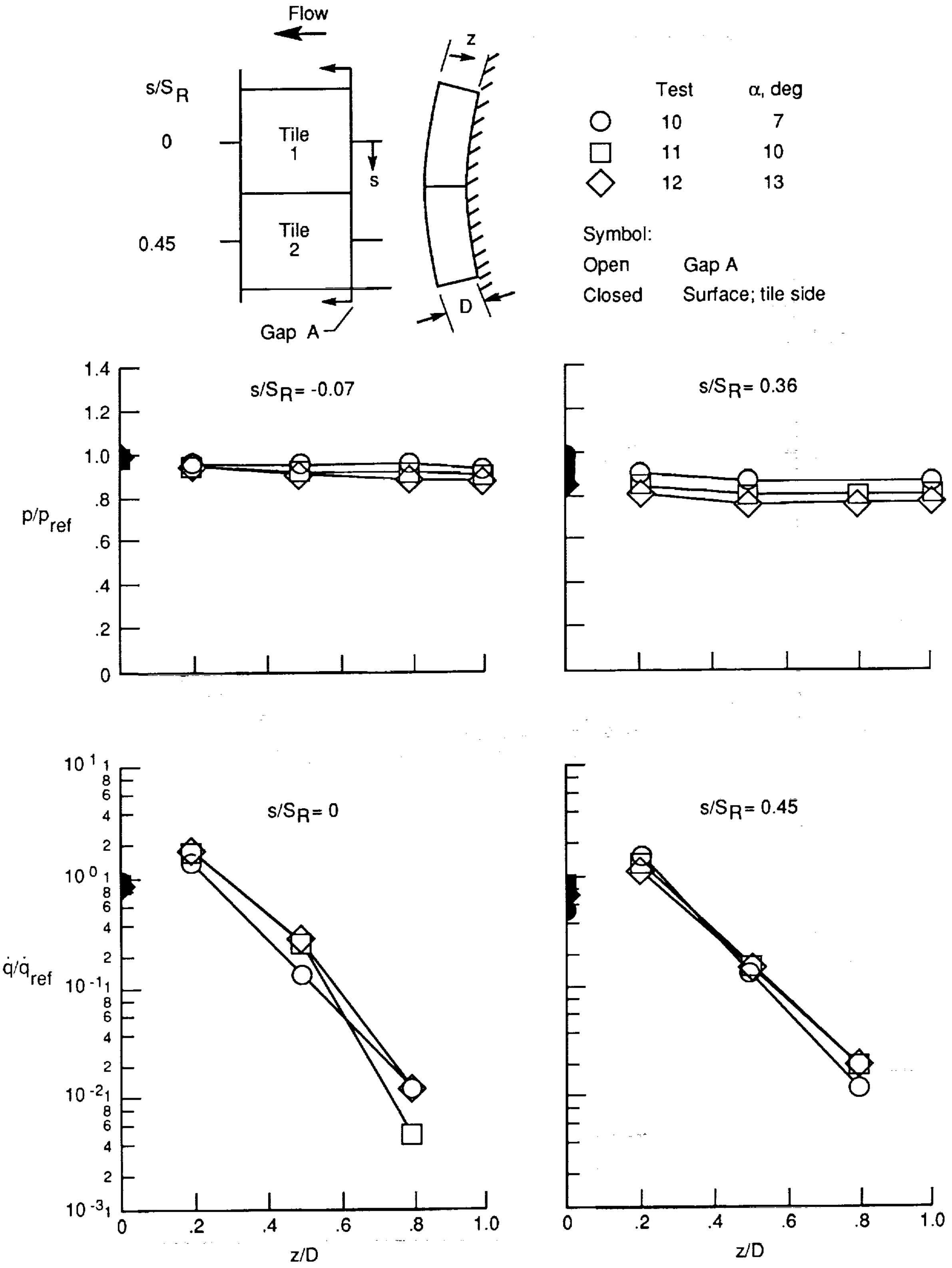

Figure 35. Variation of gap pressure and heating distributions into depth of circumferential gap A at $x/R_n = 25.7$ for configuration 2.

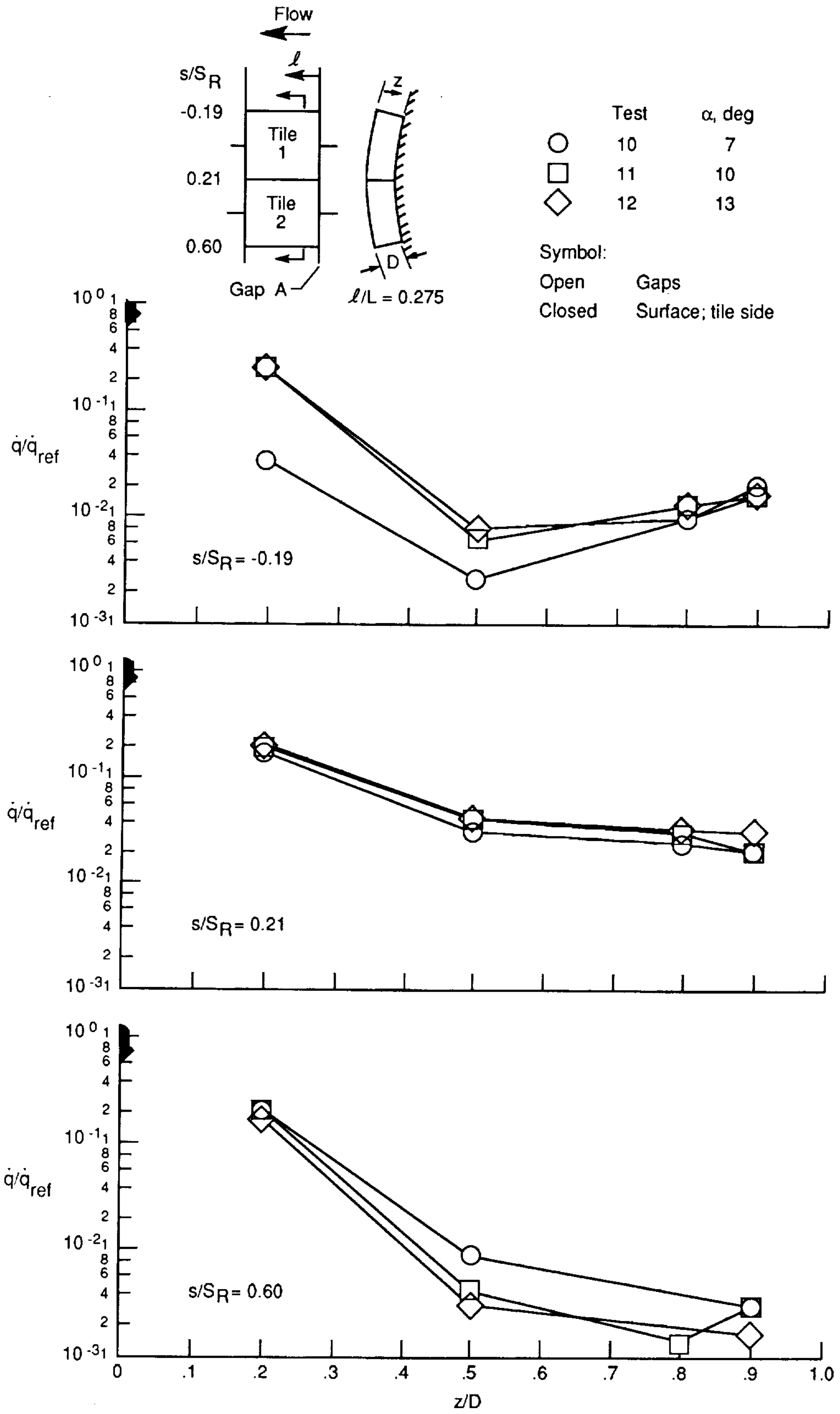

Figure 36. Variation of gap heating distributions into depth of longitudinal gaps at $x/R_n = 26.2$ for configuration 2.

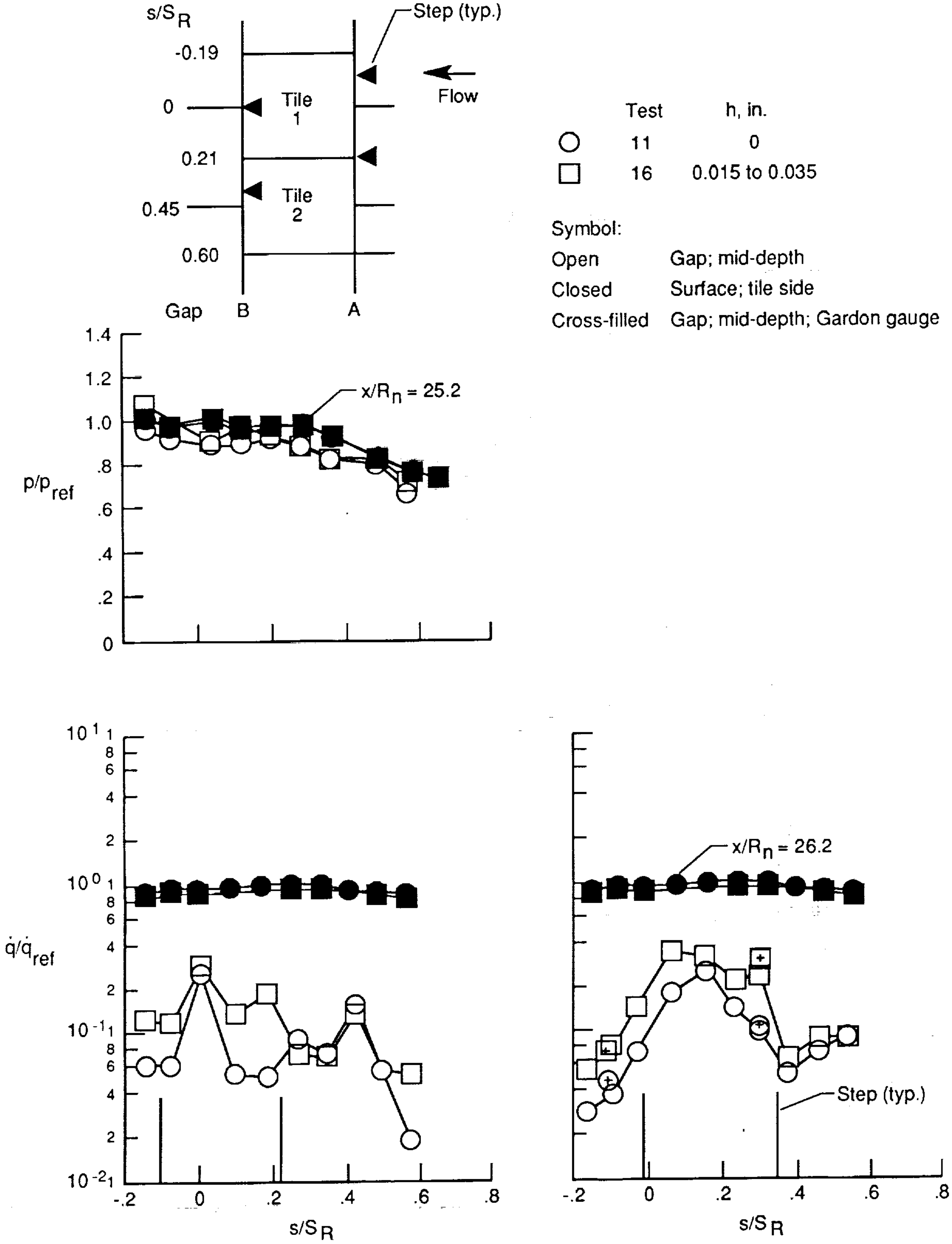

(a) Gap A. $x/R_n = 25.7$.

(b) Gap B. $x/R_n = 27.7$.

Figure 37. Effect of forward-facing steps on gap pressure and heating distributions for configuration 2 at $\alpha = 10°$.

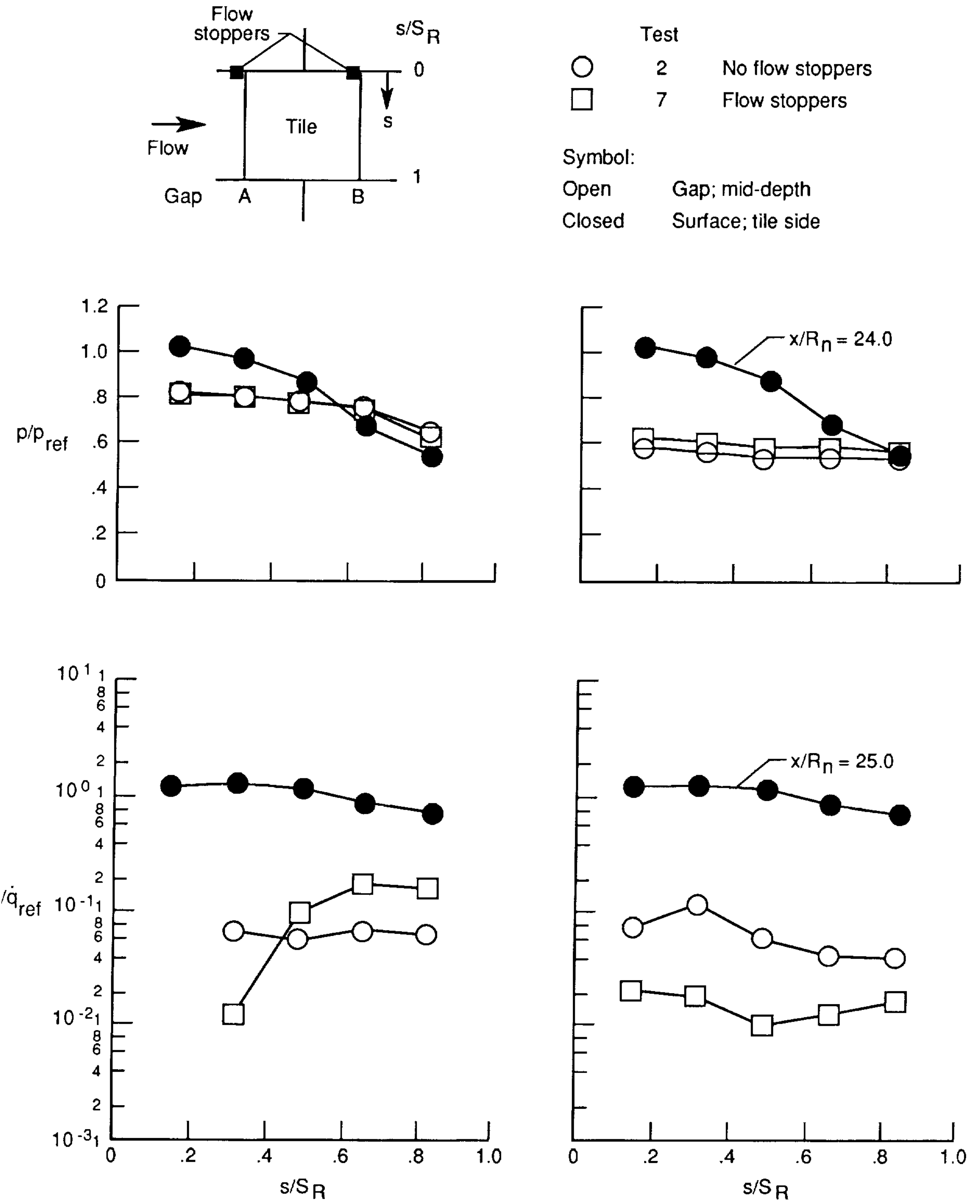

(a) Gap A. $x/R_n = 24.4$; $w = 0.075$ in.

(b) Gap B. $x/R_n = 26.4$; $w = 0.103$ in.

Figure 38. Variation of circumferential gap pressure and heating distributions with and without flow stoppers for configuration 1 at $\alpha = 10°$.

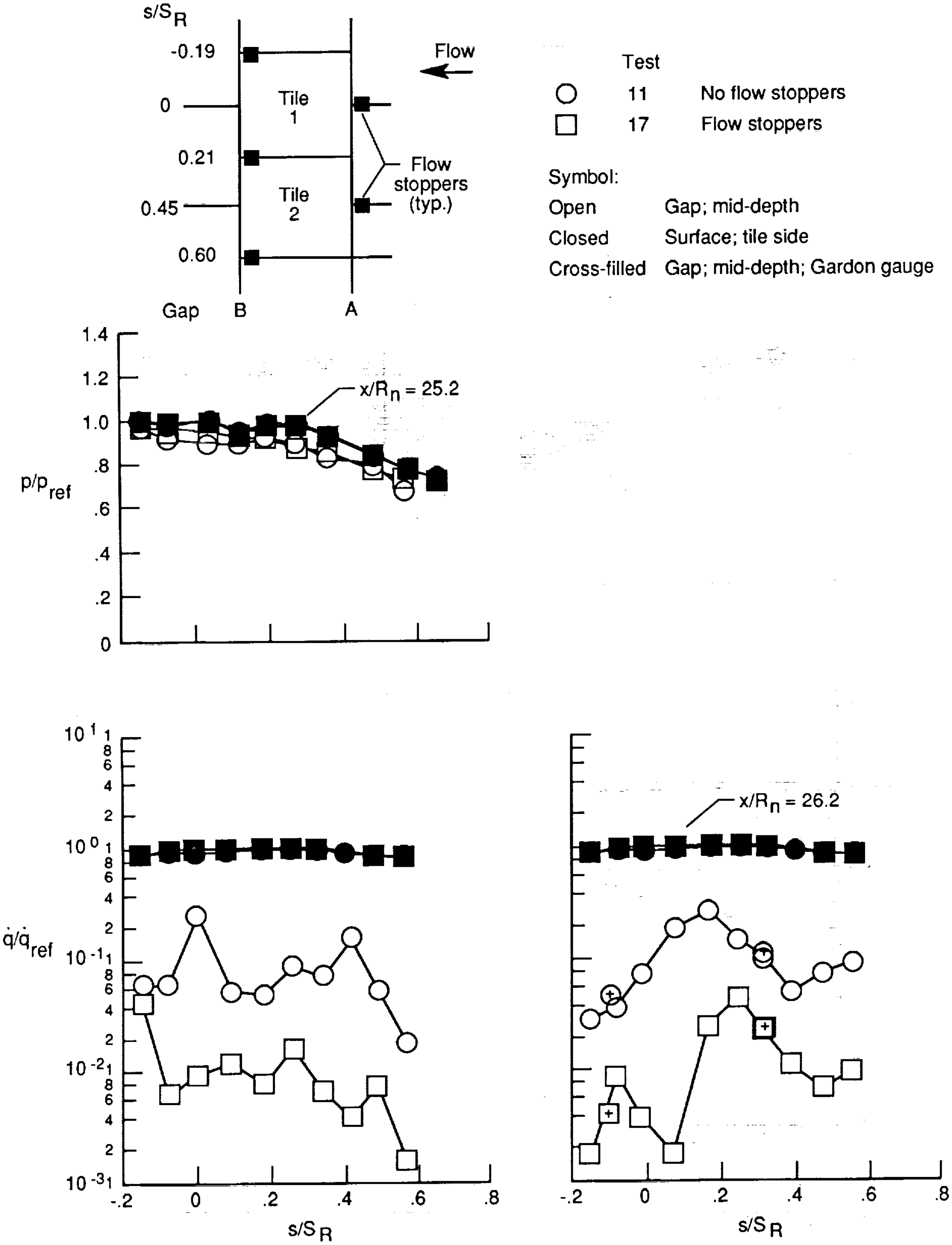

(a) Gap A. $x/R_n = 25.7$.

(b) Gap B. $x/R_n = 27.7$.

Figure 39. Effect of flow stoppers on circumferential gap pressure and heating distributions for configuration 2 at $\alpha = 10°$.

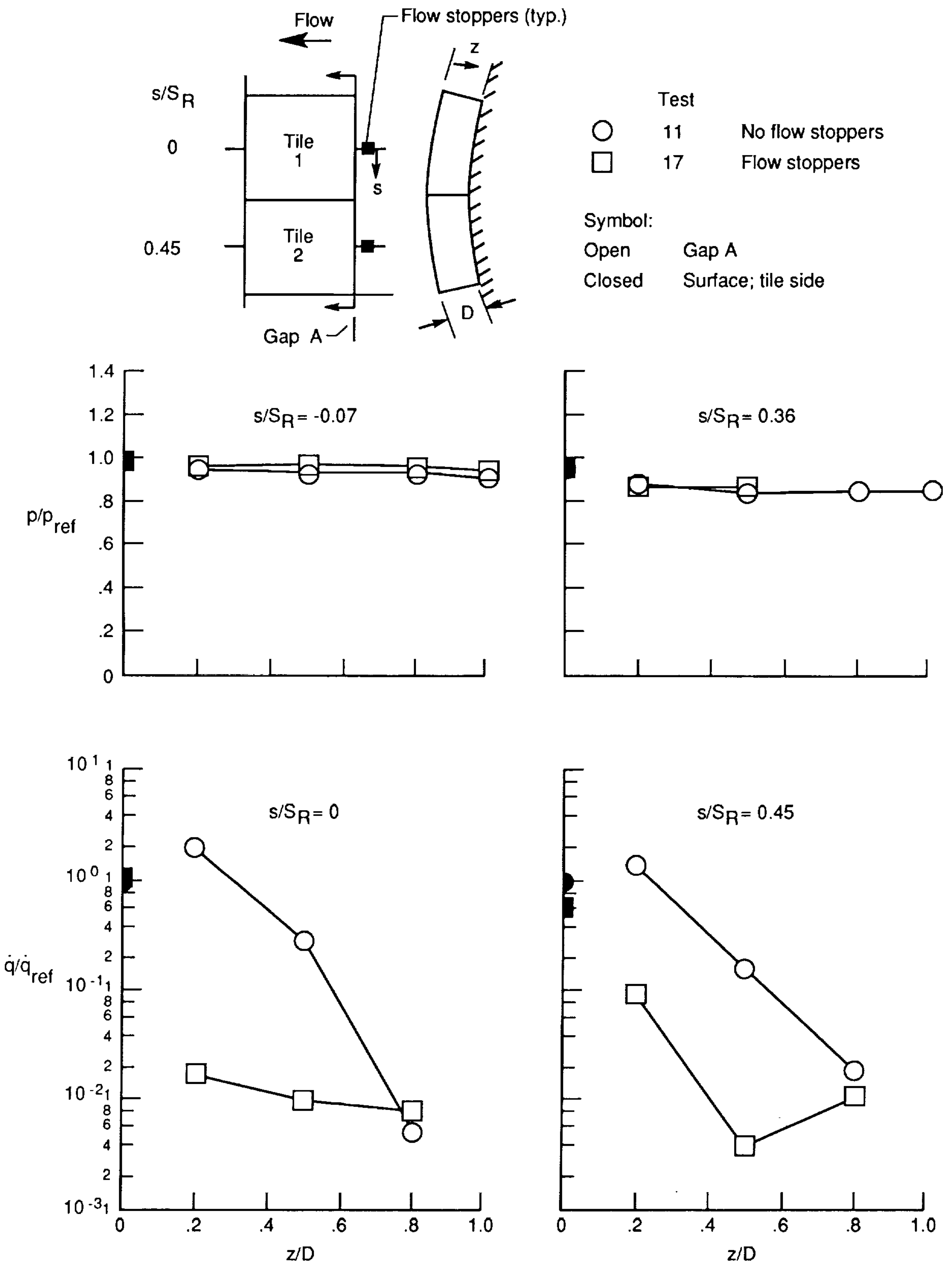

Figure 40. Effect of flow stoppers on gap pressure and heating distributions into depth of circumferential gap A for configuration 2 at $\alpha = 10°$.

NASA
National Aeronautics and Space Administration

Report Documentation Page

1. Report No. NASA TP-2988	2. Government Accession No.	3. Recipient's Catalog No.
4. Title and Subtitle Aerodynamic Pressure and Heating-Rate Distributions in Tile Gaps Around Chine Regions With Pressure Gradients at a Mach Number of 6.6		5. Report Date June 1990 6. Performing Organization Code
7. Author(s) L. Roane Hunt and Kristopher K. Notestine		8. Performing Organization Report No. L-16649
9. Performing Organization Name and Address NASA Langley Research Center Hampton, VA 23665-5225		10. Work Unit No. 506-40-21-01 11. Contract or Grant No.
12. Sponsoring Agency Name and Address National Aeronautics and Space Administration Washington, DC 20546-0001		13. Type of Report and Period Covered Technical Paper 14. Sponsoring Agency Code

15. Supplementary Notes

L. Roane Hunt: Langley Research Center, Hampton, Virginia.
Kristopher K. Notestine: PRC Kentron, Inc., Aerospace Technologies Division, Hampton, Virginia.

16. Abstract

Surface and gap pressures and heating-rate distributions were obtained for simulated thermal protection system (TPS) tile arrays on the curved-surface test apparatus of the Langley 8-Foot High-Temperature Tunnel at a Mach number of 6.6. The results indicated that the chine gap pressures varied inversely with gap width because larger gap widths allowed greater venting from the gap to the lower model side pressures. Lower gap pressures caused greater flow ingress from the surface and increased gap heating. Generally, gap heating was greater in the longitudinal gaps than in the circumferential gaps. Gap heating decreased with increasing gap depth. Circumferential gap heating at the mid-depth was generally less than about 10 percent of the external surface value. Gap heating was most severe at local T-gap junctions and tile-to-tile forward-facing steps that caused the greatest heating from flow impingement. The use of flow stoppers at discrete locations reduced heating in most gaps but increased heating in others. A limited use of "flow stoppers" or gap filler in longitudinal gaps could reduce gap heating in open circumferential gaps in regions of high surface pressure gradients.

17. Key Words (Suggested by Authors(s)) Hypersonic flight Pressure and heating-rate distributions Tile gaps Pressure gradient		18. Distribution Statement Unclassified—Unlimited Subject Category 34	
19. Security Classif. (of this report) Unclassified	20. Security Classif. (of this page) Unclassified	21. No. of Pages 68	22. Price A04

NASA FORM 1626 OCT 86

NASA-Langley, 1990

For sale by the National Technical Information Service, Springfield, Virginia 22161-2171